INVESTIGATION OF ZEOLITE NUCLEATION AND GROWTH USING NMR SPECTROSCOPY

A Dissertation

by

ALEJANDRA DEL ROCIO RIVAS CARDONA

Submitted to the Office of Graduate Studies of
Texas A&M University
in partial fulfillment of the requirements for the degree of

DOCTOR OF PHILOSOPHY

December 2011

Major Subject: Chemical Engineering

Investigation of Zeolite Nucleation and Growth Using

NMR Spectroscopy

INVESTIGATION OF ZEOLITE NUCLEATION AND GROWTH USING NMR SPECTROSCOPY

A Dissertation

by

ALEJANDRA DEL ROCIO RIVAS CARDONA

Submitted to the Office of Graduate Studies of
Texas A&M University
in partial fulfillment of the requirements for the degree of

DOCTOR OF PHILOSOPHY

Approved by:

Chair of Committee,	Daniel F. Shantz
Committee Members,	Hae-Kwon Jeong
	Juergen Hahn
	Christian B. Hilty
Head of Department,	Charles Glover

December 2011

Major Subject: Chemical Engineering

ABSTRACT

Investigation of Zeolite Nucleation and Growth Using NMR Spectroscopy.

(December 2011)

Alejandra del Rocio Rivas Cardona, B.S., Instituto Tecnologico de Celaya, Mexico;

M.S., Instituto Tecnologico de Celaya, Mexico

Chair of Advisory Committee: Dr. Daniel F. Shantz

Zeolite nucleation and growth is a complex problem that has been widely investigated but still not completely understood. However, a full understanding of this process is required in order to develop predictive models for the rational design and control of the zeolite properties. The primary objective of this dissertation is to determine the strength of organic-inorganic interactions (i.e., the adsorption Gibbs energy) in transparent synthesis mixtures using PFG NMR spectroscopy, in order to provide more information for a better understanding of zeolite nucleation and growth.

Three main tasks were conducted in this work. The first was an investigation of the organocation role in precursor mixtures of silicalite-1, where the Gibbs energy of the organocation adsorption on the silica particles was determined at 25°C. The findings showed that small changes in the adsorption Gibbs energy resulting from the differences in the molecular structure of the organocations lead to large changes in both the stability of the precursor particles and the rate of silicalite-1 formation. The second was an in situ PFG NMR investigation of silicalite-1 synthesis mixtures, where the adsorption Gibbs

energy was determined at 25°C and 70°C, and the time evolution of silicalite-1 was monitored at synthesis conditions. The findings showed similar adsorption Gibbs energies at 25°C and 70°C. Also, a maximum in the organocation diffusion coefficients was observed during the time evolution of silicalite-1, which was associated with the exothermic-endothermic transition occurring during the synthesis. The third was a systematic investigation of silicalite-1 precursor mixtures with varying degrees of dilution, where the effect of the composition of the mixtures on their conductivity, pH and particle size distribution (PSD) was studied. The results showed that conductivity, pH, and PSD are strongly affected by the mixture composition.

The main conclusion of this research is that the strength of the organic-inorganic interactions in transparent synthesis mixtures can be determined from experimental data of the organocation self-diffusion coefficients obtained with PFG NMR spectroscopy. The outcome information of this research should contribute to the development of a more detailed molecular-level description of the zeolite nucleation and growth, which is expected to allow the emergence of a new generation of materials by design.

DEDICATION

This work is dedicated to my parents, Juan Jose and Ma. del Pilar,† for inspiring me with their tenacity and joy for life to follow my passions, persevere in my endeavors, and pursue my dreams; and to my brother, Juan Alberto, for awakening my interest in science, providing me his endless support, and sharing with me this wonderful journey of lifelong learning.

ACKNOWLEDGEMENTS

I would like to express my sincere gratitude to my advisor, Dr. Shantz, for giving me the opportunity to work in his research group. He always gave me the freedom to explore my ideas, and provided me with his guidance and support all along the way.

I would also like to thank my committee members, Dr. Hahn, Dr. Jeong, and Dr. Hilty for their support, insightful comments, and feedback related to this research project.

I would especially like to thank Mr. Steve Silber and Dr. K. P. Sarathy of the NMR facility in the Department of Chemistry for their generous technical and organizational support, and for their useful insights in setting up the NMR experiments.

I would like to acknowledge financial support from the National Science Foundation. Also, part of my education was supported by the Mexican National Council of Science and Technology (CONACYT for its acronym in Spanish: Consejo Nacional de Ciencia y Tecnologia) through a national scholarship.

Finally, I would like to express my deep gratitude to all the people that encouraged and helped me throughout these years as a Ph.D. student. In particular, I want to thank my family and closest friends for their constant and unwavering support.

NOMENCLATURE

a, b, c	axes of the unit cell
a_A, a_B	apparent decay constants for populations in sites A and B
b	site assigned to bound organocations
$\boldsymbol{B_0}$	magnetic flux density vector (static magnetic field)
B_0	magnetic flux density field
C	equilibrium concentration of organocation in the mixture
d_1	first delay of the sequence
d_{hkl}	distance between planes with Miller indices hkl
d_H	hydrodynamic diameter
D	translational self-diffusion coefficient
D_b	diffusion coefficient of the bound organocation
D_f	diffusion coefficient of the free organocation
D_{obs}	observed (translational self-diffusion) diffusion coefficient
E	energy of a magnetic dipole in a magnetic field
f	site assigned to free organocations
$\boldsymbol{g_n}$	vector of additional field contributions at different positions along the z-axis
g	gradient strength
$G(\tau)$	correlation function of the scattered intensity
$[H^+]$	concentration of the hydrogen ions

I	overall nuclear spin
I_0	maximum measurable signal intensity
I_g	intensity at a given value of gradient strength
I_τ	intensity at $t = \tau$
$I(x)$	normalized echo intensity decay
k_B	Boltzmann constant
K_{ad}	adsorption constant
K_F	Freundlich adsorption constant
K_L	Langmuir adsorption constant
K_U	unified adsorption constant
m	magnetic or directional quantum number
$\boldsymbol{M}$	bulk magnetization vector
M_0	equilibrium value of the bulk magnetization vector $\boldsymbol{M}$
$M_{y'}$	y'-component of the bulk magnetization vector $\boldsymbol{M}$
M_z	z-component of the bulk magnetization vector $\boldsymbol{M}$
$1/n$	heterogeneity factor
n	valence of cation M
n_{obs}	number of observations
n_{RI}	refractive index of the medium
n_w	number of wavelengths
N_α	number of nuclei in the lower level of energy
N_β	number of nuclei in the upper level of energy

$[OH^-]$	concentration of the hydroxide ions
p	number of parameters in the fitting model
p_A, p_B	apparent populations in sites A and B
$\boldsymbol{P}$	angular momentum vector
P_z	z-component of the angular momentum
Q	objective function
r_f, r_b	decay constants for sites *f* and *b*
r_m	mean decay constant
R	gas constant
R_1	spin-lattice or longitudinal relaxation rate
R_2	spin-spin or transverse relaxation rate
R^2	determination coefficient
t	time
T	absolute temperature in K
T_1	spin-lattice or longitudinal relaxation time
T_2	spin-spin or transverse relaxation time
x	total number of AlO_2 tetrahedra per unit cell or moles of organocation in a mixture
x_f , x_B	true molecular fractions of the probe molecule in sites *f* and *b*
x_{NP}, x_{SA}, x_{BA}	fraction of nanoparticles, small aggregates, and big aggregates
y	total number of SiO_2 tetrahedra per unit cell or moles of TEOS in a mixture

w	total number of water molecules per unit cell
z	moles of water in a mixture
Greek symbols	
α, β, γ	angles between axes of the unit cell
δ	chemical shift
$\delta, \delta_1, \delta_2, \delta_3$	duration of the gradient pulse
Δ	diffusion time or diffusion delay
Δ_{aux}	auxiliary diffusion time or auxiliary diffusion delay
ΔE	energy difference between two adjacent levels of energy
ΔG_{ad}	adsorption Gibbs energy
γ	gyromagnetic ratio of a nucleus
Γ	amount of bound organocation
Γ_c	characteristic decay time
Γ_{max}	maximum amount of bound organocation per amount of silica nanoparticles
λ	wavelength of the laser beam
η	viscosity of the medium
μ	nuclear magnetic moment
μ_z	z-component of the nuclear magnetic moment
ν_0	original precession frequency before introducing inhomogeneities in the magnetic field

ν_1	electromagnetic radiation frequency or RF field frequency
ν_L	precession frequency or Larmor frequency
$\boldsymbol{\nu_n}$	precession frequency vector
ν_{sample}	sample frequency
$\nu_{reference}$	reference frequency
σ	residual standard deviation
θ	scattering angle
τ	delay time or gradient stabilization delay
τ_c	correlator time delay
$\hbar$	reduced Planck's constant

Abbreviations and acronyms

BBU	basic building unit
cac	critical aggregation concentration
CONTIN	constrained Laplace inversion
CPMG	Carr-Purcell-Meiboom-Gill experiment
DI	deionized (water)
DLS	dynamic light scattering
Dbppste	DOSY bipolar pulse pair stimulated echo
Dbppste_cc	DOSY bipolar pulse pair stimulated echo with convection Compensation
DOE	design of experiments
DOSY	diffusion ordered spectroscopy

ETPA	ethyltripropylammonium
FCC	fluid catalytic cracking
FID	free induction decay
FFT	fast Fourier transform
HRTEM	high-resolution transmission electron microscopy
ILT	inverse Laplace transform
LTA	Linde type A
MFI	Mobil five
MTPA	methyltripropylammonium
NNLS	non-negative constrained least squares
NMR	nuclear magnetic resonance
PBU	periodic building unit
PCS	photon correlation spectroscopy
PGSE	pulsed gradient spin echo
PFG	pulsed-field gradient
PSD	particle size distribution
PXRD	powder X-ray diffraction
QELS	quasi-elastic light scattering
RF	radiofrequency
SBU	secondary building unit
SDA	structure directing agent
SSU	structural sub-unit

TAA	tetraalkylammonium
TEM	transmission electron microscopy
TEOS	tetraethyl orthosilicate
TMA	tetramethylammonium
TMAA	N,N,N-trimethyl-1-adamantylammonium
TMBDMP	4,4'-trimethylenebis (1,1’-dimethylpiperidinium)
TMOS	tetramethyl orthosilicate
TPA	tetrapropylammonium
XRD	X-ray diffraction
ZSM-5	Zeolite Socony Mobil-five

TABLE OF CONTENTS

CHAPTER Page

CHAPTER Page

LIST OF FIGURES

FIGURE Page

FIGURE Page

FIGURE Page

FIGURE Page

LIST OF TABLES

TABLE Page

CHAPTER I

INTRODUCTION

Porous materials are solids that contain void spaces.[1] In general, they have porosities between 0.2 and 0.95, where porosity is defined as the fraction of pore volume to the total volume of material. Pores can be classified as open pores, which connect to the outside of the material, and closed pores, which are isolated from the outside. Open pores can have penetrating, non-penetrating, and/or ink-bottle morphology (Figure 1.1). Open pores, and more specifically penetrating pores, are required for most of the industrial applications of porous materials because they provide large surface area and have low density. These properties are important for the application of porous materials as filters, sensors, and catalysts. Zeolites are a good example of catalytic porous solids. The fine pores within their structure provide them with a high surface area necessary for catalytic applications.

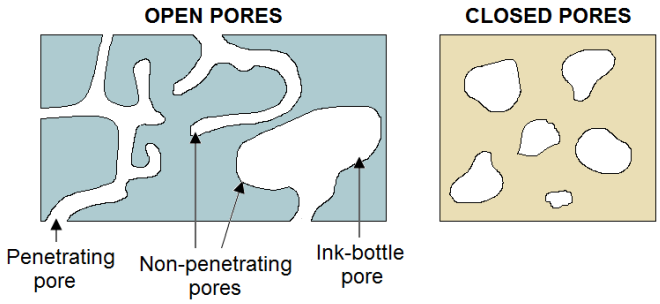

Figure 1.1 Scheme of different pore morphologies of porous materials. Adapted from Kozo, I.; Sridhar, K.; Makoto, N., *Porous Materials. Process technology and applications*. Kluwer Academic Publishers: Dordrecht, **1998**.

This dissertation follows the style of *The Journal of Physical Chemistry C*.

The International Union of Pure and Applied Chemistry (IUPAC) has recommended specific nomenclature for porous materials.[1] Their classification according to their pore size is shown in Figure 1.2. Porous materials with pore diameters less than 2 nm are considered as microporous, those with pore diameters between 2 nm and 50 nm are considered as mesoporous, and those with diameters larger than 50 nm are considered as macroporous. Most zeolites are classified as microporous materials.

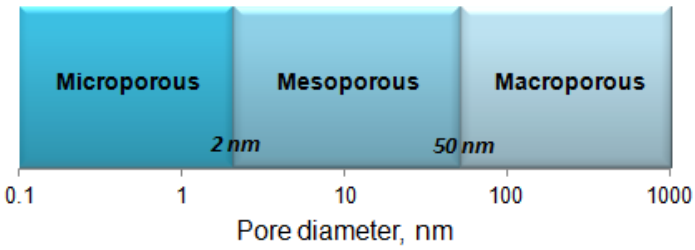

Figure 1.2 Classification of porous materials according to their pore size. Adapted from Kozo, I.; Sridhar, K.; Makoto, N., *Porous Materials. Process technology and applications*. Kluwer Academic Publishers: Dordrecht, **1998**.

Porous materials can be also classified according to the relationship between their pore size and application. This classification is useful in considering applications of porous materials and is shown in Figure 1.3. A wide range of pore size (from Angstroms to millimeters) required for the different applications of porous solids can be observed in this figure.

1.1 Zeolite fundamentals

Zeolites are classically defined as crystalline aluminosilicate materials that have pores of molecular dimensions.[2] However, this definition has evolved during the last decades to include non-aluminosilicate materials with analogous properties to those of zeolites.[3] Zeolites can exist as natural minerals or as synthetic materials. Natural zeolites

are extensively mined in many places of the world,[4] including China, Korea, Japan, Turkey, Slovakia, and the United States.[5] The global production in 2010 was estimated to be approximately 3 million tons, from which about 60000 tons were produced by the U.S.[5] Though the world reserves of natural zeolites have not been determined, they are estimated to be large, and might approach 10 trillion tons in the U.S. alone.[5] Synthetic zeolites, on the other hand, are made for specific uses, either for industrial applications or research purposes. The interest of scientists in the development and improvement of zeolites has been encouraged by the broad industrial application of these materials.

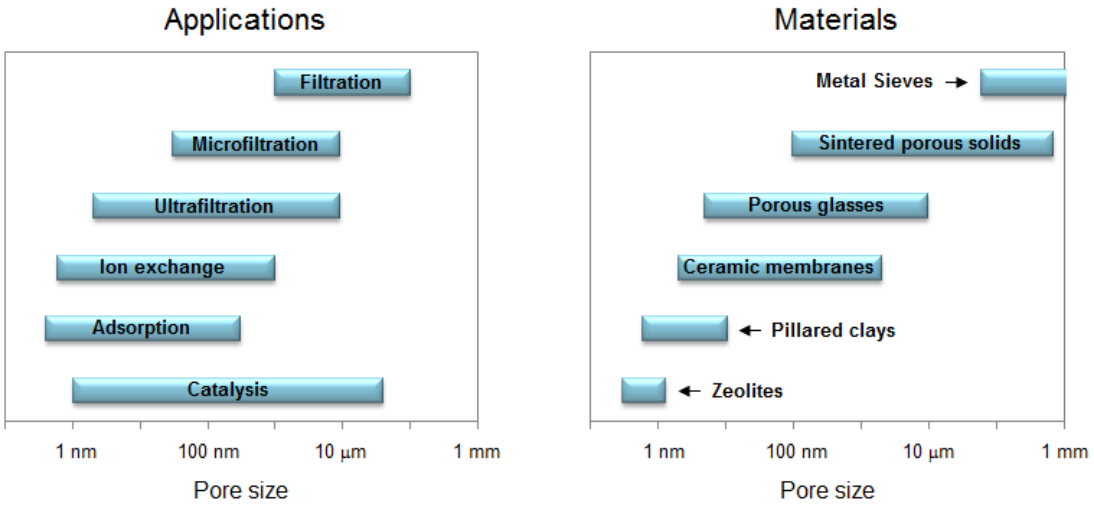

Figure 1.3 Relationship between pore size and applications of porous materials. Adapted from Kozo, I.; Sridhar, K.; Makoto, N., *Porous Materials. Process technology and applications*. Kluwer Academic Publishers: Dordrecht, **1998**.

1.1.1 Historical overview

In 1756 the Swedish mineralogist Cronstedt recognized the first zeolite mineral, stilbite.[3,6] He observed that large amounts of steam from the water absorbed by the mineral were produced upon heating. Therefore, he called it “zeolite”, derived from the

Greek ζέω (zeo) that means "boil" and λίθος (lithos) that means "stone".[3] Since their discovery by Cronstedt, natural zeolites were used in jewelry for about 200 years,[6] although in 1858 Eichhorn showed that zeolites exhibit reversible ion exchange.[3,6] The first hydrothermal synthesis of a zeolite (levynite) was reported in 1862 by Deville and the first use of X-ray diffraction (XRD) for identification of zeolites was reported in 1927 by Leonard.[3]

In 1938 all the early qualitative observations mentioned above were extended by the work of Barrer. He presented the first classification of zeolites based on molecular size considerations in 1945 and the first definitive synthesis of zeolites that included the analogue of modernite in 1948. In this way studies on zeolite synthesis were initiated. Between 1949 and 1954 Milton and Breck discovered several zeolites including zeolite A, X and Y.[3]

In 1954 zeolites started to be commercialized by Union Carbide Corporation for industrial applications such as separations and purifications.[3] The earliest application was drying refrigerant and natural gas. Mobil Oil introduced the use of zeolite X as a cracking catalyst in 1962 and reported the synthesis of zeolites beta and ZSM-5 between 1967 and 1969. Since then, the use of zeolites for industrial applications has grown considerably. In general, an explosion in the discovery of new zeolite structures took place in the 80's and 90's. In the 1980's, for instance, many studies were carried out on the synthesis and applications of ZSM-5. Incorporation of metals such as iron, germanium, titanium, and others, into the ZSM-5 framework was also reported during these years. The explosion in the discovery of new zeolites structures continued through

the 90's. Based on the great interest shown in this area during the past few decades, it is expected that the work on zeolite science continues in order to achieve further advances.

1.1.2 Structure and composition

Zeolites have a three-dimensional framework structure that forms uniformly sized pores of molecular dimensions.[7] The zeolite framework is comprised of tetrahedral building units of TO_4, where T is typically Si and/or Al, but it may also be P, Ga, B, Be, and others.[8] The charge of the framework depends on its T-atoms. For instance, a negative charged framework can be formed when Al^{3+} is present and replaces Si^{4+} in some of the framework sites. The tetrahedral building units, also known as basic building units (BBUs), are interconnected with each other forming larger structures (Figure 1.4) that can be described by finite units such as secondary building units (SBUs) and structural sub-units (SSUs), and by infinite building units such as periodic building units (PBUs). All these units help to describe features of the lattice structure of zeolites such as chains, rings, and cages. The pores formed within a zeolite framework can measure between 0.3 to 1 nm and they can host cations, water, and/or other molecules usually referred as extra-framework molecules. The effective pore widths are characterized by the size of the ring that defines the pore, which is usually designated as n-ring (where n is the number of T-atoms). An 8-ring is considered to be a small pore width (~0.41 nm), a 10-ring a medium one (~0.55 nm), and a 12-ring a large one (~0.74 nm). The channel arrangement influences the properties of zeolites, and therefore, it is an important characteristic of these materials. Even relatively minor structural differences result in significant changes in the zeolite properties. The structures of

zeolites can be elucidated with a variety of methods that include solid state nuclear magnetic resonance (NMR), electron microscopy, sorption experiments and powder X-ray diffraction (PXRD). Among these methods XRD is widely used to determine the structure of zeolites, though it is not quite straightforward.[7] The structural formula of a zeolite unit-cell (the smallest unit of structure) can be represented as

$$M_{x/n}\left[\left(AlO_2\right)_x\left(SiO_2\right)_y\right]\bullet wH_2O \qquad (1.1)$$

where n is the valence of the cation M, x and y are the total number of tetrahedra per unit cell, and w is the number of water molecules per unit cell.[3]

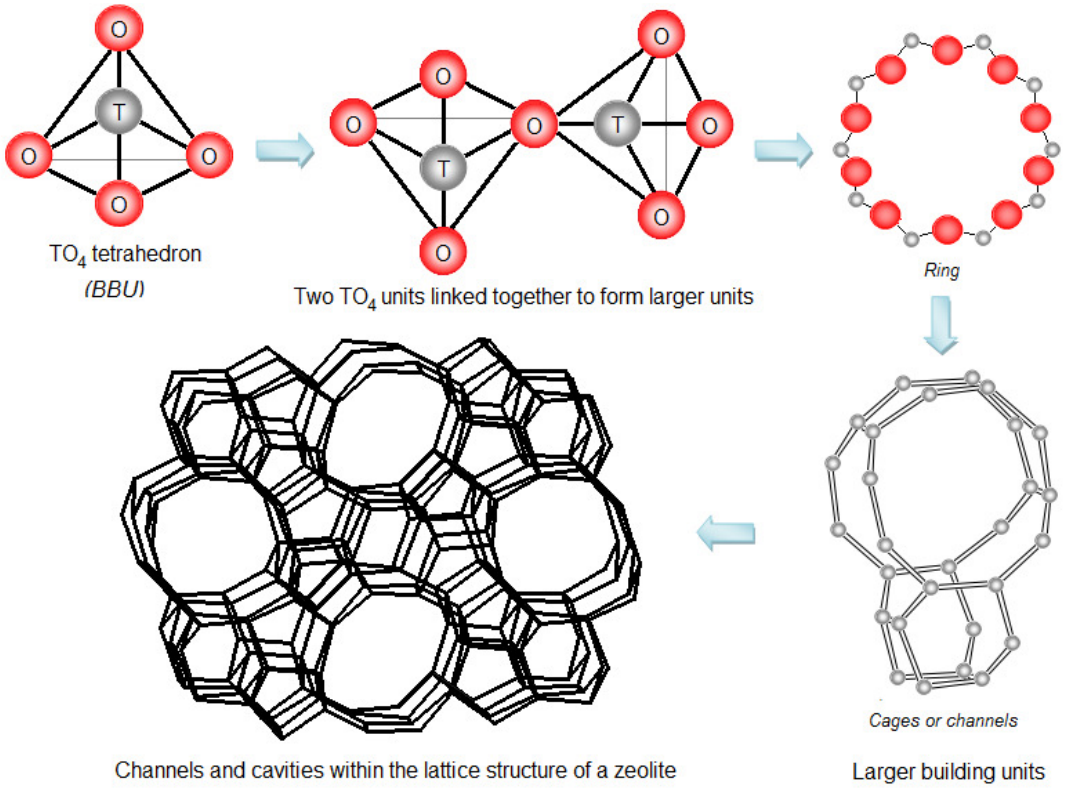

Figure 1.4 Scheme of how basic primary units (BBUs) of TO_4 and other larger units are connected together within a zeolite structure. The last two schemes of this figure were reproduced with permission from Baerlocher, C.; McCusker, L. B., *Database of Zeolite Structures*. http://www.iza-structure.org/databases (accessed August **2011**).

1.1.3 Classification and nomenclature

Classifying zeolites has been a need since scientists first recognized these materials. Their framework structure is fundamental for understanding their chemistry.[7] Zeolites have been classified according to different features, but typically classifications are related to the zeolite composition. In Table 1.1 the classification of zeolites according to their Si/Al ratio is shown.[3] Three somewhat arbitrary categories (low-silica, intermediate-silica, and high-silica zeolites) and examples of zeolites within each of them are shown in this table.

Table 1.1 Classification of zeolites according to their Si/Al ratio.

Category	Si/Al ratio	Examples
Low-silica zeolites	1 – 1.5	A, X
Intermediate-silica zeolites	~ 2 – 5	Y, L
High-silica zeolites	~ 10 – 100	ZSM-5, beta

The classification of zeolites by framework type was first proposed by Meier and Olson in 1970 and it is the accepted classification by the zeolite community. A framework type, in contrast with a framework structure, describes the connectivity of the tetrahedral coordinated T-atoms in the highest possible symmetry, but the composition of the framework, the extra-framework molecules, and the dimension of unit-cell are not considered. Thus, many different materials can be described under one single designation.[7] For example, boralite C, encilite, monoclinic H-ZSM-5, ZSM-5, and silicalite all have the MFI framework type. The Structure Commission of the

International Zeolite Association according to the rules of the IUPAC Commission on Zeolite Nomenclature has assigned a three-letter code to each of the approved framework types. These codes are usually assigned according to the name of the zeolite (e.g., FAU from faujasite, LTA from Linde Type A, and MFI from ZSM-5 (Zeolite Socony Mobil – five). 197 framework types codes have been assigned by March 2011 and information about them can be found in the Atlas of Zeolite Framework Types.[8]

1.1.4 High-silica zeolites: the MFI framework type

High-silica zeolites tend to be hydrophobic and they are well known for their catalytic and adsorption properties. MFI (Figure 1.5) is one of the most popular high-silica zeolites as well as one of the most successful framework types regarding scale-up for industrial applications.[9] MFI is the framework type code for ZSM-5 structure, which is part of the pentasil family.

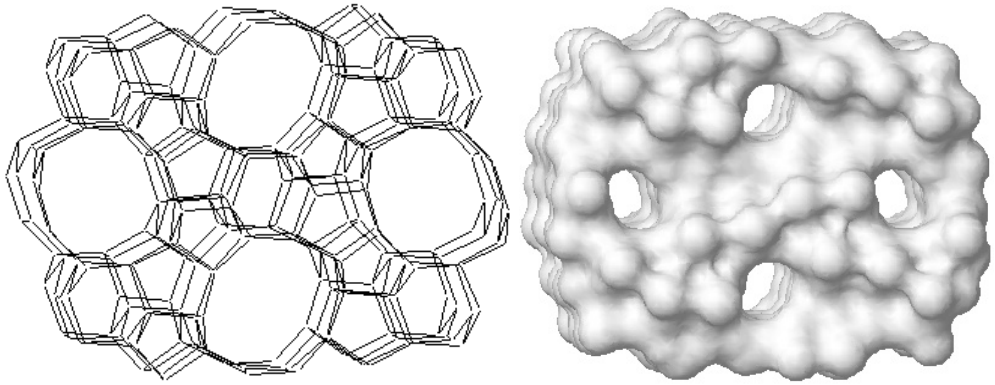

Figure 1.5 MFI framework displaying only Si-atoms (left) and MFI molecular surface (right). Reproduced with permission from Baerlocher, C.; McCusker, L. B., *Database of Zeolite Structures*. http://www.iza-structure.org/databases (accessed August **2011**).

ZSM-5 is one of the most common zeolites and has been widely used as catalyst in many refinery and petrochemical processes. ZSM-5 has a 3-dimensional, 10-ring

channel system,[7] with zig-zag channels of near-circular cross-section and straight channels with elliptical cross-section.[6] All the intersections in ZSM-5 have the same size. ZSM-5 has low water content, and its framework has hydrophobic tendencies. Moreover, ZSM-5 has low aluminum content, and therefore, few extra-framework cations. The pure-silica analogue of ZSM-5 is silicalite-1. Silicalite-1 has a neutral framework due to its lack of aluminum atoms, and therefore it is a good adsorbent of organic molecules. In Table 1.2 some of the most important characteristics of ZSM-5 and zeolite A structures are summarized.

Table 1.2 Important characteristics of ZSM-5 structure.[7,8]

Characteristic	ZSM-5	
Composition	High Si/Al	
Crystal chemical data	$\|Na_n\ (H_2O)_{16}\|\ [Al_nSi_{96-n}O_{192}]$-MFI, n<27	
Framework density	17.9 T-atoms per 1000 Å^3	
Channels	5.1 x 5.5 Å (10-ring view along [100]) 5.3 x 5.6 Å (10-ring view along [010])	
Hosted cation types	Alkali and quaternary ammonium (e.g., Pr_4N^+, also known as TPA)	
Related materials	ZSM-5 [As-Si-O]-MFI [Fe-Si-O]-MFI [Ga-Si-O]-MFI AMS-1B AZ-1 Bor-C Boralite Encilite FZ-1 LZ-105 Monoclinic H-ZSM-5	Mutinaite NU-4, NU-5 Silicalite TS-1, TSZ, TSZ-III TZ-01 USC-4 USI-108 ZBH ZKQ-1B ZMQ-TB organic-free ZSM-5
Applications	Sorption and ion-exchange	

1.1.5 Low-silica zeolites: the LTA framework type

Low-silica zeolites tend to be hydrophilic, and have a high number of balancing extra-framework cations and a very high affinity for polar molecules. LTA (Figure 1.6) is one of the most widely used low-silica zeolites regarding scale-up for industrial applications.[9] LTA is the framework type code for the zeolite A structure.

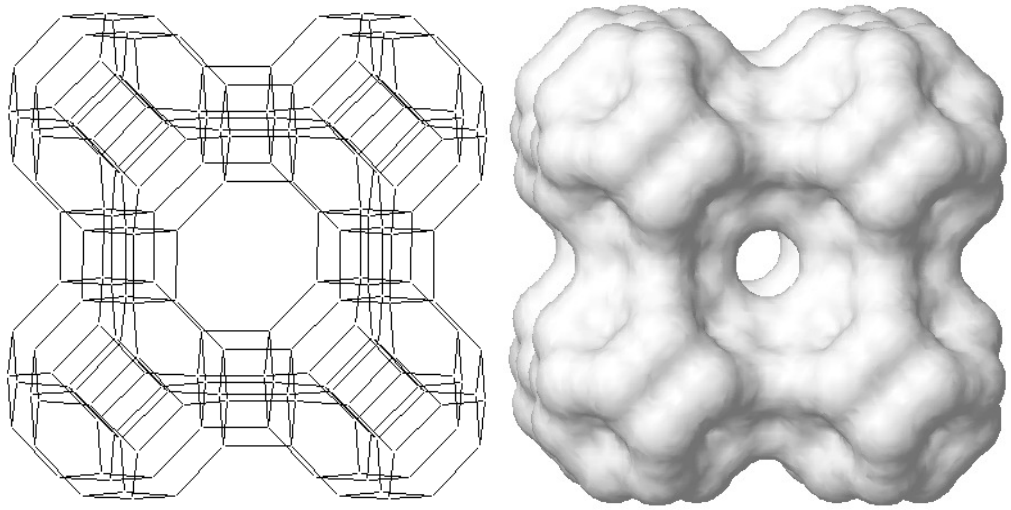

Figure 1.6 LTA framework displaying only Si-atoms (left) and LTA molecular surface (right). Reproduced with permission from Baerlocher, C.; McCusker, L. B., *Database of Zeolite Structures*. http://www.iza-structure.org/databases (accessed August **2011**).

Zeolite A is also a common zeolite and has been widely applied as an ion-exchanger (water softener) in laundry detergents.[7,10] Zeolite A has a 3-dimensional, 8-ring channel system[7] that is comprised by polyhedral cavities that share all their faces with other polyhedra and form the so-called space-filling structure.[6] In contrast with ZSM-5, zeolite A has high aluminum content (typically, Si/Al ~ 1 as compared with Si/Al > 30 for ZSM-5). In Table 1.3 some of the most important characteristics of zeolite A structure are summarized.

Table 1.3 Important characteristics of zeolite A structure.[7,8]

Characteristic	Zeolite A	
Composition	Low Si/Al	
Crystal chemical data	$\|Na_{12}\ (H_2O)_{27}\|_8\ [Al_{12}Si_{12}\ O_{48}]_8$-LTA	
Framework density	12.9 T-atoms per 1000 $Å^3$	
Channels	4.1 x 4.1Å (8-ring view along [100])	
Hosted cation types	Alkali (e.g., Na^+, K^+)	
Related materials	Zeolite A [Al-Ge-O]-LTA [Ga-P-O]-LTA Alpha Dehydrated zeolite A ITQ-29	LZ-215 N-A SAPO-42 ZK-21 ZK-22 ZK-4
Applications	Sorption and ion-exchange	

1.1.6 Importance of zeolites: properties and applications

The unique structure of zeolites gives these materials special properties such as catalytic and selective adsorption capability resulting from their large internal surface area and void space, or the ability to exchange ions due to the loosely-bound nature of the extra-framework ions.[4] One of the major uses of zeolites is in catalysis, specifically, in the petrochemical industry for fluid catalytic cracking (FCC). Some zeolite properties and their relation with their catalytic functionality are summarized in Table 1.4.[6]

Table 1.4 Zeolite properties and their catalytic functionality. Reproduced with permission from Dyer, A., *An Introduction to Zeolite Molecular Sieves*. John Wiley & Sons: Chichester, **1998**.

Property	Catalytic functionality
Cavities within their channel system	Provides an extensive surface area desirable for catalytic processes
Variable pore size	Creates reactant and product selectivity while acting as molecular sieves
Ion exchange	Extra-framework cations control the pore size, create active sites (high energy fields), and enable distribution of catalytically active metals
Salt occlusion	Controls pore size, provides another method for metal incorporation, can improve stability and poison resistance
Framework modification	Changes the lattice charge in order to enhance active sites and thermal stability

1.2 Zeolite synthesis

In general, the synthesis of a zeolite is produced by crystallization of species in a mixture composed of a silica and/or aluminum source combined with water, under pH conditions controlled by OH^- ion concentrations.[6] Though the synthetic preparation of zeolites is relatively simple, the nucleation and growth process, taking place between the initial multicomponent mixture and the desired final zeolite phase, is rather complicated.[7]

1.2.1 Important parameters

A large number of factors are involved in the nucleation and growth of zeolites and affect the formation of their final phase. These parameters, among others, are composition, silicon and aluminum sources, Si/Al ratio, pH, water content, inorganic cations, organic cations, solvents, stirring, aging, temperature, and time.[7]

Composition

The composition of the initial mixture is crucial in determining the final zeolite phase.[11] This was previously shown by Breck and is illustrated in Figure 1.7. Breck's work shows how the composition of a Na_2O-Al_2O_3-SiO_2-H_2O mixture greatly affects the structure and framework type of the zeolite formed. This parameter is directly related with other synthesis parameters such as the Si/Al ratio, alkalinity, and water content.

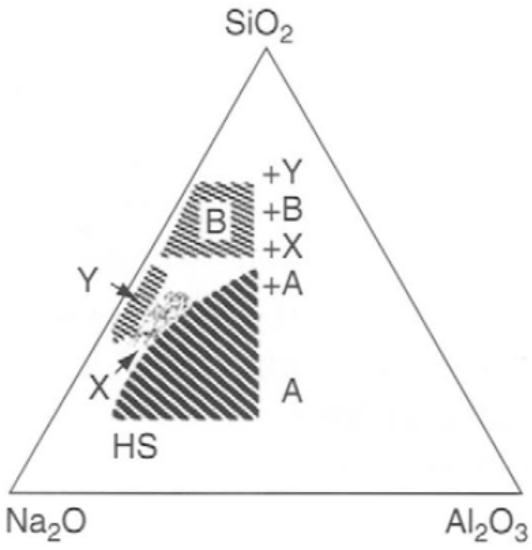

Figure 1.7 Reaction composition diagram of a Na_2O-Al_2O_3-SiO_2-H_2O system at 100°C. The water content is 90-98 mol% and the silica source is sodium silicate. Reproduced with permission from Breck, D. W., *Zeolite molecular sieves. Structure, chemistry, and use*. John Wiley & Sons: New York, **1974**. Copyright © 1974 John Wiley & Sons.

Si and Al sources

The chemical and physical nature of the Si and Al sources has an important effect on the zeolite synthesis and their influence on the zeolite crystallization has been previously reported.[11-13] The most common silicon sources are colloidal silica, fumed silica, tetramethyl orthosilicate (TMOS), and tetraethyl orthosilicate (TEOS). Different

silicon sources have different solubility and reactivity, and therefore they play an important role in the nucleation and growth process by affecting the nature of the silicate species and their distribution in the mixture. It was found that the different surface areas of the silicon source can affect the crystallization rate, the crystal size, and the particle size distribution of some zeolites, apparently because is much more easy to dissolve silica with high surface area.[14] Moreover, less-reactive silicon sources might provide fewer nucleation sites and ultimately favor the formation of large crystals. On the other hand, aluminum sources can also affect the nucleation and growth of zeolites. The most common aluminum sources are sodium aluminate, aluminum hydroxide, aluminum isopropoxide, aluminum nitrate, aluminum sulfate, and aluminum metal (foil or Al powder). It was found that different framework types can be obtained by varying the aluminum source under the same synthesis conditions.[15]

Si/Al ratio

The Si/Al ratio plays an important role in determining the structure and composition of the final zeolite. In general, low-silica zeolites are synthesized from mixtures with low Si/Al ratio and high alkalinity, while high-silica zeolites are synthesized from mixtures with high Si/Al ratio and weak alkalinity. However, there is often not a direct correlation between the Si/Al ratio of the initial mixture and the Si/Al ratio in the zeolite framework.[10]

pH

Most of the zeolites are synthesized from basic mixtures. A higher pH favors the solubility of the Si and Al sources, decreases the polymerization of the silicate anions,

and increases the polymerization of the polysilicate and aluminum anions.[7] Therefore, increasing the pH reduces the induction and nucleation times and accelerates the crystallization of the zeolite. The pH also affects the particle size of zeolites. In general, increasing the pH decreases the particle size and narrows the particle size distribution (PSD).[14] Moreover, pH can affect the morphology of zeolites. As an example, it has been previously shown that decreasing the pH promotes high aspect ratios (length/width) for MFI crystals.[16]

Water content

Water acts as a solvent in zeolite synthesis. Typically the water content is varied in the synthesis of a specific zeolite, altering the concentration of the reactants too. Thus, changing the water content can influence the final zeolite phase obtained. This effect might be related to the nucleation step, and hence, to the kinetics of the system.[17] On the other hand, dilution of the initial reaction mixture causes lower supersaturation, favoring crystal growth, and therefore the formation of large crystals.[7]

Structure directing agents (SDAs)

Inorganic cations. Some aluminosilicate zeolites can be synthesized from mixtures containing sodium and/or potassium.[18] In Table 1.5 some examples of the framework types formed in the presence of these species are shown. Flanigen suggested two roles of inorganic cations in the synthesis of zeolites.[19] The first is as a source of hydroxide ions (because the cation is typically added as a base in the MOH form) that solubilize the silicate and aluminate species. The second is as a limited structure-directing agent (SDA). Hydrated alkali-metal (M) cations such as sodium and potassium

are supposed to influence the ordering of water molecules in aqueous solution (Figure 1.8).[20] Apparently, cations play a structure-directing role breaking the original hydrogen bonds and ordering the water molecules, which can be partially replaced by silicon and aluminum tetrahedra (oxygen of tetrahedral species replaces oxygen of water) forming regions of microorganization that lead to nucleation centers.

Table 1.5 Examples of zeolite framework types synthesized from aluminosilicate systems in the presence of sodium- and/or potassium-containing species.[7]

Inorganic cation	Zeolite framework type formed
Sodium	ANA, CAN, CHA, EMT, FAU (X), FAU (Y), FER, GIS, LTA, MOR, MTT, MWW, and SOD
Potassium	EDI, KFI, LTL, MER, and TON
Sodium and potassium	BEA, low-silica-type X (FAU), NAT, OFF, PAU, and PHI

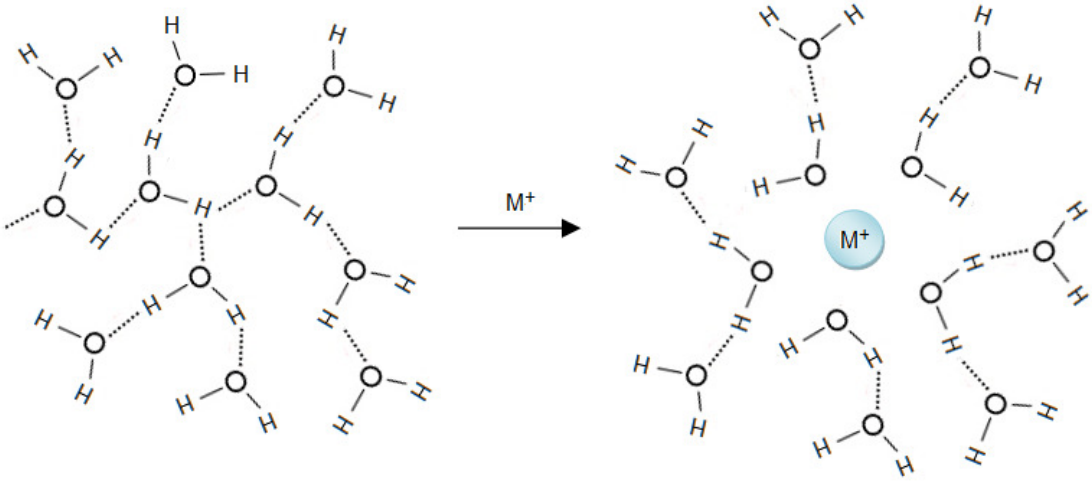

Figure 1.8 Structure directing role of alkil-metal cations in the synthesis of zeolites. Adapted from Feijen, E. J. P.; Martens, J. A.; Jacobs, P. A., Zeolites and their Mechanism of Synthesis. In *Studies in Surface Science and Catalysis*, J. Weitkamp, H. G. K. H. P.; Hölderich, W., Eds. Elsevier: Louvain-la-Neuve, **1994**.

Organic cations. Barrer and Denny first introduced an organocation, tetramethylammonium, in the zeolite synthesis achieving higher Si/Al ratio zeolite frameworks.[21] The organocation seemed to have a structure-directing role in the formation of building units. Since then other quaternary ammonium cations have been used in the zeolite synthesis. Lok et. al. defined templating as the phenomenon occurring during either gelation or nucleation, where the organocations organize the oxide tetrahedra in a particular topology around themselves providing in this way the initial building units of a specific structure.[22] They suggested that templating becomes operative only in the environment of the right "gel chemistry". Davis and Lobo clarified Lok's definition suggesting that organic molecules have a structure-directing rather than a strict templating role.[23] They summarized the role of organocations as space-filling species, structure-directing agents (SDAs), and templates. The low specificity of multiple organic cations that can direct the formation of a specific structure is associated with a space-filling role. Structure direction means that a specific structure is synthesized using a single organocation. True templating occurs when the zeolite structure adopts the geometric and electronic configuration of the organocation while retaining their shape after their removal from the framework.

SDAs or templates significantly affect zeolite formation by altering the gelation and/or nucleation process and by lowering the chemical potential of the lattice formed upon their inclusion.[20,24] Moreover, the charge density of the organocations affects the chemical composition (Si/Al ratio) of a given framework. Also, the hydrophobic character of the organocations influences the synthesis of pure-silica zeolites. More

hydrophobic cations such as tetrapropylammonium (TPA) have been shown to increase the rate of crystallization.[25]

SDAs in the synthesis of high-silica zeolites. The influence of the geometry of organic moieties on the shape and size of void spaces is more evident in the final structure of high-silica zeolites.[26] This is mainly due to two reasons. First, the mixtures for the synthesis of high-silica zeolites contain a limited number of species (i.e., a silica source, organic species, water, and low concentrations of alkali metal hydroxides). Second, the interactions between the organic cations and the silicate species can be ascribed to van der Waals forces, since high-silica zeolites are more hydrophobic and have low charge (or are uncharged in the case of pure-silica zeolites; as-made high silica zeolites have defects to satisfy charge neutrality).

Davis proposed a hypothetical mechanism for the structure direction of pure-silica ZSM-5 (Si-ZSM-5) by TPA cations.[27] This mechanism was supported by relevant experimental findings and it is depicted in Figure 1.9. Initially, the hydrophobic hydration sphere formed around the TPA cations is partially or totally replaced by silicate species. The availability of soluble silicate species affects the rate of formation of the new composites. The source of silica influences the rate of nucleation, showing enhanced rates for those mixtures containing monomeric silica (i.e., tetraethyl orthosilicate) or small amounts of alkali-metal cations. The enthalpic driving force is provided by van der Waals interactions between the alkyl groups of the organic molecules and the hydrophobic silicate species, while the additional entropic driving force is provided by the released ordered water to the bulk aqueous phase. Thus, the

geometric correspondence between the structure-directing agent and the final zeolite framework arises.

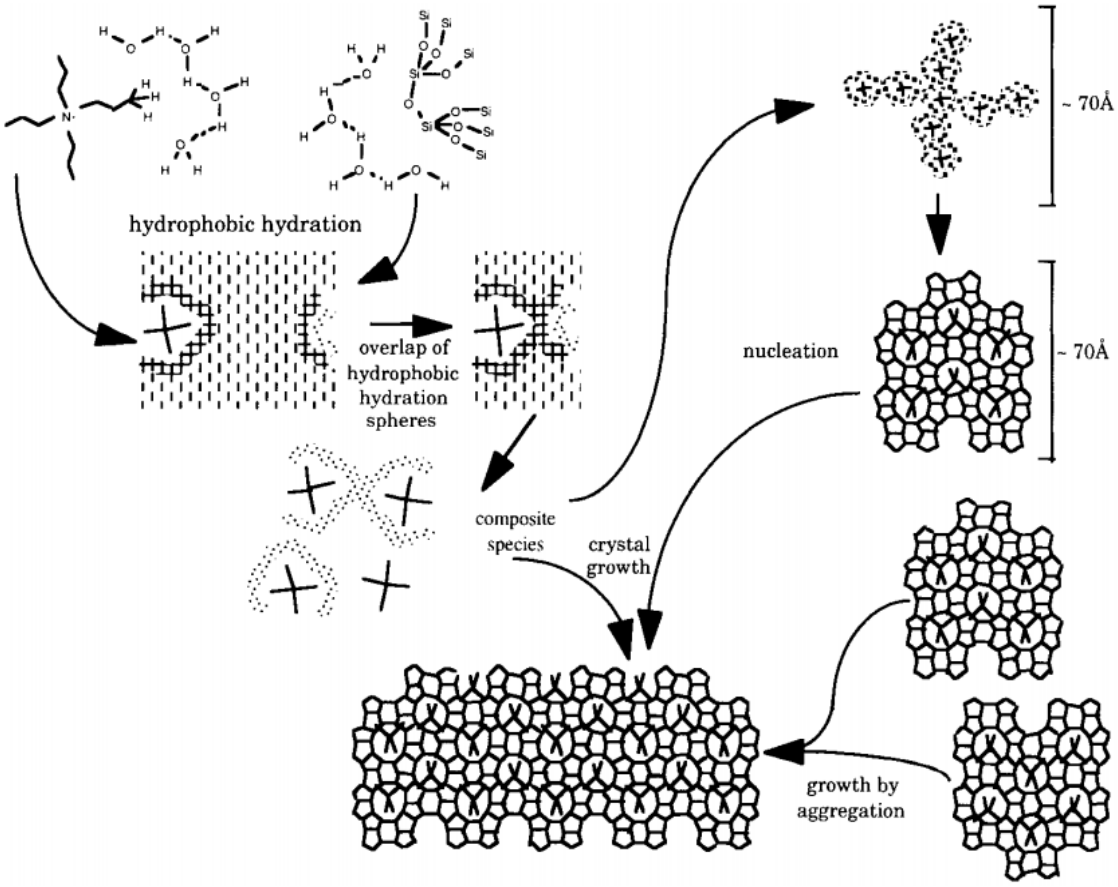

Figure 1.9 Diagram of the proposed mechanism of structure direction in the TPA-mediated synthesis of Si-ZSM-5. Reproduced with permission of Davis, M. E., Strategies for zeolite synthesis by design. In *Studies in Surface Science and Catalysis. Vol. 97*, Laurent, B.; Serge, K., Eds. Elsevier: **1995**. Copyright © 1995 Elsevier.

After the formation of the silica enclathrated TPA species, the composites form entities of size ~ 5-7 nm suggesting that nucleation centers for zeolite synthesis should be smaller than 10 nm in size. An intermediate step in the formation of the 5-7 nm entities involves the condensation of the TPA-silicate species into aggregates by

chemical interactions of silicate species. Reorganization of these aggregates leads to their densification, apparently, in order to minimize the surface energy. ZSM-5 crystal formation appears to occur via aggregation of the 5-7 nm nuclei, which surfaces serve to "template" the growth process of the crystal by using the silica enclathrated TPA as building units. However, these building units may participate in the growth process (that seems to occur in a layer-by-layer mode) in combination with free TPA that adsorbs on the crystal surfaces. Thus, the mechanism described above suggests that structure-direction is critical for the crystallization process at the nucleation stage.

SDAs in the synthesis of low-silica zeolites. The synthesis of low-silica zeolites is less amenable to structure direction by organic molecules than that of high-silica zeolites.[26] In the synthesis of low-silica zeolites the alkali metal ions balance the negative charges introduced by the aluminum species present in the framework, and even if organic cations are present, a sufficient number of them cannot be accommodated in the void space to balance the framework charges. Thus, the structure direction by organic molecules is weak relative to influences of the alkali metal hydroxides that are usually present in high concentrations and strongly affect the zeolite structure formation in the low-silica synthesis. This is probably due to the fact that the interactions between organic and inorganic species are mainly electrostatic in nature. As a consequence, the effect of the organic structure direction is only present in a narrower range of the synthesis conditions as the aluminum content increases. Thus, discerning the structure-directing effects in the low-silica zeolite syntheses is more complicated due to the complexity of these systems.

Solvents

The synthesis of zeolites is typically conducted in aqueous medium, but other solvents such alcohols can also be used. The properties of the solvent play an important role in the crystallization of zeolites, because this process is influenced by the interactions between the solvent and the reaction species (specifically the SDAs). Organic solvents have a tendency to form hydrogen bonds, which can be classified as high, high-medium, low-medium, and non-hydrogen bonding.[28] High hydrogen-bonding solvents can shield the interactions between the framework species and the SDAs preventing nucleation.

The viscosity of the solvent can also affect the size and morphology of the zeolite crystals. Solvents with higher viscosity than water can prevent convection, and therefore, the mass transfer process occurring during the crystallization will be only due to diffusion. This reduces secondary nucleation and prevents crystallization by sedimentation. In general, solvents of intermediate viscosity and hydrogen-bonding ability seem to favor the synthesis of zeolites, particularly the formation of large crystals.[28]

Aging

Aging refers to the period of time occurring between the mixing of the reagents in the initial mixture and the onset of the heating at the synthesis temperature. Several studies have shown that aging has an important effect on the nucleation and growth kinetics of zeolites.[7,29] In particular, the aging period appears to have a significant effect in low-silica zeolites, probably because they form at relatively lower temperatures than

high-silica zeolites. It is believed that the germ nuclei are formed during the aging period and remain dormant until the temperature is increased. However, the process occurring during the aging period is still unclear, but it is believed to affect the crystallization of zeolites by increasing the nucleation and growth rate, reducing the induction period, reducing the duration of crystallization, reducing the crystal size, and increasing the crystal population. Ogura et al. studied the crystallization of FAU (faujasite) zeolite framework type and found that shortening the aging time of the mixtures resulted in the formation of other phases such as SOD (sodalite), CHA (chabazite), and ANA (analcime).[30] They also found that at least 1 day of aging was needed to obtain pure-FAU, and that a sufficiently long aging period leads to a shorter crystallization time and a narrower crystal size distribution.

Stirring

Several studies have shown that stirring affects the crystallization kinetics.[31,32] Specifically, it can modify the crystal size, the selectivity for the formation of different zeolite phases, and the intergrowth of the polymorphs of some zeolites. In general, it has been observed that smaller crystals are obtained under stirring because supersaturation is rapidly achieved due to accelerated mass transfer. On the other hand, the intergrowth of polymorphs seems to be affected by fluctuations of the local concentration at the growing surface, which are due to diffusion-limited transport and produce an apparent low concentration.

Temperature

The temperature is probably one of the most important parameters in the synthesis of zeolites since it strongly affects the zeolite formation. The zeolite phase, the crystal size, and the crystal aspect ratio (length/width) are affected by the synthesis temperature. Thus, higher nucleation and growth rates, as well as larger crystals and crystal aspect ratios are obtained at higher temperatures.[33-35]

Time

Time is another important parameter in the synthesis of zeolites. In general, the crystallinity increases with time, but it should be noticed that zeolites are metastable phases that can be replaced by more stable phases following the Ostwald's rule of successive reactions.[7,36] For instance, increasing the crystallization time of zeolite A (LTA) and zeolite X (FAU) from alkaline aluminosilicate gel directs to the formation of sodalite (SOD) and zeolite P (GIS). However, it is important to keep in mind that in order to understand the zeolite formation not only the thermodynamics has to be considered, but the kinetics of the systems.

1.2.2 Routes

Many routes for the synthesis of zeolites have been developed in order to obtain zeolites with the desired properties such as specific structures, compositions, and crystal sizes. These routes include microwave assisted, hydrothermal, solvothermal, and ionothermal syntheses. The hydrothermal synthesis, which refers to reactions occurring at high temperature and pressure in aqueous solutions in a closed system, has become the

primary route for the synthesis of zeolites. However, some zeolites can be synthesized at relatively low temperature and atmospheric pressure.

The synthesis of zeolites starts with the preparation of a mixture with amorphous reactants that include, in general, a source of silica, a source of aluminum, organic species, water, and/or low concentrations of alkali metal hydroxides. Before heating, this mixture is usually aged and stirred during a certain period of time leading to the formation of a partially reacted phase that is known as a precursor mixture. The complexity of the precursor mixtures vary according with its composition. For instance, aluminum-rich mixtures are simple in the sense that mainly $Al(OH)^{-4}$ anions are present in them.[37] On the other hand, silica-rich mixtures are more complex because they contain different silicate anions that can be present as charged monomers and oligomers. The co-existence of these anions depends on the ratio of base to silica. Reorganization of the species in these precursor mixtures leads to the nucleation and growth of the zeolite crystals.

The nucleation and growth process seems to be affected by the phase nature of the precursor mixtures, which varies from gel-like to transparent liquid-like mixtures. Although the transparent mixtures have been called clear solutions by some authors, they are not single-phase but colloidal systems.[38] Therefore, they will be referred as transparent mixtures in this work. Several studies have supported the idea that nucleation occurs mainly in a gel phase, specifically at interface between the gel and the bulk mixture where the concentration gradients seems to be the highest.[39] This has also shown to be true in transparent mixtures where the nucleation seems to take place inside small

gel-like particles.[40] Zeolite growth appears to increase linearly during most of the crystallization process for both gels and transparent mixtures. However, some investigations on transparent mixtures have shown a dependence of the growth rate on the particle size for values below 15-20 nm.[41]

1.2.3 Nucleation and growth

Crystallization of zeolites generally occurs via sequential steps of nucleation followed by the growth of the nuclei to larger sizes by incorporation of the species from the bulk mixture.[18] Zeolite nucleation and growth (also referred as zeolite crystallization) has been considered as one of the most complex chemical problems,[7,42] which has been extensively studied but still not completely understood.[42-56] An overarching unresolved question in the zeolite community is to understand at a molecular level how zeolite crystals nucleate and grow from a given mixture. Getting this fundamental knowledge is not a simple task because zeolite nucleation and growth is governed by both thermodynamic and kinetic processes. It appears that the nucleation and growth rates are governed by a driving force related to supersaturation (Figure 1.10). However, supersaturation is difficult to identify in the synthesis mixtures due to the considerable large amount of species and parameters involved. In order to understand the nucleation and growth mechanisms of zeolites researches have studied model systems such as silicalite-1 and zeolite A. Some of the most important findings on these systems are summarized below.

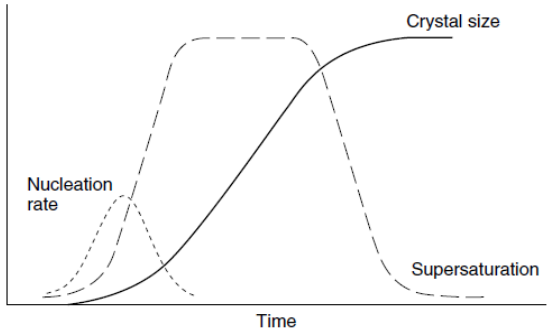

Figure 1.10 Scheme of nucleation, growth rate, and supersaturation relationship. Reproduced with permission from Cubillas, P.; Anderson, M. W., Synthesis Mechanism: Crystal Growth and Nucleation. In Zeolites and Catalysis, Wiley-VCH: Weinheim, 2010. Copyright © 2010 Wiley-VCH.

Silicalite-1

Among the studies on zeolite nucleation and growth, investigations of silicalite-1 (the pure-silica analog of ZSM-5, MFI) from mixtures of TAA cations (tetraalkylammonium cations), TEOS (tetraethyl orthosilicate), and water that are transparent to the eyesight dominate the literature.[23,38,43-46,50,55,57-70] The silicalite-1 synthesis has been chosen as a model synthesis because it is robust and chemically simple, and forms MFI (an important industrial catalyst) under a wide range of conditions.[44,71] Moreover, the transparent nature of the mixtures facilitate the use of scattering techniques,[38,42-46,50,52,53,55,58-69,72-84] NMR spectroscopy,[58,85-94] calorimetry,[38,49,54,55,81,92,95,96] and electron microscopy.[59,64,97,98] Among these techniques, NMR spectroscopy has shown to be particularly useful because of its non-invasive nature.

Before the late 1990s, the investigations of silicalite-1 nucleation and growth were mainly focus on three major topics: 1) the investigation of silicalite-1 growth using

scattering techniques, 2) the development of so-called "guest-host" interactions, and 3) the investigation of silicate speciation using liquid ^{29}Si NMR. The investigations of de Moor et al, Iton et al., Watson et al., and Schoemann et al.[23,42,51-53,73-78,82,84,99,100] on the silicalite-1 growth using scattering techniques are particularly notable. Their work showed the presence of small (<5 nm) ellipsoidal core-shell nanoparticles in the precursor mixtures that consists of a silica core and a cation shell.[42,43,50,52,60,61,65,68,82] They also showed that these nanoparticles (also referred as precursor particles) grow in size upon heating the precursor mixtures at ~ 100°C leading to the formation of small (<100 nm) particles with a zeolite crystal structure.[46,69,82] Davis et al., Gies et al., Goretsky et al., Kubota el al., Lobo et al., Petrovic et al., Rollman et al., Zones et al., Chevron, and Mobil Oil Co. (now ExxonMobil) investigated the second topic on the "guest-host" interactions.[23,25,57,101-108] They characterized high-silica zeolites including ZSM-5 to understand how the organocation nature correlates with the final zeolite topology obtained after synthesis. Burkett et al. were the first to show the organocation-silica association in partially formed zeolites by NMR, making in this way contributions to the first and second topics.[26,109] Harris et al.,[110-114] Kinrade et al.,[89,90,115-119] and Knight et al.,[92,120-122] studied silicate speciation using liquid ^{29}Si NMR. They showed that parameters such as pH, solvents, and SDAs influence the silicate speciation. The main conclusion of their NMR work was that the organic molecules do not cause unique speciation of silicate species in liquid mixtures (i.e., formation of double-five associated rings found in the final zeolite structures). As it is going to be explained below, this conclusion based on the NMR experiments have been controversial. The main

disagreement arose in the late 1990s when the Leuven's group[85,94,123-130] proposed a different morphology for the 5 nm precursor particles. They claimed that these precursor particles observed in previous works[42,43,50,52,60,61,65,68,82] had a well-defined structure with MFI framework topology and a TPA in each channel intersection. Their hypothesis has been referred as the "nanoslab" model. However, further investigations by Knight et. al., Fyfe et al., and Cheng and Shantz (using NMR),[58,86,93,131] Ramanan et al. (using transmission electron microscopy, TEM),[98] Cheng and Shantz., Fedeyko et al., Kragten et al., Kumar et al., and Rimer et. al., and Yang et al. (on the characterization precursor particles)[44-46,54-56,60,61,63,64,67-69] have proven and supported the conclusion of the original reports that the precursor particles are in fact amorphous. The correct interpretation of the experimental data in order to propose the morphology of the precursor particles has an important impact in the development of an accurate molecular-level description for the nucleation and growth of silicalite-1 and other zeolites. Based on the evidence presented in previous works, the author of this dissertation agrees on the existence of precursor particles with a silica core and a cation shell.

Zeolite A

Another zeolite that has been commonly chosen as a model system for the understanding of the nucleation and growth mechanisms is zeolite A. The crystallization behavior of this zeolite has been well established and the time and conditions of the synthesis are known to be reasonable.[132] The mechanism for the formation and growth of crystal nuclei of zeolite A proposed by Bein et al. is depicted in Figure 1.11.[40] Bein et al. studied the synthesis of zeolite A from transparent mixtures at room temperature using

high-resolution transmission electron microscopy (HRTEM) and in situ dynamic light scattering (DLS). They proposed that small particles of ~5 nm contained in the aluminosilicate mixtures rapidly agglomerate after the addition of the organic molecules to give amorphous gel particles of 40-80 nm. Then, single zeolite A crystals nucleate in these amorphous gel particles within 3 days at room temperature. Because only one crystal was observed per gel particle, they concluded that aggregation of nuclei is not required for crystallization and that the driving force for nucleation should be supersaturation within the amorphous phase. This process results in single crystals of 10-30 nm embedded in the amorphous gel particles. The amorphous gel phase seems to be consumed during further crystal growth at room temperature, forming a colloidal suspension of 40-80 nm zeolite A crystals. Significant growth of these crystals is observed after heating this suspension at 80°C.

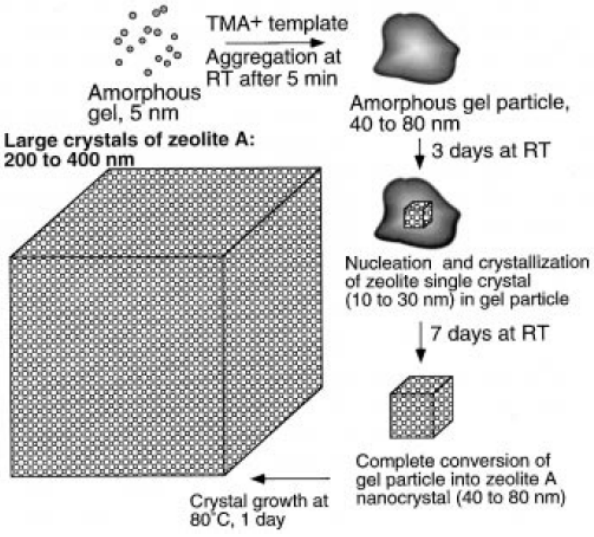

Figure 1.11 Proposed mechanism for the formation and growth of zeolite A crystal nuclei. Reproduced with permission from Mintova, S.; Olson, N. H.; Valtchev, V.; Bein, T., *Science* **1999**, 283 (5404), 958-960. Copyright © 1999 American Association for the Advancement of Science.

1.3 Dissertation scope and structure

It can be inferred from the introduction presented above that interactions between the organic (i.e., organocations) and inorganic (i.e., silicon or aluminum) molecules occurring during the zeolite synthesis play an important role in determining the ultimate structure of the zeolite. However, most of the previous studies have only provided information about the structure of the species involved in the zeolite synthesis. Although the findings from these studies are important, information related to the strength of organic-inorganic interactions has remained basically absent. Specifically, determination of the organic-inorganic interaction strength (i.e., the adsorption Gibbs energy between the organic and inorganic species) from transparent synthesis mixtures is needed. Achieving this goal from experimental investigations is not trivial. However, pulsed-field gradient (PFG) NMR spectroscopy offers a potential tool in this regard since it is non-invasive and sensitive to the motion of species in liquid mixtures. Therefore, **the objective of this work is to determine the strength of organic-inorganic interactions in transparent synthesis mixtures using PFG NMR spectroscopy.** The outcome information of this work should contribute to a more detailed molecular-level description of the nucleation and growth process occurring between the initial multi-component mixture and the final zeolite phase. This molecular description is expected to be used for the development of predictive models for the rational design and control of the properties of zeolites. In a broader scope, this information would represent a pinnacle achievement in zeolite science that would allow the emergence of a new generation of materials by design.

The experimental methods used to satisfy the objective of this dissertation are described in Chapter II. In this chapter, the general approach of this work as well as basic concepts of nuclear magnetic resonance (NMR) spectroscopy, dynamic light scattering (DLS), X-ray diffraction (XRD), conductivity, and pH are discussed. A PFG NMR investigation of the organocation role in precursor mixtures of silicalite-1 is presented in Chapter III. Then, an in situ PFG NMR of silicalite-1 synthesis mixtures is discussed in Chapter IV. A systematic investigation of silicalite-1 precursor mixtures with varying degrees of dilution is presented in Chapter V. A summary of the findings and the conclusion of this work are presented in Chapter VI. Finally, recommendations for future investigations based on the results presented in this dissertation are discussed in Chapter VII.

CHAPTER II

EXPERIMENTAL METHODS

In order to achieve the objective of this work the general approach illustrated in Figure 2.1 has been followed. First, the organocation self-diffusion coefficients have been determined using PFG NMR spectroscopy. Also, other significant information about the species in the liquid mixtures has been determined using other NMR methods besides PFG. Second, the fraction and amount of organocations bound to the silica particles have been calculated through a two-site model analogous to the one proposed by Choudhury and Schönhoff.[133] These parameters have been used to generate the adsorption isotherms. Third, the adsorption isotherms have been fitted with model isotherms and the adsorption energy has been calculated from the fitting parameters. Finally, other relevant information of the studied systems has been obtained through dynamic light scattering (DLS), X-ray diffraction (XRD), and/or conductivity and pH measurements.

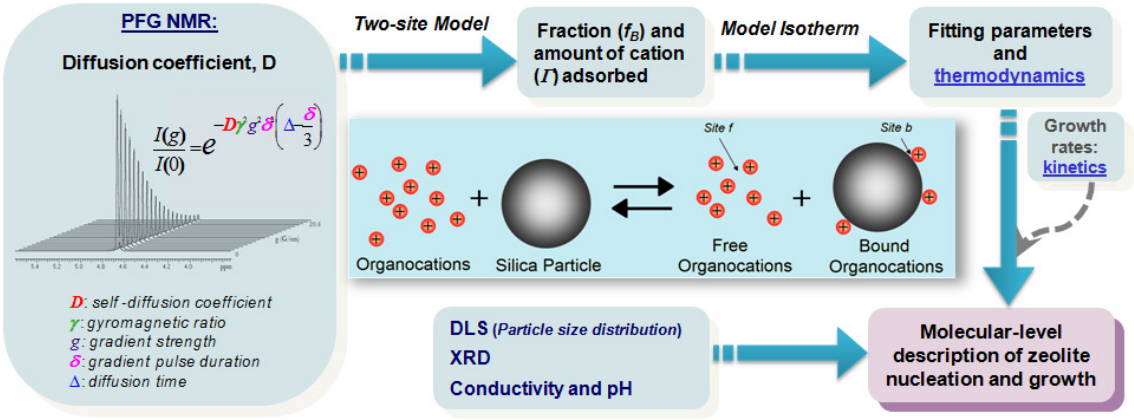

Figure 2.1 Diagram of the general approach of this work.

Basic concepts of the experimental methods that are relevant to analyze and discuss the results of this work are given in this chapter. Background on NMR spectroscopy is emphasized in this chapter because this is the main experimental technique used in this work.

2.1 Nuclear magnetic resonance

Nuclear magnetic resonance (NMR) spectroscopy is a powerful technique for zeolite characterization. Virtually every chemical element contained in zeolites has an isotope that can be studied with NMR spectroscopy. This attribute allows elucidating the molecular structure of zeolites. In this work, NMR spectroscopy has been used to determine interactions between the species within the synthesis mixtures by measuring the diffusion coefficients of the organocation, and how these values are perturbed in the presence of silica.

2.1.1 Basic principles

NMR is based on the fact that nuclei of atoms have magnetic properties that can provide information on the structure, motions, and chemical reactions of the molecules. These magnetic properties are connected with the magnetic moment μ of a nucleus, which is related to its angular momentum $\boldsymbol{P}$ and overall nuclear spin I through the equation

$$\mu = \gamma \boldsymbol{P} = \gamma \hbar \sqrt{I\left(I+1\right)} \tag{2.1}$$

where γ is the gyromagnetic ratio and $\hbar$ is the reduced Planck's constant. Thus, a nucleus with an overall spin $I = 0$ has no nuclear magnetic moment and, therefore, cannot be

observed by NMR spectroscopy. Fortunately, most elements possess at least one isotope with a non-zero nuclear spin that is observable with NMR spectroscopy.

The angular momentum ***P*** of a nucleus takes up an orientation if the nucleus is placed in a static magnetic field $\boldsymbol{B_0}$. This behavior of the nucleus in a magnetic field is called directional quantization and it is depicted in Figure 2.2.[134] The direction of the magnetic field is conventionally represented in the z-axis and the component of the angular momentum along this direction is given by

$$P_z = m\hbar \tag{2.2}$$

where m is the magnetic or directional quantum number and can take values of I, I-1, …$-I$. There are $(2I+1)$ different values of m, and therefore, the same number of possible orientations of the angular momentum and the magnetic moment. Thus, two orientations are allowed for protons (^{1}H), which have $I = 1/2$.

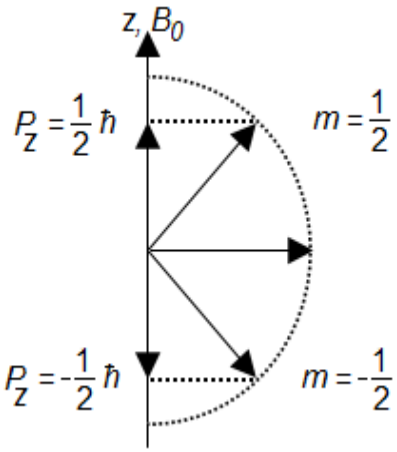

Figure 2.2 Directional quantization of the angular momentum ***P*** for a nucleus with $I = 1/2$ in a magnetic field $\boldsymbol{B_0}$. Reproduced with permission from Friebolin, H., *Basic One- and Two-Dimensional NMR Spectroscopy*. Wiley-VCH: Weinheim, **1998**. Copyright © 1998 Wiley-VCH.

The nuclear dipoles precess around the z-axis resembling a spinning top (Figure 2.3). The precession frequency or Larmor frequency ν_L is given by

$$\nu_L = \left|\frac{\gamma}{2\pi}\right| B_0 \tag{2.3}$$

where B_0 is the magnetic flux density. The energy of a magnetic dipole in a magnetic field is

$$E = -\mu_z B_0 = -m\gamma\hbar B_0 \tag{2.4}$$

where μ_z is the z-component of the nuclear magnetic moment. Therefore, the energy difference between two adjacent levels of energy is

$$\Delta E = \gamma\hbar B_0 \tag{2.5}$$

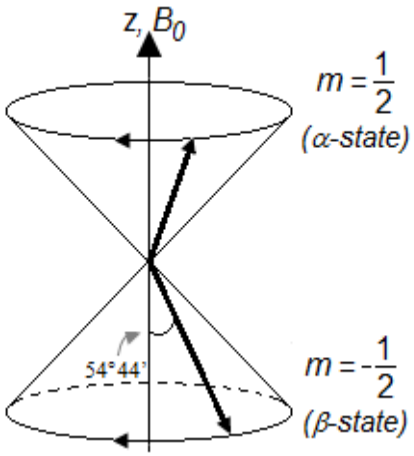

Figure 2.3 Precession of nuclear dipoles with I = 1/2 around a double cone. Reproduced with permission from Friebolin, H., *Basic One- and Two-Dimensional NMR Spectroscopy*. Wiley-VCH: Weinheim, **1998**. Copyright © 1998 Wiley-VCH.

A macroscopic sample, such as the actual samples used in NMR experiments, consists of an ensemble of spins rather than a single spin. Therefore, the distribution of the spins between different states is described in terms of classical mechanics rather than

quantum mechanics. If a single spin was considered, a quantum mechanics formalism would be required because atomic phenomena do not behave classically.[135] However, the distribution of the spins between states for nuclei with I = 1/2 can be described by Boltzmann statistics as follows

$$\frac{N_\beta}{N_\alpha} = e^{-\Delta E/k_B T} \approx 1 - \frac{\Delta E}{k_B T} \tag{2.6}$$

where N_β is the number of nuclei in the upper level of energy, N_α is the number of nuclei in the lower level of energy, k_B is the Boltzmann constant, and T is the absolute temperature in K. The difference between populations in the lower and upper energy levels is very small, being the excess in the lower level of energy in the order of parts per million (ppm). This small difference in populations makes of NMR an inherently insensitive tool. However, the observation of the bulk magnetization $\boldsymbol{M}$ along the direction of the magnetic field is possible when the z-components of all the nuclear magnetic moments of the spins in a sample are added.

In Figure 2.4 the main components of an NMR experiment for nuclei with I = 1/2 are summarized. In the absence of an external magnetic field the nuclear spins are randomly oriented. However, in the presence of an external magnetic field they adopt one of the allowed orientations; these states are separated by an energy difference ΔE, which depends on the interaction between the nuclei and the magnetic field. A radiofrequency (RF) field is applied to the sample in order to induce transitions between states. The RF field is then turned off and the system is allowed to return to equilibrium. Transitions will only occur if the frequency from the RF field ν_1 matches the Larmor

frequency ν_L. This match in frequencies is called the resonance condition. The transitions are then detected as a signal, whose intensity is proportional to the population difference between the lower and upper energy levels. However, if the populations are exactly equal transitions from the lower to the upper level (absorption process) and from the upper to the lower level (emission process) cancel each other and no signal is observed. This condition is called saturation. The detected signal is called the FID (free induction decay) and it can be Fourier transform to see the spectrum in the frequency domain.

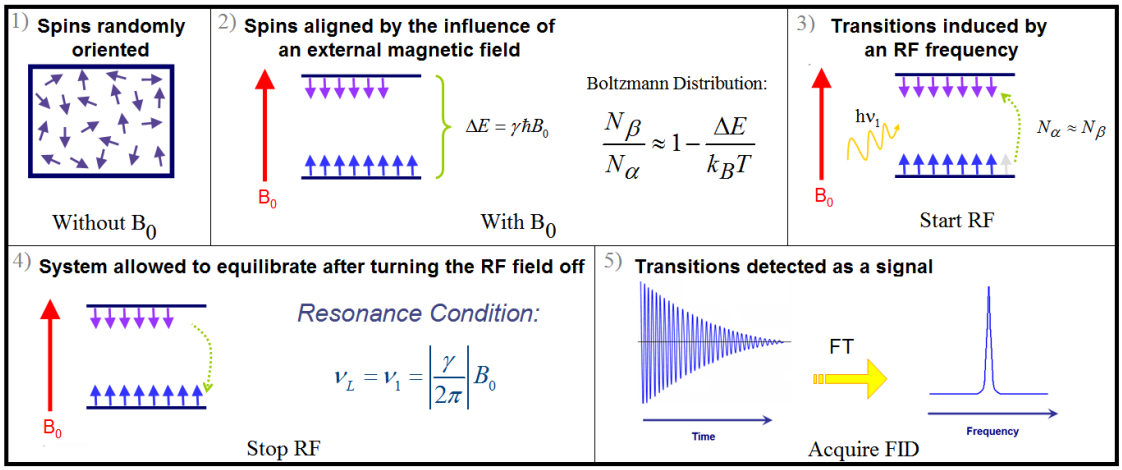

Figure 2.4 Basic principles of an NMR experiment represented for nuclei with $I = 1/2$.

One important parameter in NMR spectroscopy is the chemical shift. This parameter describes the position of the resonances in an NMR spectrum. The absolute position of a resonance varies with the strength of the magnetic field used in the experiment. In order to avoid that the position of the peaks would be instrument-dependent, the frequency of a resonance (in Hz) is calculated as a shift from the

frequency of a reference compound and divided by the resonance frequency of the nucleus. Thus, the chemical shift δ is defined as

$$\delta = \frac{\nu_{sample} - \nu_{reference}}{\nu_{sample}} \times 10^6 \tag{2.7}$$

where ν_{sample} is the sample frequency and $\nu_{reference}$ is the reference frequency. The factor 10^6 is introduced to simplify the numerical values because the chemical shifts are always given in parts per million (ppm). The chemical shift depends on the chemical environment of the nucleus. Thus, depending on the chemical environment, the same isotope shows different chemical shifts corresponding to differences between resonances in the order of Hz to kHz.[136] This phenomenon arises from the fact that the nuclei are shielded by their electrons, which introduce a secondary magnetic field opposing the applied magnetic field. Thus, different chemical groups (e.g., aliphatic versus aromatic protons) resonate at different frequency and have different chemical shifts. Therefore, the chemical shift can be used as a fingerprint to identify the nature of the nucleus, which makes NMR spectroscopy a powerful tool for scientists.[134]

2.1.2 Relaxation: T_1 and T_2

Relaxation describes the processes by which the bulk magnetization caused by the population difference between two spin states returns to the equilibrium. The relaxation processes can be described by two different relaxation times, which are given by the Bloch equations in terms of classical mechanics. The spin-lattice or longitudinal relaxation time T_1 is the relaxation in the applied field direction and depends on the molecular motions. Bloch described this process by the following differential equation[134]

$$\frac{dM_z}{dt} = -\frac{M_z - M_0}{T_1} \tag{2.8}$$

where M_z is the z-component of the bulk magnetization vector $\boldsymbol{M}$, t is the time, and M_0 is the equilibrium value of the bulk magnetization vector $\boldsymbol{M}$. The spin-lattice relaxation is always related with a change in the energy of the spin system, as the energy absorbed from the RF pulse must be emitted back again.

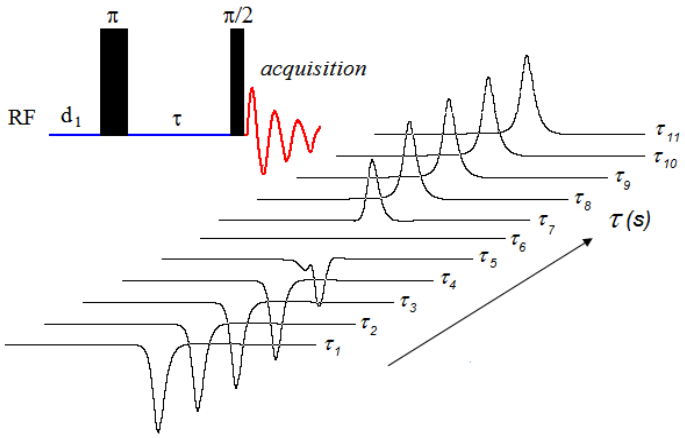

Figure 2.5 Inversion recovery pulse sequence and a series of spectra showing one signal obtained after applying the sequence with eleven different values of the time delay between pulses τ. The first delay of the sequence is d_1.

The most common method for experimental determination of the spin-lattice relaxation time T_1 is called inversion recovery. In this method a series of spectra are recorded using a [$\pi - \tau - \pi/2 -$ *acquisition*] pulse sequence (Figure 2.5). The π (180°) pulse brings the magnetization in the negative direction of the z-axis. During the delay time τ, the system relaxes at a rate constant $R_1 = T_1^{-1}$. After the delay time τ the z-component of the magnetization is rotated by the $\pi/2$ (90°) pulse in order to generate a transverse component of the magnetization that can be observed. The delay time τ

between the π and π/2 pulses is set at different values for each spectrum as is shown in Figure 2.5. As the delay time τ varies the intensity of the signals changes too. Integration of Eq. 2.8 and substitution of the magnetization terms by intensities allows quantifying the spin-lattice relaxation time T_1 from the inversion recovery experiment

$$\frac{I_\tau}{I_0} = 1 - 2\exp\left(-\frac{\tau}{T_1}\right) \tag{2.9}$$

where I_τ is the intensity at $t = \tau$ and I_0 is the maximum measurable signal intensity.

The spin-spin or transverse relaxation time T_2 is the relaxation perpendicular to the applied field direction. Bloch described the evolution of the spin-spin relaxation by the following differential equation[134]

$$\frac{dM_{y'}}{dt} = -\frac{M_{y'}}{T_2} \tag{2.10}$$

where $M_{y'}$ is the y'-component of the bulk magnetization vector $\boldsymbol{M}$, t is the time, and the y'-axis rotates at the Larmor frequency of the nuclei. The energy of the spin system is not affected by the spin-spin relaxation because the population levels are not affected. Only the phase coherence between the precessing spins is lost. Therefore, this relaxation is associated with an entropy process.One of the most used methods for experimental determination of the spin-spin relaxation time T_2 is the Carr-Purcell-Meiboom-Gill (CPMG) experiment. In this experiment a series of spectra are recorded using a [$\pi/2 - (\tau - \pi - \tau)_n - acquisition$] pulse sequence (Figure 2.6). The π/2 (90°) brings the magnetization in the y'-axis (transverse magnetization). Due to the field inhomogeneities each nucleus experiences slightly different magnetic fields, and therefore, it precesses at slightly different rates than other nuclei in the analyzed sample.

Thus, after a delay time τ the nuclear spins have gradually lost their phase coherence. Then, a π (180°) pulse is applied to produce the reflection of the spins in the plane perpendicular to the y'-axis, without changing their direction of rotation. Doing this allows the spins to recover their phase coherence after a further delay time τ. However, the resultant transverse magnetization points now in the opposite direction as compared with the initial transverse magnetization generated after the first $\pi/2$ pulse. The ($\tau - \pi - \tau$) part of the sequence is repeated n number of times producing n number of echoes with alternating phases differing by 180°. The decay in the intensity of these echoes is determined by T_2. Integration of Eq. 2.10 and substitution of the magnetization terms by intensities allows determination of the spin-spin relaxation time T_2 from the CPMG experiment

$$\frac{I_\tau}{I_0} = \exp\left(-\frac{\tau}{T_2}\right) \tag{2.11}$$

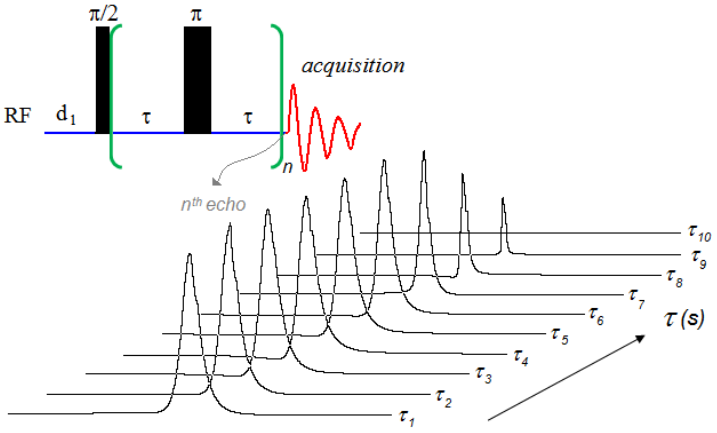

Figure 2.6 Carr-Purcell-Meiboom-Gill (CPMG) pulse sequence and a series of spectra showing one signal obtained after applying the sequence with ten different values of the time delay τ. The first delay of the sequence is d_1.

2.1.3 Diffusion NMR: pulsed-field gradient (PFG) methods

While the chemical shift parameter described in section 2.1.1 is the best-known attribute of NMR, much other information can be obtained from NMR spectroscopy. Among that information, the ability to measure the self-diffusion coefficients of species in liquid mixtures is relevant to this work. Although, it is possible to determine this quantity from spin-lattice relaxation time measurements,[137] the application of field gradients along the sample is a more straightforward and reliable way to achieve this goal. Starting with Stejskal and Tanner, pulsed-field gradients were introduced into a standard spin-echo sequence giving rise to the pulsed-gradient spin echo (PGSE) experiments and achieving more sensitivity to diffusion compared with constant gradient methods.[138]

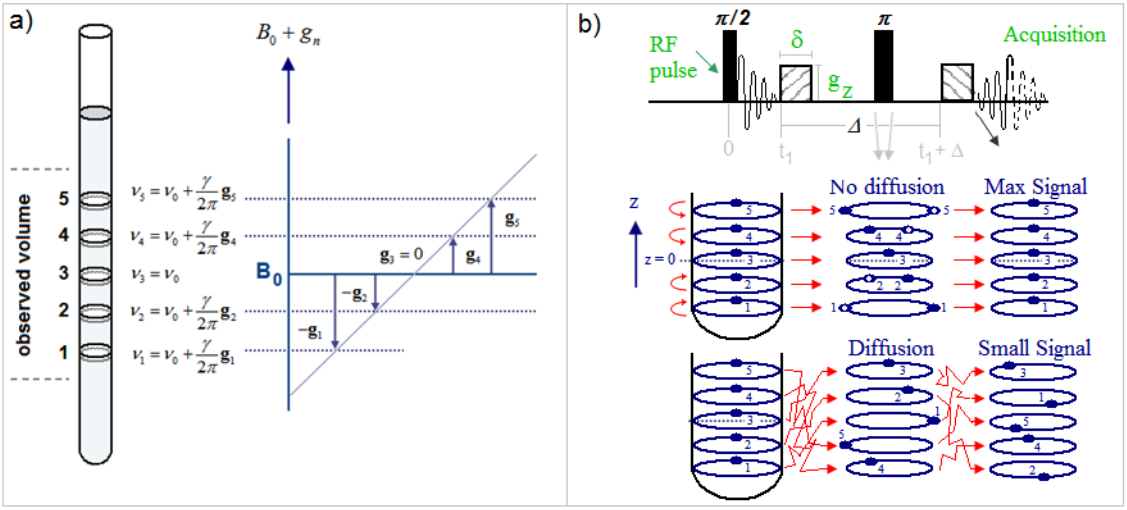

Figure 2.7 Basic principles of the PFG NMR methods: a) effect of the pulse field gradients and b) diffusion measurement by the PGSE pulse sequence. a) Reproduced with permission from Friebolin, H., *Basic One- and Two-Dimensional NMR Spectroscopy*. Wiley-VCH: Weinheim, **1998**. Copyright © 1998 Wiley-VCH. b) Adapted with permission from Price, W. S., *Concepts in Magnetic Resonance* **1997**, 9 (5), 299-336. Copyright © 1997 John Wiley & Sons.

In Figure 2.7 the principle of pulse field gradient (PFG) methods is depicted. The effect of pulse field gradients is showed in the left side of this figure. For most of the NMR experiments is normally desired to keep the magnetic field throughout the observed volume of the sample as homogeneous as possible. In contrast, in a PFG experiment pulsed-field gradients are used to intentionally introduce inhomogeneities in the magnetic field in such a way that the nuclei within the observed volume experience different field strengths depending on their positions. Using gradient coils, a linear gradient is applied along the direction of $\boldsymbol{B_0}$ (usually the z-axis) so that the additional field contribution at the center of the sample volume is zero. Thus, the precession frequencies at different positions will be given by

$$\boldsymbol{\nu_n} = \frac{\gamma}{2\pi}\left(\boldsymbol{B_0} + \boldsymbol{g_n}\right) = \nu_0 + \frac{\gamma}{2\pi}\boldsymbol{g_n} \tag{2.12}$$

where $\boldsymbol{\nu_n}$ are the precession frequencies, $\boldsymbol{g_n}$ are the additional field contributions at different positions, and ν_0 is the original precession frequency before introducing inhomogeneities in the magnetic field.[134] In the right side of Figure 2.7 it is illustrated how the PGSE experiment measures the self-diffusivity. First, a 90° (π/2) RF pulse brings the magnetization into the transverse plane (x-y plane). At time t_1 a gradient of strength g and duration δ is applied changing the frequencies of the nuclei along the z-axis. The system evolves during a time Δ, also known as diffusion time; then, an opposite gradient with identical magnitude $-g$ (g after a 180° pulse) is applied. If the nuclei remain in their same positions during the diffusion time the effects of the two applied gradients are cancelled. In this case, the phase differences are reversed and the

magnetization is completely restored. However, if the nuclear spins undergo translational motion along the z-axis the effects of the gradients are not cancelled and the magnetization is not totally restored causing the observation of an attenuated signal.[138,139]

In the PFG experiment, a measured signal intensity attenuation as the one shown in Figure 2.8 is given by

$$\frac{I_g}{I_0} = \mathbf{exp}\left[-D\gamma^2 g^2 \delta^2 \left(\Delta - \frac{\delta}{3}\right)\right] \tag{2.13}$$

where I_g/I_0 is the attenuation of the signal (the intensity at a given value of g, I_g, relative to the maximum intensity, I_0), D is the translational self-diffusion coefficient, γ is the gyromagnetic ratio of the nucleus, g is the gradient strength, δ is the duration of the gradient pulse, and Δ is the diffusion time. Thus, for given values of the experimental parameters γ, g, δ, and Δ, a plot of ln (I_g/I_0) versus g^2 allows the calculation of the diffusion coefficient from the slope.

Although the PGSE technique allows the calculation of the self-diffusion coefficients, the spin-spin relaxation rate ($R_2 = 1/T_2$) is often faster than the spin-lattice relaxation rate ($R_1 = 1/T_1$), which limits the effective diffusion time and the accessible range of diffusion coefficients.[140] This disadvantage can be overcome with the use of PFG stimulated-echo techniques. Also, in cases where multiplets are present in the spectrum, a stimulated echo is preferable because yields to much more sensitivity than a PGSE experiment.[140,141]

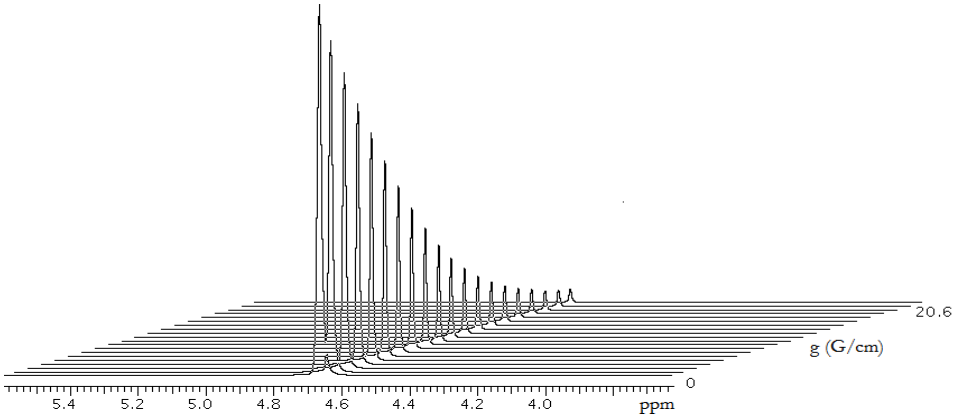

Figure 2.8 Signal attenuation observed in the PFG NMR experiments.

Diffusion ordered spectroscopy

Diffusion ordered spectroscopy (DOSY) is the two-dimensional version of the PGSE experiment.[142] This technique introduced by Johnson and coworkers has the advantage of being able to virtually separate in a 2D data matrix all the compounds of a mixture based on their different diffusion coefficients.[143-147] However, the extraction of the decay constants from DOSY data and their transformation into a 2D plot is not trivial and requires special mathematics that have been described in detail elsewhere.[94] Fast Fourier transformation (FFT) of the time domain is used to calculate the chemical shift of the signals whereas inverse Laplace transformation (ILT) of the signal decay data is used to calculate the diffusion coefficients. The DOSY processing results in a 2D plot that displays the chemical shift along the x-axis and the diffusion coefficients along the y-axis (Figure 2.9).[143,144,147-153] In this work the Dbppste (DOSY bipolar pulse pair stimulated echo) and Dbppste_cc (DOSY bipolar pulse pair stimulated echo with convection compensation) sequences has been used. In addition to the advantages of DOSY and stimulated echo experiment, the bipolar pulse pairs of these sequences reduce

the need of phase cycling (a method by which unwanted signals are eliminated based on their phase properties), improve the line shape and can be useful to eliminate the modulation introduced by chemical exchange.[154] The details of these two sequences as well as the parameters used in the experiments will be described in the next chapters.

DOSY has shown to be a powerful tool for the study of molecular interactions and systems involving binding.[145,150,155] This characteristic and the advantages mentioned above make DOSY an attractive technique for the investigation of the organic-inorganic interactions in transparent synthesis mixtures. Nevertheless, only one report was found to use this technique on the investigation of the TEOS (tetraethyl orthosilicate) hydrolysis during the first stages of the silicalite-1 synthesis.[94] DOSY has been the main experimental technique employed in the present work and its use for the calculation of the organocation-silica strength was basically introduced with this research project.

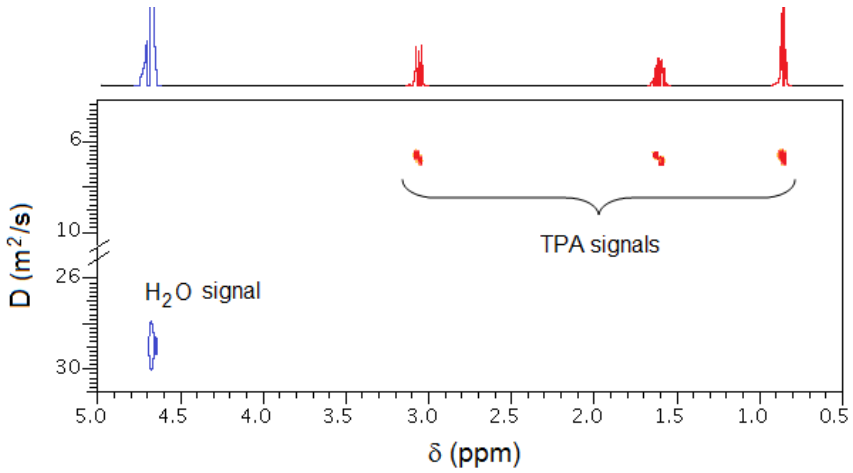

Figure 2.9 Typical 2D map obtained from DOSY experiments. The compounds in a solution of tetrapropylammonium (TPA) hydroxide in deuterated water (1 D_2O: 9 H_2O) are separated based on their diffusion coefficients. The standard ^1H spectrum is showed on top of the 2D map.

2.2 Dynamic light scattering

Determination of the size and distribution of the silica particles in the synthesis mixtures is relevant to this work. Dynamic light scattering (DLS), which is also referred as photon correlation spectroscopy (PCS) or quasi-elastic light scattering (QELS), is a widely used technique allows determining the size of particles (typically in the submicron region) or the distribution of particles that are suspended in solutions.[156,157] Particles suspended in a liquid undergo Brownian motion, which is the random movement of the particles due to the bombardment by the solvent molecules that surround them. DLS measures the Brownian motion of the particles (usually suspended within a liquid) and relates it to the size of the particles. The velocity of the Brownian motion is defined by the translational diffusion coefficient (D), and it is related to the size of the particle through the Stokes-Einstein equation

$$d_H = \frac{k_B T}{3\pi\eta D} \tag{2.14}$$

where d_H is the hydrodynamic diameter, k_B is the Boltzmann's constant, T is the absolute temperature, D is the translational self-diffusion coefficient, and η is the viscosity of the medium. The hydrodynamic diameter is defined as the diameter of a hard sphere that has the same translational diffusion coefficient that the probe particle and includes any materials attached to the particle surface (Figure 2.10). Eq. 2.14 allows inferring that larger particles will have smaller diffusion coefficients (and therefore, will move slower) and that the temperature should be kept as accurate and stable as possible during a DLS experiment in order to get reliable results.

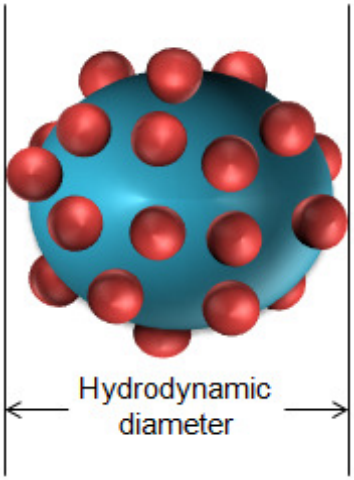

Figure 2.10 Scheme of the hydrodynamic diameter of a particle.

In a DLS measurement a holder (cuvette or cell) containing the sample is illuminated by a laser with wavelength λ (Figure 2.11). The moving particles scatter light depending on their size and the scattered light intensity fluctuates with the time carrying information about the diffusion.[158] The intensity is recorded and compared with itself at different times using a correlator. In this way the correlator constructs a correlation function $G(\tau)$ of the scattered intensity

$$G(\tau_c) = \langle I(t).I(t+\tau_c) \rangle \tag{2.15}$$

where τ_c is the correlator time delay. This correlation function of the light signal fluctuations can be written as an exponential decay (or a sum of exponential decays in the case of polydisperse samples) that is a function of the characteristic decay time (Γ_c) given by

$$\Gamma_c = Dq^2 \tag{2.16}$$

where $q = (4\pi n_{RI}/\lambda)\sin(\theta/2)$, n_{RI} is the refractive index of the medium, λ is the wavelength of the laser beam, and θ is the scattering angle. The correlation function encodes important information about the sample. The time at which the correlation starts to decay is an indication of the mean size of the particles whereas the slope of the decay correlates with their polydispersity. In polydisperse multimodal samples, the correlation function can be analyzed with several algorithms such as CONTIN (constrained Laplace inversion) and NNLS (non-negative constrained least squares) in order to determine the size and distribution of the particles in suspension. NNLS has shown to provide more accurate results as compared with other common algorithms used for the analysis of polydisperse multimodal samples (such as CONTIN)[159-161] and it has been used in this work to analyze the correlation functions.

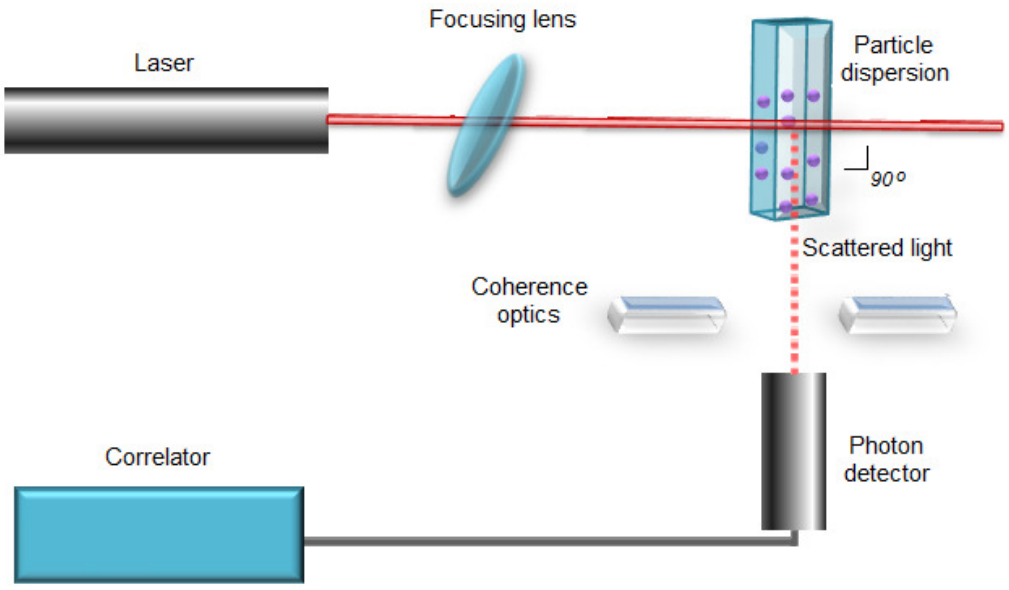

Figure 2.11 Scheme diagram of a conventional 90° DLS instrument.

The preparation of the sample is very important for a DLS measurement. Dusty liquids can limit the reproducibility of results. Dust distorts the baseline, broadens the distribution, and can ultimately affect the fitting of the correlation function. Dust is primarily a problem in highly polar liquids, especially water. Therefore, it is suggested to purify the solvent, clean the sample holder, and prepare the suspension adequately before running a DLS experiment.

2.3 X-ray diffraction

X-ray diffraction (XRD) is the most common technique used for identification of new zeolitic materials, verification of zeolite crystallinity, and/or monitoring of post-synthesis treatment effects. X-ray diffraction provides information about the way that atoms are geometrically arranged in the zeolite crystals.[162] However, most zeolite syntheses do not provide big enough crystals suitable for single-crystal X-ray diffraction analysis. Fortunately, individual crystals about the size of grains of fine powder can be used instead of single crystals. Although some information is lost with powder X-ray diffraction (PXRD), this method has proved to be useful in those cases where single crystals are not available. Data from PXRD experiments contain features that provide important information about the zeolite (Table 2.1).[18] In this work, PXRD is used to verify the crystalline zeolite phase by comparing the peak positions obtained by this technique with standard zeolite patterns.[18]

Table 2.1 Features and information contained in PXRD data.

Feature	Information
Peak positions	Unit cell dimensions
Width of peaks	Crystallite size
Peak intensities	Crystal structure
Background	Presence or absence of amorphous materials
Non-indexable peaks	Presence of crystalline impurities
Systematically absent reflections	Symmetry

In a crystalline solid the atoms are arranged in patterns which are characterized by periodic repetition in three dimensions.[162] The smallest volume element that holds the symmetry and structural information of the crystal is called unit cell. The dimensions of a unit cell can be described by three axes (*a*, *b*, *c*) and the angles between them (α, β, γ). Thus, the entire crystal structure can be envisioned as a lattice that results from stacking several unit cells together.

The crystal lattice can be described by points, rows, and planes[163] as shown in Figure 2.12. The lattice points are denoted without brackets while the lattice rows are identified in brackets. The lattice planes are defined in terms of Miller indices, which are reciprocals of the intercepts of the planes on the coordinate axes. The Miller indices are defined by three integers written in enclosed parentheses as (*hkl*). For instance, the plane illustrated in Figure 2.12 has intercepts 1a, 1b, and 2c with reciprocals 0.5, 0.5, and 1. Thus, the Miller indices of this plane are (1 1 2).

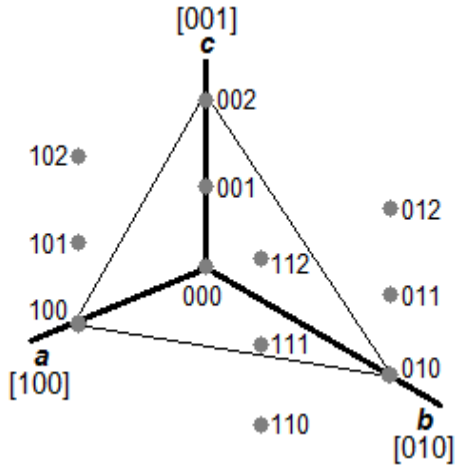

Figure 2.12 Notation of lattice points, rows, and planes.[163]

In the PXRD experiment an x-ray beam interacts with the crystalline powder generating scattering of the x-rays in two directions as shown in Figure 2.13.[162] These directions correspond to a continuation of the beam in its original direction and a reflection of the beam by the plane on which the atoms of the crystalline powder lie on. Therefore, scattering by the atoms in the plane corresponds to the reflection by the plane. If the planes scatter in phase, the path difference must be an integer number of wavelengths, and the x-rays must scatter in accordance to the Bragg's law

$$n_w \lambda = 2 d_{hkl} \sin(\theta) \tag{2.17}$$

where n_w is the number of wavelengths, d_{hkl} is the distance between planes with Miller indices *hkl*, and θ is the scattering angle. The angles and intensities of the diffracted rays are recorded resulting in a peak pattern where the 2θ angle is plotted in the x-axis and the intensity in the y-axis. Verification of the crystalline material can be attained by comparison of the positions of the obtained peaks with standard patterns published in the literature.[18]

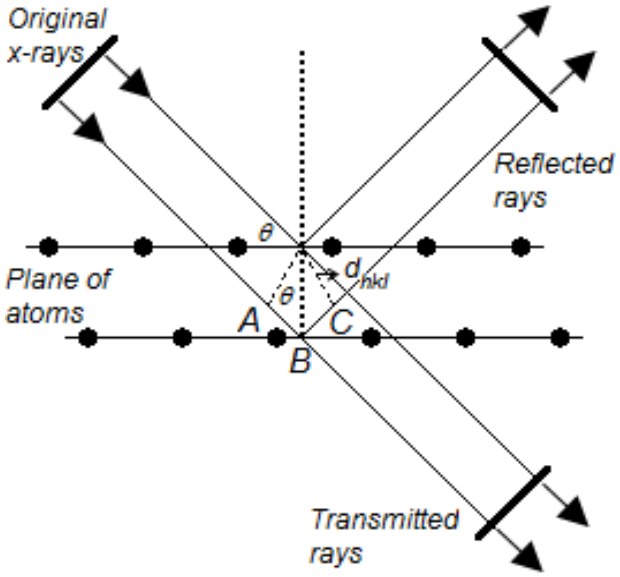

Figure 2.13 Geometry of Bragg reflections. The greater path difference between the two rays is ABC (or 2AB) which is equal to d_{hkl} sin θ.

2.4 Conductivity and pH

Conductivity and pH are crucial parameters for the control of the zeolite crystallization.[2,164] The composition and stability of the zeolite products as well as the solubility of the gel phase depend on the pH value. Conductivity measures the concentration of all ions present in a solution. Hence, the conductivity value is affected by the concentration of ions, their mobility, their binding, and the reactions among them. pH is a measure of the hydrogen (or hydroxide) ions. Therefore, it is a measure of the acidity or alkalinity of the sample. pH is strictly defined as a negative decimal logarithm of the hydrogen ion activity in a solution. However, pH is usually defined in terms of concentration of hydrogen ions as follows

$$pH = -\log\left[H^+\right] \tag{2.15}$$

where $[H^+]$ is the concentration of the hydrogen ions. The concentration of the hydroxide ions can be therefore calculated from the pH values as

$$\left[OH^-\right] = \frac{1\times10^{-14}}{10^{-pH}} \tag{2.16}$$

where $[OH^-]$ is the concentration of the hydroxide ions.

CHAPTER III

INVESTIGATION OF THE ORGANOCATION ROLE IN PRECURSOR MIXTURES OF SILICALITE-1*

3.1 Introduction

It was mentioned in Chapter I that the synthesis of silicalite-1 zeolite from optically transparent mixtures of TAA^+ (tetraalkylammonium cations), TEOS (tetraethyl orthosilicate), and water has been intensely studied with different experimental techniques and that these investigations have provided important information about the morphology of the precursor units,[50] as well as their evolution[50,59] and growth.[7,43] However, it was also mentioned that information related to the organocation-silica interactions in these synthesis mixtures is missing and that the objective of this work is to determine the strength of these interactions using PFG NMR spectroscopy. In this chapter, the investigation of the organocation-silica interactions in the first stages of the silicalite-1 formation using PFG NMR spectroscopy is presented.

The Dbppste (DOSY bipolar pulse pair stimulated echo) sequence is used here to determine the self-diffusion coefficients of the organocation in the mixtures. If a bipolar pulse pair stimulated echo sequence is used, the signal attenuation can be determined analogously to Eq. 2.13 as

---

*This chapter has been reprinted with permission from Rivas-Cardona, A.; Shantz, D. F., *The Journal of Physical Chemistry C* **2010**, 114 (47), 20178-20188.

$$\frac{I_g}{I_0} = \exp\left[-D\gamma^2 g^2 \delta^2 \left(\Delta - \frac{\delta}{3} - \frac{\tau}{2}\right)\right] \tag{3.1}$$

where I_g/I_0 is the attenuation of the signal, D is the translational self-diffusion coefficient, γ is the gyromagnetic ratio of the nucleus, g the gradient strength, δ the duration of the gradient pulse, Δ is the diffusion time, and τ is the gradient stabilization delay. In this case, the self-diffusion coefficient can be calculated from the slope of a plot of ln (I/I_0) versus $\gamma^2 g^2 \delta^2$ $(\Delta - \delta/3 - \tau/2)$.

3.1.1 The two-site model

An interesting problem results when the diffusion coefficients are affected by the contributions of the organocation in two (or more) different states. In other words, the organocations are either free in the mixture or bound to the silica nanoparticles as depicted in Figure 3.1. In this figure, site *f* is assigned to the organocations in the bulk mixture (or free organocations), while site *b* is assigned to the organocations adsorbed to the silica nanoparticles (or bound organocations).

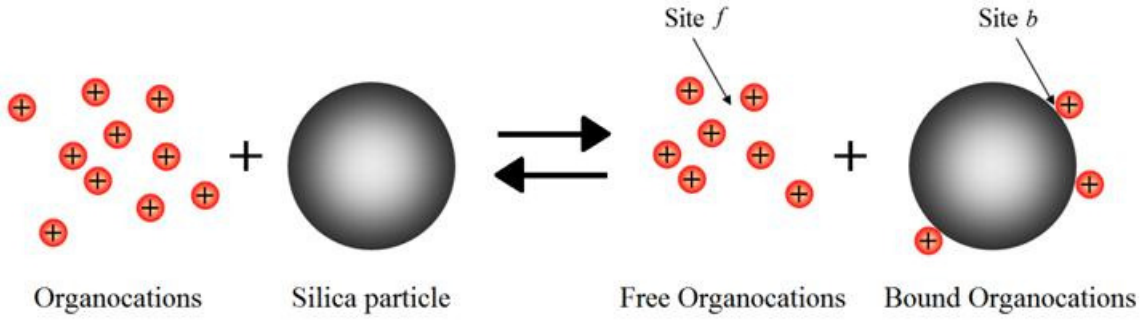

Figure 3.1 Two-site model for the organocation-silica nanoparticle mixtures.

The organocations can exchange between sites affecting the diffusion and relaxation processes. Schönhoff and Choudhury[133] proposed an equation for the general case of molecular exchange in heterogeneous systems where the probe molecules experience exchange between two sites. Their work unifies two theories: one concerning to the effect of exchange on diffusion experiments (developed by Kärger),[143,151] and the other concerning to the effect of the exchange on relaxation experiments (described by Woessner).[133] Thus, they describe the normalized echo intensity decay $I(x)$ of a spin exchanging between two different sites as a superposition of two exponential functions

$$I(x) = p_A \exp(-xa_A) + p_B \exp(-xa_B) \tag{3.2}$$

where a_A and a_B are the apparent decay constants, p_A and p_B are the apparent populations ($1 = p_A + p_B$), and x is the independent variable (e.g., time in the case of relaxation experiments or $\gamma^2 g^2 \delta^2 (\Delta - \delta/3 - \tau/2)$ in the case of diffusion). If the molecule experiences fast exchange between sites compared with the diffusion and relaxation time scale the intensity decay becomes monoexponential and the apparent decay constants of Eq. 3.2 can be described as a weighted average of the different states

$$r_m = x_f r_f + x_b r_b \tag{3.3}$$

where r_m is the mean decay constant (i.e., D_{obs} for diffusion); r_f and r_b are the decay constants for site f and b, respectively; and x_f and x_B are the true molecular fractions of the probe molecule in each site ($1 = x_f + x_b$). Based on Eqs 3.2 and 3.3, the observation of mono-exponential intensity decays in the diffusion and the relaxation experiments as well as the observation of diffusion coefficients that do not depend of the diffusion time

can be taken as an indicator that exchange is very fast relative to the diffusion and the relaxation scales.[139]

The investigation presented in this chapter shows that, following the approach of Figure 2.1, PFG NMR can be used to estimate the adsorption Gibbs energy of TPA mimics (i.e., organocations that resemble the TPA cation structure) that have previously proved to make silicalite-1.

3.2 Experimental

3.2.1 Materials

Figure 3.2 shows the three organocations investigated. Tetrapropylammonium hydroxide (TPAOH, Alfa Aesar, 40% w/w aq. soln.) was used as received. For the synthesis of MTPAOH and ETPAOH, tripropylamine (Aldrich, ≥ 98%), iodomethane (Sigma-Aldrich, 99%, reagent plus), iodoethane (Sigma-Aldrich, 99%, reagent plus), 2-butanone (EMD, 99%) and ethyl acetate anhydrous (EM Science, > 99.5%) were used as received. Anion exchange resin (J.T. Baker, IONAC NA-38, OH^- Form, Type I, Beads, 16-50 Mesh) was used for ion-exchange. Hydrochloric acid (EMD, 0.1N), phenolphthalein (VWR, indicator 1%, alcoholic) and a 0.04% w/v aqueous solution of m-cresol purple (Sigma-Aldrich, indicator grade) were used for titration. Tetraethyl orthosilicate (TEOS, Aldrich, ≥ 99.0% and Fluka, > 99.0%) and deuterium oxide (D_2O, CIL, 99.9%) were used in the silicalite-1 synthesis. Phosphate pH buffer (Beckman Coulter, pH 7.00 ± 0.01 at 25°C) and carbonate pH buffer (Beckman Coulter, pH 10.01 ± 0.01 at 25°C) were used for the calibration of the pH meter. Conductivity calibration

solution (VWR, 718 micro-Mho ± 1 at 25°C, 0.005 N KCl) was used to calibrate the conductivity meter.

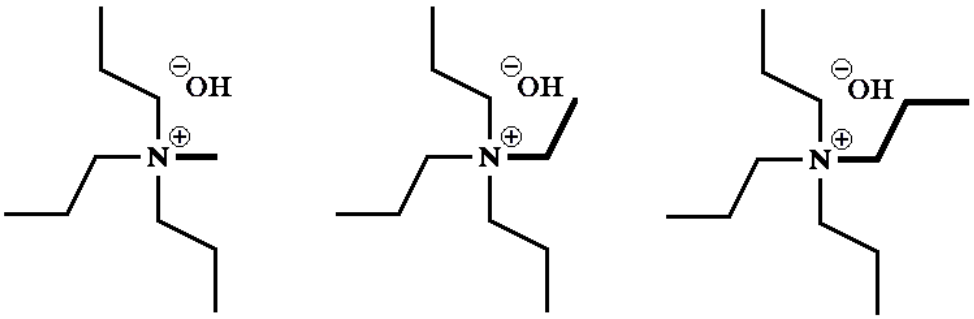

Methyltripropyl ammonium hydroxide (MTPAOH)

Ethyltripropyl ammonium hydroxide (ETPAOH)

Tetrapropyl ammonium hydroxide (TPAOH)

Figure 3.2 Molecular structure of the three organocations investigated.

3.2.2 Synthesis of structure directing agents (SDAs)

Methyltripropylammonium iodide (MTPAI) and ethyltripropylammonium iodide (ETPAI) were prepared by reacting iodomethane and iodoethane, respectively, with tripropylamine ($N(C_3H_7)_3$) by the following procedure: 60 mL (0.3 moles) of tripropylamine were added to 200 mL of butanone in a round-bottom flask. The corresponding iodoalkane (70 mL or 1.1 moles of iodomethane, and 75 mL or 0.9 moles of iodoethane) was placed in an additional funnel and then added drop wise to the tripropylamine mixture. The resulting solution was stirred under reflux for 24 hours in the absence of light. After this time, the reacting solution was cooled; the solids were recovered by filtration, rinsed with ethyl acetate and dried at room temperature. The typical yield was greater than 75% for MTPAI and greater than 90% for ETPAI. Each of these alkyltripropylammonium iodide salts was ion-exchanged twice to the hydroxide

form using a column with anion exchange resin. The resulting alkyltripropylammonium hydroxide ($RN(C_3H_7)_3^+OH^-$) solution was titrated with hydrochloric acid using m-cresol purple and phenolphthalein as indicators. The exchange efficiency was always greater than 80%, and usually greater than 90%.

3.2.3 Silicalite-1 synthesis: precursor mixtures

Mixtures of composition *x* $RN(C_3H_7)_3^+OH^-$: *y* TEOS: 7290 H_2O: 810 D_2O (where *x* = 1-18 moles, *y* = 0-60 moles, and R = Me, Et, and Pr) were prepared as follows. The organocation was first diluted with deionized water and deuterium oxide (added to provide a lock signal), and the resulting solution was then mixed with TEOS. The organocation-TEOS-water mixture was placed in a screw-cap Teflon container and was aged for 24 hours while mixing at room temperature to ensure full hydrolysis of TEOS.

3.2.4 Conductivity and pH

The conductivity measurements were performed at 25°C with an Amber Science (Model 2052) conductivity meter and Pt cell (Amber Science Inc., 545 Multi-Purpose Cell, 10.03 cm^{-1} cell constant). The conductivity meter was calibrated at 25°C using calibration solution. The accuracy of the conductivity meter at 25 ± 1°C was ± 0.002-0.3 mS. pH measurements were performed with a Beckman pH meter and glass electrode (Model 511052) at room temperature. The pH meter was calibrated with pH 7 and pH 10 buffer solutions at 25°C. The accuracy of the pH meter was ± 0.01.

3.2.5 Dynamic light scattering

DLS measurements were performed on a Brookhaven ZetaPALS instrument using a BI–9000AT correlator. A laser with a wavelength of 658 nm was used as

incident beam and the scattered light was detected at a 90° scattering angle. All the measurements were conducted at 25°C. The mixture was prepared by carefully filtering the solvent (DI water) through a 0.2 μm cellulose acetate filter to remove any dust particles that might affect the scattering measurements. In order to ensure repeatability, the measurements were performed three times on each sample with an elapsed time of 10 min. The light scattering data was analyzed with the BI–DLSW control software using the non–negative constrained least squares (NNLS) algorithm. This algorithm was used in this work for the analysis of the correlation functions in order to determine the size distributions.

3.2.6 NMR Spectroscopy

Single pulse ^{1}H, ^{1}H relaxation (spin-lattice and spin-spin) and ^{1}H diffusion NMR measurements were performed on a Varian INOVA spectrometer operating at 500 MHz for ^{1}H, equipped with a 5 mm indirect detection probe and a z-axis PFG coil that provides a maximum gradient strength of 30 G/cm. All the NMR experiments were carried out at 25°C, using 600 μL of sample and without spinning. Single pulse ^{1}H experiments were performed using 128 scans. The 90° pulse length was calibrated for each sample and the values were between 6.9 and 7.6 μs. The spin-lattice relaxation time, T_1, was determined from inversion recovery experiments. The spin-spin relaxation time, T_2, was measured using the CPMG pulse sequence. The diffusion coefficients were determined using the DOSY bipolar pulse pair stimulated echo (Dbppste) sequence shown in Figure 3.3. This stimulated echo sequence has a [*hsgt*-π-*hgst*] homospoil block at the beginning. The sequence uses pairs of bipolar gradient pulses of duration δ and

strength g followed by a gradient stabilization delay time τ. The first pair of gradient pulses spatially encodes the nuclear spins of the probe molecules; the spins are allowed to evolve during the diffusion delay time Δ after which the second pair of gradient pulses is applied to decode the nuclear spins. The gradient strength calibration was performed using a 10 mol% D_2O in H_2O mixture with a self-diffusion coefficient of $(2.26 \pm 0.01) \times 10^{-9}$ m^2/s.[165] The first delay d_1 was 2 s, τ was 500 μs, Δ was 50 ms unless mentioned otherwise, δ was 4 ms, and g was varied from 3 G/cm to 19 G/cm using 40 gradient levels that were acquired with 64 scans per level and 4 steady-state transients at the start of each level.

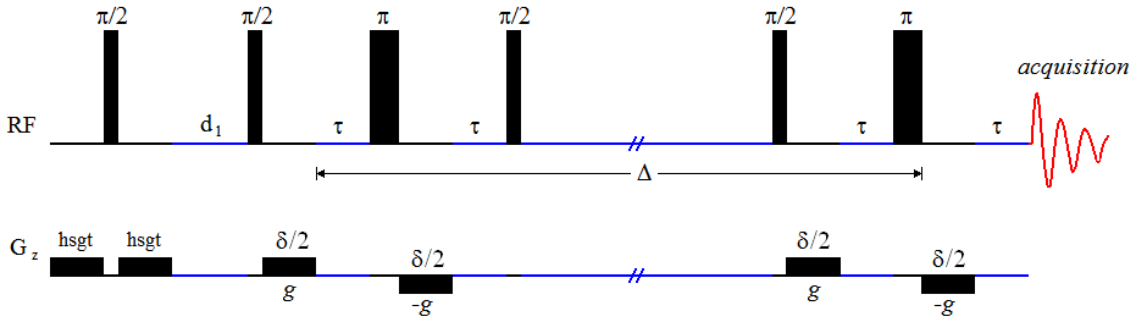

Figure 3.3 DOSY bipolar pulse pair stimulated echo (Dbppste) sequence.[166]

The NMR data was processed using Varian's VNMRJ 2.2C software.[167] In order to extract the diffusion data from the DOSY experiments, the baseline of all the spectra was corrected and the threshold was adjusted such all signals of interest were above it; the line broadening was set to 1 Hz and the FIDs were zero-filled; then, the *dosy* macro was used. This macro determines the heights of all signals above the threshold and fits the decay curve for each signal to a Gaussian. A 2D spectrum is constructed with this

information displaying the chemical shift in the first dimension and the diffusion coefficients in the second.

3.3 Results and Discussion

3.3.1 Conductivity and pH

Figure 3.4 shows the conductivity and the hydroxide concentration [OH^-] obtained from the pH values for MTPAOH-TEOS-water and ETPAOH-TEOS-water mixtures as a function of the total concentration of alkyltripropylammonium hydroxide. In general, the values of conductivity and hydroxide concentration are very similar for both organocations. This is expected as $MTPA^+$ and $ETPA^+$ are very similar in structure and have the same net charge. It can be noticed that with the addition of TEOS the conductivity and hydroxide concentration drop and that in mixtures containing TEOS the conductivity and hydroxide concentration increase slowly with the total concentration of alkyltripropylammonium hydroxide. These results are in agreement with previous results presented by Fedeyko[61] for the region above the critical aggregation concentration (cac) where uniform silica nanoparticles are observed in equilibrium with oligomeric species. The observed behavior is expected since in this work the amount of TEOS added to the mixtures with the lowest TEOS content (mixtures with y = 20 moles of TEOS = 0.13 mol/kg) is above the cac value (0.092 mol/kg) reported by Fedeyko[61] for a similar mixture with composition of 18 TPAOH: y TEOS: 9500 H_2O. Therefore, in the following discussion, silica refers to the presence of silica nanoparticles formed by incorporation of TEOS to the mixture.

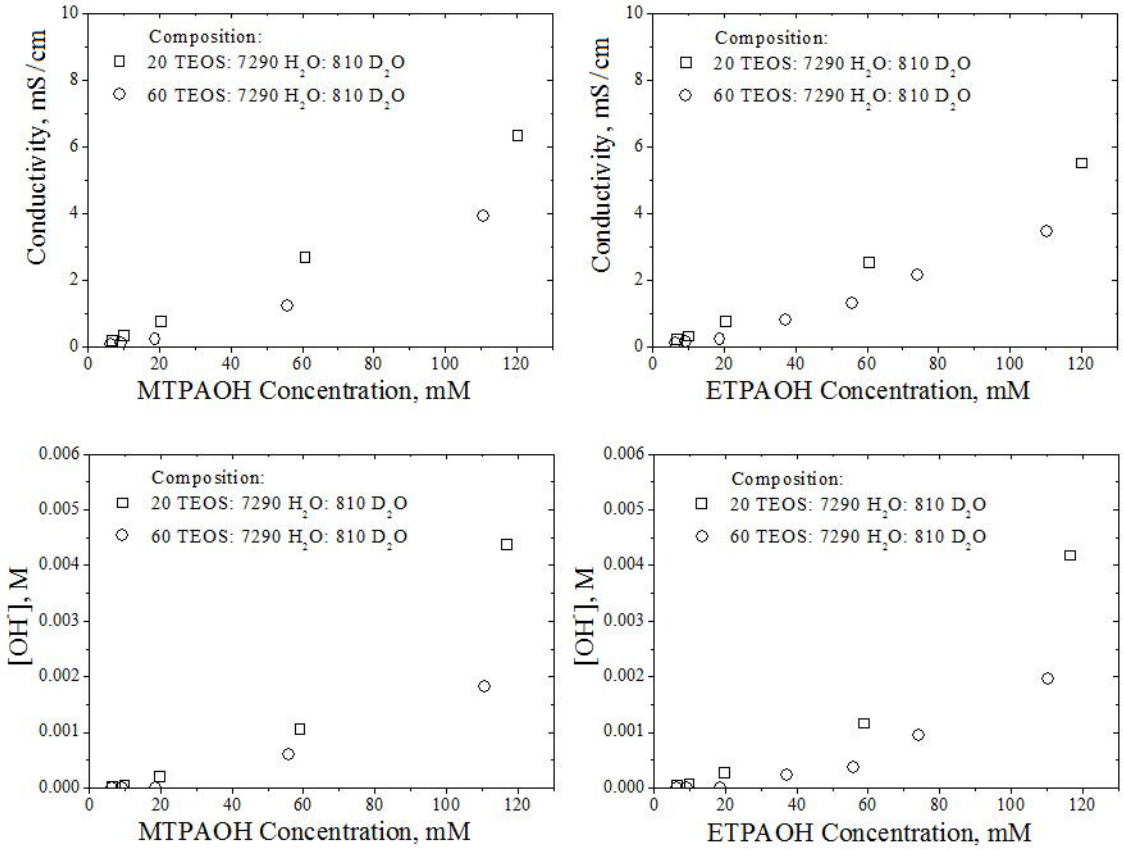

Figure 3.4 Conductivity and hydroxide concentration as a function of the total concentration of alkyltripropylammonium hydroxide.

3.3.2 NMR Spectroscopy and DLS

Figure 3.5 shows the one-pulse ^{1}H NMR spectra of MTPAOH-TEOS-water and ETPAOH-TEOS-water mixtures. In the absence of silica, the signal intensities of $MTPA^{+}$ (Figure 3.5a) increase monotonically as the MTPAOH concentration increases. In these mixtures, no changes in either the chemical shift or the line width are observed. However, in the presence of silica (Figure 3.5b and 3.5c), the $MTPA^{+}$ resonances show broadening and a considerable shift of some NMR resonances. These details are summarized in Table 3.1.

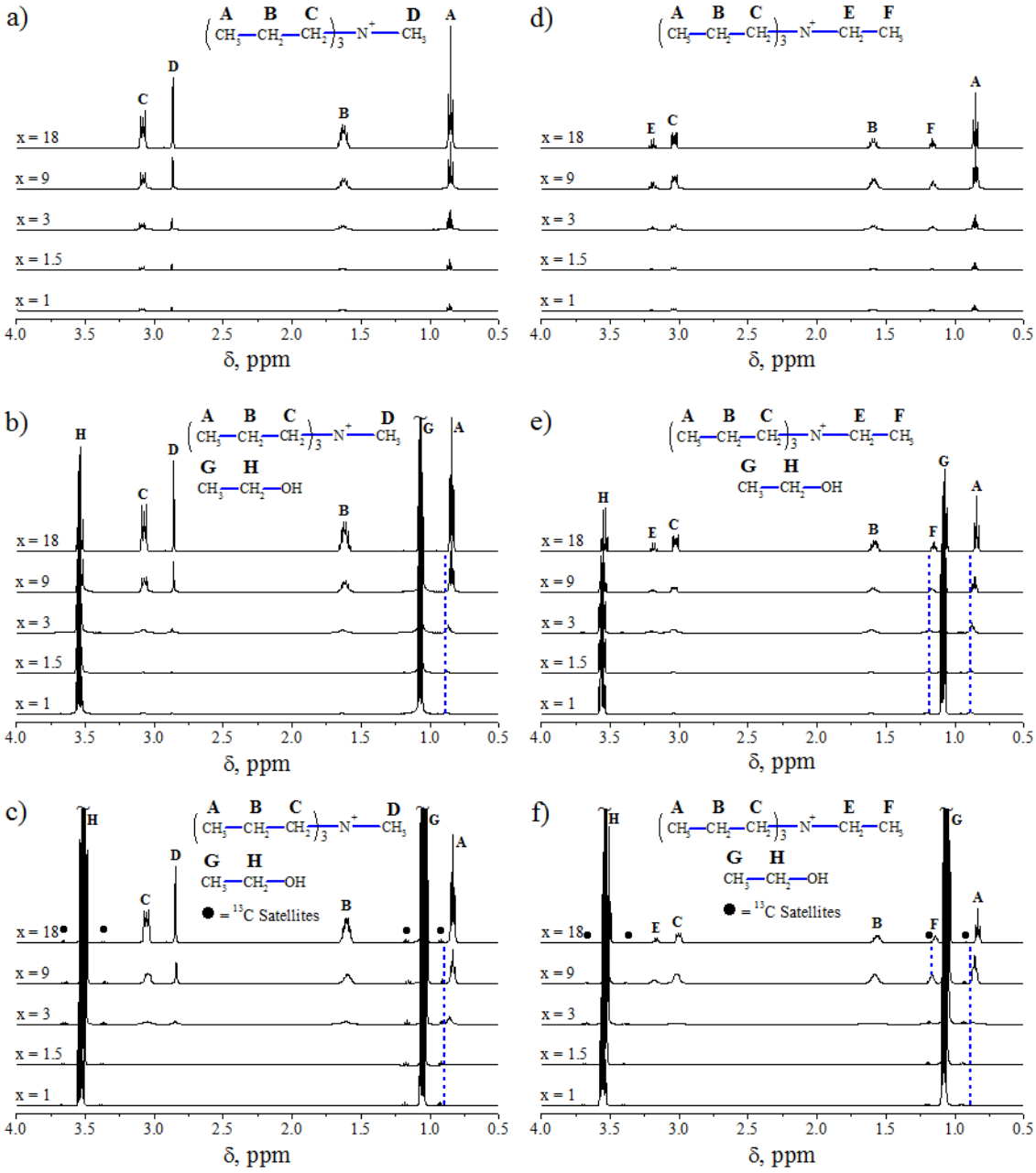

Figure 3.5 ^{1}H NMR spectra for mixtures with a molar composition of *x* MTPAOH: *y* TEOS: 7290 H_2O: 810 D_2O where a) *y* = 0, b) *y* = 20, and c) *y* = 60 and for mixtures with a molar composition of *x* ETPAOH: *y* TEOS: 7290 H_2O: 810 D_2O where d) *y* = 0, e) *y* = 20, and f) *y* = 60.

Table 3.1 Chemical shift changes of the organocation methyl resonances of Figure 3.5.

Composition	Shifted peaks	$\delta(x = 1)$, ppm	$\delta(x = 18)$, ppm	$\Delta\delta$, ppm ($\Delta\nu$, Hz)
x MTPAOH: 7290 H_2O: 810 D_2O	None			
x MTPAOH: 20TEOS: 7290 H_2O: 810 D_2O	A	0.87	0.84	0.03 (*15*)
x MTPAOH: 60 TEOS: 7290 H_2O: 810 D_2O	A	0.87	0.84	0.03 (*15*)
x ETPAOH: 7290 H_2O: 810 D_2O	None			
x ETPAOH: 20 TEOS: 7290 H_2O: 810 D_2O	A	0.88	0.84	0.04 (*20*)
	F	1.18	1.15	0.03 (*15*)
x ETPAOH: 60 TEOS: 7290 H_2O: 810 D_2O	A	0.88	0.84	0.04 (*20*)
	F	1.16[a]	1.14	0.02 (*10*)

[a] Chemical shift value at $x = 9$.

Figure 3.5b shows broad $MTPA^+$ lines at low organocation/silica ratios that become narrower as the organocation/silica ratio increases. Moreover, the triplet resonance corresponding to the methyl moiety (A) moves upfield as the organocation/silica ratio increases. The ethanol resonances (G and H) coming from the hydrolysis of TEOS do not show broadening or systematic changes in the chemical shift. Figure 3.5c shows that further addition of TEOS ($y = 60$) produces signal broadening in such a way that the observation of $MTPA^+$ peaks at low concentrations ($x \leq 1.5$) becomes difficult. This figure also shows an upfield shift of the methyl resonance (A) with increasing organocation/silica ratio.

A similar trend is observed in the mixtures with ETPAOH. In the absence of silica, the chemical shift and line width of the $ETPA^+$ signals (Figure 3.5d) do not

change with the ETPAOH concentration. However, the $ETPA^+$ signals show line broadening as the organocation/silica ratio decreases in mixtures that contain silica (Figure 3.5e). The organocation methyl resonances (A and F) shift upfield (Table 3.1) as the ETPAOH concentration increases. Further addition of silica (Figure 3.5f) shows stronger line broadening causing signal loss at $x \leq 3$. In this case, an upfield shift of both methyl resonances (A and F) is observed. The upfield shift of the methyl peak (A) of $ETPA^+$ is slightly and consistently greater than the upfield shift of the analogous methyl peak of $MTPA^+$. The change in chemical shift of the second methyl peak (F) from the lowest to the highest ETPAOH concentration cannot be determined due to low intensity and broadening of the signals.

Changes in line shape (i.e., broadening) and chemical shift can be attributed to organocation-silica interactions. Line broadening can be related to a reduction in the mobility of the organocations (or organocation segments) experiencing an association with the silica particles. Thus a possible cause for the observation of the signal attenuation is the decrease in organocation mobility. In contrast, upfield changes in chemical shift can be linked to a greater shielding likely due to weaker organocation-silica interactions and therefore, more mobile organocations. The organocation relaxation times (T_1 and T_2) are also important because they are an indicator of molecular motion and affect the diffusion NMR measurements. Therefore, the relationship between the relaxation times and the total concentration of alkyltripropylammonium hydroxide has been investigated.

Figure 3.6 shows the spin-lattice (T_1) and spin-spin relaxation (T_2) times of MTPAOH-TEOS-water and ETPAOH-TEOS-water mixtures for the methyl group D of the $MTPA^+$ and of the methyl group F of the $ETPA^+$, respectively. The error bars represent the error between the experimental data and the fitting to its respective relaxation function. Figure 3.6a shows that the spin-lattice relaxation time remains constant for MTPAOH-water mixtures but decreases with the addition of silica, particularly, at low MTPAOH concentrations. Figure 3.6b shows that the spin-spin relaxation time of $MTPA^+$ in water is practically independent of the MTPAOH concentration, but drops when TEOS is added to the mixtures. Furthermore, T_2 becomes dependent on the MTPAOH concentration in the presence of silica and its value drops as the MTPAOH decreases.

Similar trends are observed for ETPAOH-TEOS-water mixtures. The spin-lattice (Figure 3.6c) and spin-spin relaxation (Figure 3.6d) times are practically independent of the ETPAOH concentration for ETPAOH-water systems. However, the relaxation times decrease in the presence of silica; in particular, the spin-spin relaxation time decreases significantly. Relaxation times could not be determined at low concentrations of alkyltripropylammonium hydroxide (either MTPAOH or ETPAOH) and high concentrations of TEOS because of the low intensity and broadening of the signals. This can be particularly observed in Figure 3.6d, where the spin-spin relaxation time can only be determined at high ETPAOH concentrations. This behavior is consistent with the previous discussion that, at low concentrations of alkyltripropylammonium hydroxide and high concentrations of TEOS, the organocation-silica interactions cause a reduction

in the mobility of the organocations and, therefore, line broadening that in this figure is associated with short T_2 times. On the other hand, the fact that T_2 is shorter than T_1 can be attributed to chemical exchange, which can occur in mixtures with relatively low viscosity as the ones investigated here (i.e., with viscosity similar to that of the water). PFG NMR has been used to further quantify the organocation mobility.

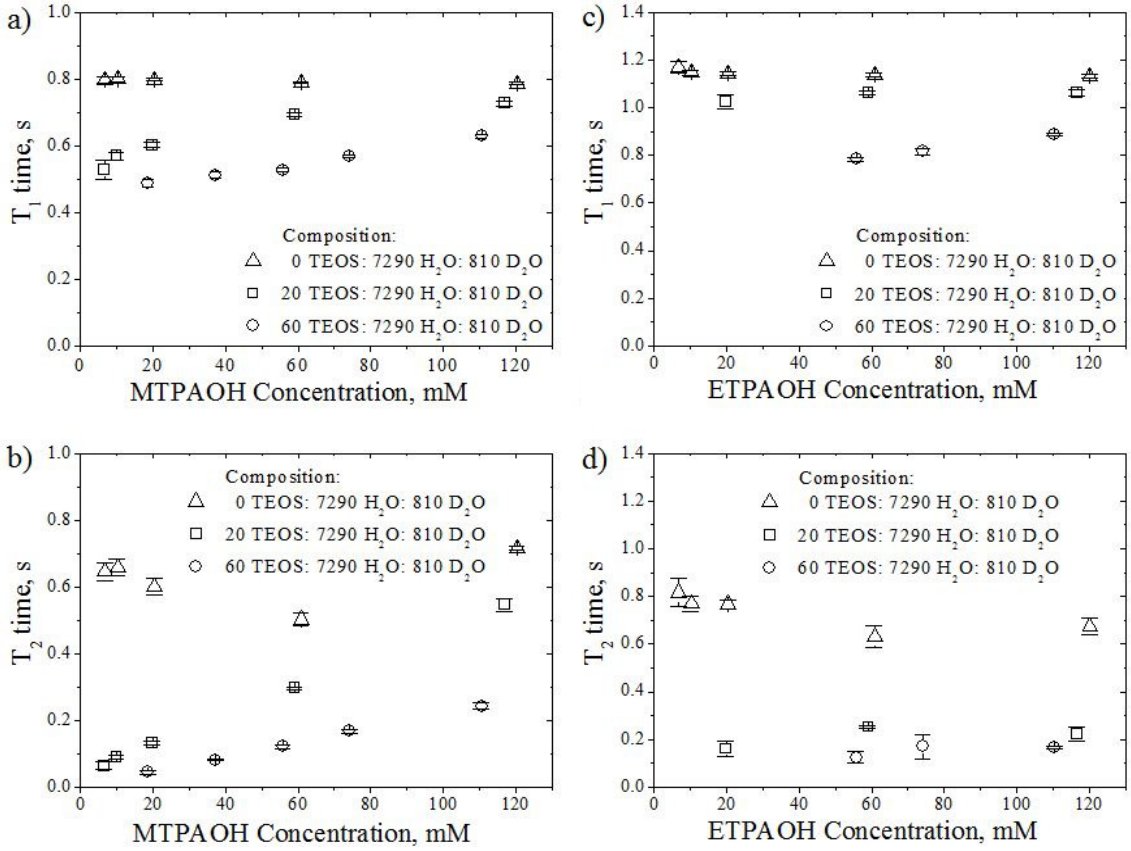

Figure 3.6 Relaxation times as a function of the total concentration of alkyltripropylammonium hydroxide. a) Spin-lattice relaxation (T_1) time for mixtures with a molar composition of *x* MTPAOH: *y* TEOS: 7290 H_2O: 810 D_2O. b) Spin-spin relaxation (T_2) time for mixtures with a molar composition of *x* MTPAOH: *y* TEOS: 7290 H_2O: 810 D_2O. c) Spin-lattice relaxation (T_1) time for mixtures with a molar composition of *x* ETPAOH: *y* TEOS: 7290 H_2O: 810 D_2O. d) Spin-spin relaxation (T_2) time for mixtures with a molar composition of *x* ETPAOH: *y* TEOS: 7290 H_2O: 810 D_2O.

Figure 3.7 shows the diffusion NMR results for a series of MTPAOH-TEOS-water, ETPAOH-TEOS-water and TPAOH-TEOS-water mixtures. The error bars represent the line width of the signal in the diffusion dimension determined by the estimated error of the diffusion coefficient obtained from the fitting process.[168] In the absence of silica the diffusion coefficients of the organocations appear insensitive to alkyltripropylammonium hydroxide concentration and the values are shown in Table 3.2. The self-diffusion coefficients presented in this table have been calculated as the average of the coefficients of all data points showed in Figure 3.7 for organocation-water mixtures and the error represents its standard deviation. By contrast the addition of TEOS leads to a decrease in the observed organocation diffusion coefficients. The lowest values of diffusion coefficients are detected at the highest TEOS content and were $(0.254 \pm 0.027) \times 10^{-9}$ m^2/s at 18.7 mM of MTPAOH, $(0.262 \pm 0.072) \times 10^{-9}$ m^2/s at 18.7 mM of ETPAOH, and $(0.276 \pm 0.042) \times 10^{-9}$ m^2/s at 18.7 mM of TPAOH. Diffusion coefficients cannot be determined at lower alkyltripropylammonium hydroxide concentrations because of the low signal intensity as discussed above. Also, noteworthy is that at the highest organocation contents the diffusion coefficient approaches the value of the organocation in aqueous solution (i.e., in the absence of TEOS) as shown in Table 3.2. One simple way to explain the results in Figure 3.7 is that in the presence of silica particles (formed after the TEOS hydrolysis) the organocation experiences two distinct states, a free state and a bound state. Therefore, the organocation reduces its mobility, which is manifested as a decrease in the diffusion coefficient.

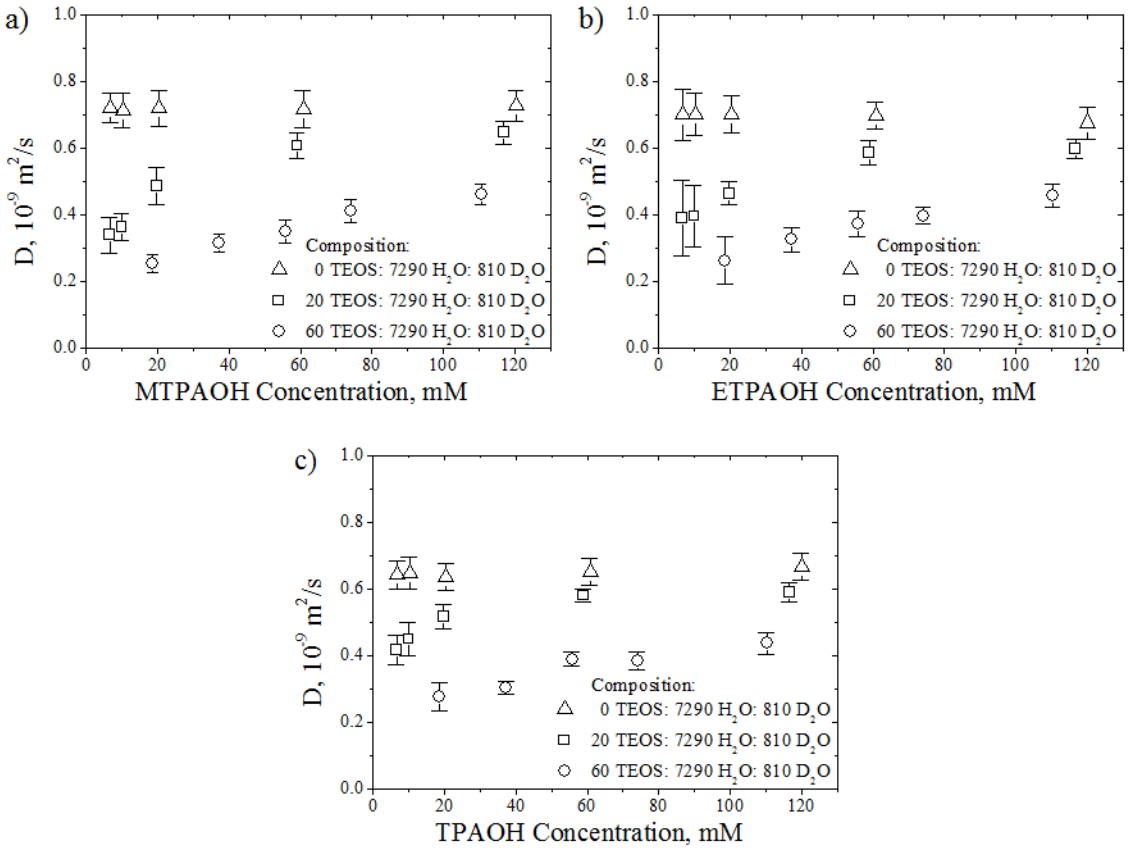

Figure 3.7 Diffusion coefficients as a function of the total concentration of alkyltripropylammonium hydroxide for mixtures with a molar composition of a) *x* MTPAOH: *y* TEOS: 7290 H_2O: 810 D_2O, b) *x* ETPAOH: *y* TEOS: 7290 H_2O: 810 D_2O, and c) *x* TPAOH: *y* TEOS: 7290 H_2O: 810 D_2O.

Table 3.2 Self-diffusion coefficients of the organocations in water at 25°C.

Organocation	D_f, 10^{-9} m^2/s
$MTPA^+$ (Methyltripropylammonium)	0.719 ± 0.006
$ETPA^+$ (Ethyltripropylammonium)	0.694 ± 0.011
TPA^+ (Tetrapropylammonium)	0.648 ± 0.011[a]

[a] The diffusion coefficient of TPA^+ in dilute aqueous solution at 25°C reported in the literature is 0.623 × 10^{-9} m^2/s.[169]

The relaxation and diffusion data presented above indicates that the silica perturbs the mobility of the organocation, since the relaxation times and the diffusion coefficients show significant changes as compared to the values of the organocation in water. A simple way to model the organocation-silica interactions is using the two-site model previously shown in Figure 3.1 which considers that the organocation can exists free in the aqueous mixture or bound to the silica nanoparticles. As described in the introduction section, the decay constants in Eq. 3.2 for molecules exchanging between both sites can be simplified in the fast exchange limit (Eq. 3.3). In this limit the exchange is fast compared to the relaxation and diffusion scale. One way to ascertain if the organocation exchanges in the fast limit is by observing the signal decays of the relaxation and diffusion experiments. If monoexponential decay of the signals in the relaxation and diffusion experiments is observed and the observed diffusion coefficient (D_{obs}) is independent of the diffusion time (Δ) then exchange (τ_{ex}) is very fast compared with the relaxation and diffusion scales.[139]

The relaxation data showed in Figure 3.6 is well described by monoexponential decays. In Figure 3.8 the signal decays from the diffusion experiments as a function of the diffusion time (Δ) are shown. Figure 3.8a shows the signal decays for a mixture with composition 3 MTPAOH: 20 TEOS: 7290 H_2O: 810 D_2O, while Figure 3.8b shows the signal decays for a mixture of ETPAOH with an analogous composition (3 ETPAOH: 20 TEOS: 7290 H_2O: 810 D_2O). In this figure it can be observed that the signal decays monoexponentially. In addition, the slope of the normalized intensity does not change

with the diffusion time and therefore, the diffusion coefficient (which can be calculated from the slope) is independent of the diffusion time.

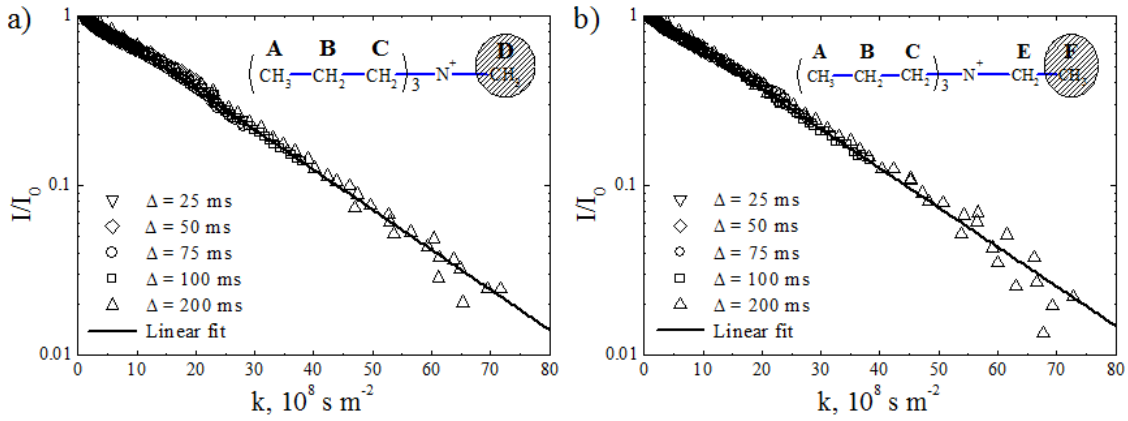

Figure 3.8 Signal decays obtained from the diffusion experiments as a function of the diffusion time for a mixture with a molar composition of a) 3 MTPAOH: 20 TEOS: 7290 H_2O: 810 D_2O and b) 3 ETPAOH: 20 TEOS: 7290 H_2O: 810 D_2O. The decays correspond to the methyl signal highlighted in the molecular structure of the organocation.

Based on the results in Figure 3.8 it can be concluded that the systems are in the fast exchange limit. Thus, the observed diffusion coefficient (D_{obs}) is given by a weighted average between the free and the bound state

$$D_{obs} = x_f D_f + x_b D_b \tag{3.4}$$

where *f* denotes the free state and *b* denotes the bound state. The diffusion coefficient for the former (D_f) is taken as the self-diffusion coefficient of the organocation determined from organocation-water mixtures and these values are summarized in Table 2. The diffusion coefficient for the latter (D_b) is taken as the diffusion coefficient of the silica particle and can be estimated from dynamic light scattering, where the bound diffusion

coefficient (D_b) is obtained from the particle size using the Stokes-Einstein equation (Eq. 2.14)

$$D_b = \frac{k_B T}{3\pi\eta d_H} \tag{3.5}$$

where k_B is the Boltzmann's constant, T is the absolute temperature, η is the viscosity of the medium and d_H is the hydrodynamic diameter. DLS analysis of the mixtures yields several observations. First, in all mixtures there is a bimodal distribution of small (5 nm or less) particles and large (100 nm or larger) particles. The relative number of small particles increases with increasing OH content (i.e., increasing organocation content). These values have been obtained with NNLS size distributions for mixtures of composition of 3 $RN(C_3H_7)_3^+OH^-$: 60 TEOS: 7290 H_2O: 810 D_2O.[170] It is important to point out that NNLS distributions are weighted by the intensity not the particle number density. Given that the scattering intensity scales non-linearly with particle size the number of large particles is overestimated. Although this can potentially complicate the analysis of the PFG NMR data, a few important points can be made. First, it is unlikely that the organocations bound to the large aggregates contribute to the diffusion NMR spectra. This is due to the fact that their rotational diffusion rate will be slow on the NMR time scale. Second, the influence of the errors of the input parameters (D_{obs}, D_f and D_b) on the bound fraction of organocation (x_b) calculated with Eq. 3.4 has been analyzed by varying the input parameters within their error and the analysis has shown that the bound fraction is considerably sensitive to the errors of D_{obs} and D_f, but not very sensitive to the error of D_b. Based on these two observations it seems unlikely that the

organocations bound to the large aggregates contribute significantly to the diffusion NMR results.

3.3.3 Adsorption isotherms and Gibbs energy

With the previous information it is possible to calculate the fractions of free and bound organocation, and determine the amount of organocation bound (Γ) as a function of the total concentration of alkyltripropylammonium hydroxide. This information is presented in Figure 3.9. The plots show the amount of bound organocation bound for two cases, the first being if all the nanoparticles are 5 nm in size (filled symbols), the second being if the nanoparticles are all 200 nm in size (open symbols). Interestingly it can be observes that the fraction of organocation bound is very similar for both scenarios. A fairly linear increase in the amount of bound organocation at low organocation content is observed. Then, the convergence towards a plateau at high concentrations of alkyltripropylammonium hydroxide is observed, and it is likely due to the saturation of the silica nanoparticle surface. It can also be noticed that the calculated amount of the organocation bound to 5 nm silica particles is very similar (a difference less than 15%) to that of the organocation bound to 200 nm silica aggregates.

From the data in Figure 3.9 it is possible to determine both the binding energies and organocation concentration on the particle surface at saturation. One of the many ways to analyze the data is through the use of the Lineweaver-Burk linearization of the Langmuir isotherm

$$\frac{1}{\Gamma} = \frac{1}{\Gamma_{max}} + \frac{1}{\Gamma_{max} K_{ad} C} \tag{3.6}$$

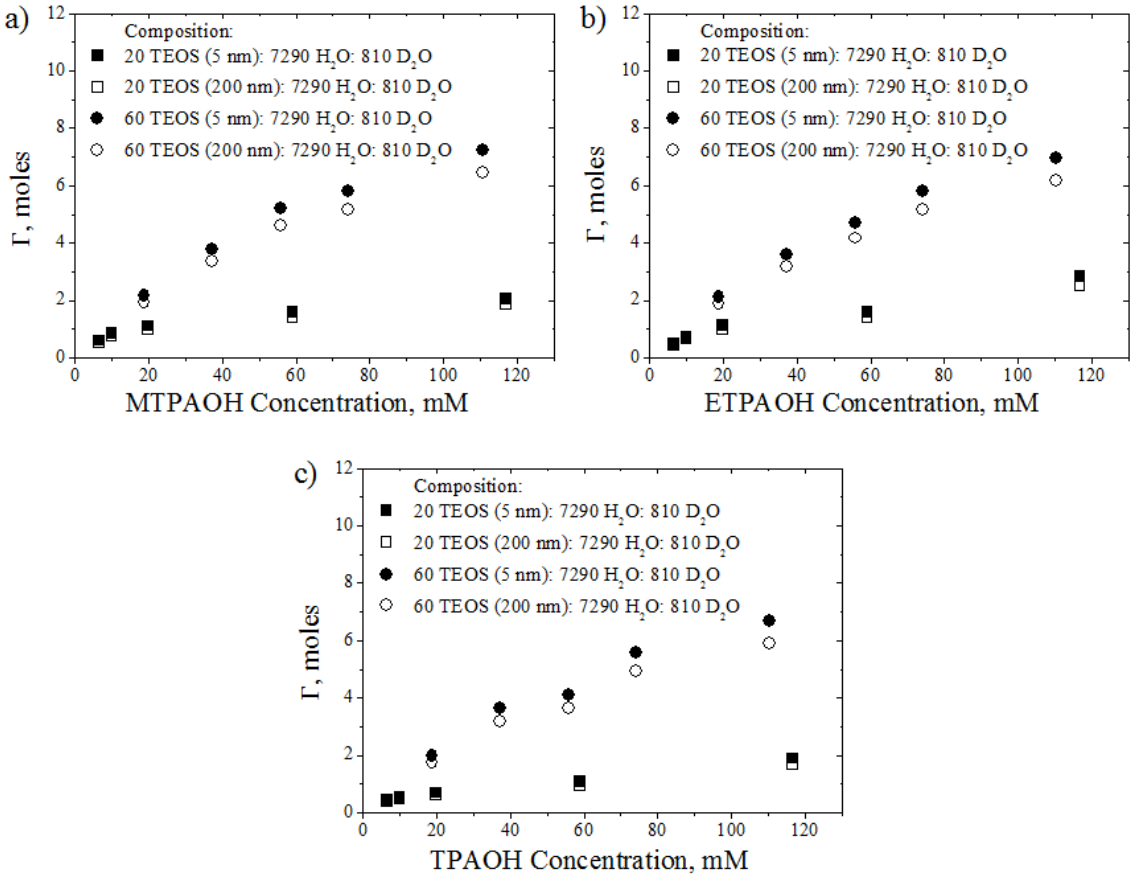

Figure 3.9 Amount of bound organocation as a function of the total concentration of alkyltripropylammonium hydroxide for mixtures with a molar composition of a) *x* MTPAOH: *y* TEOS: 7290 H_2O: 810 D_2O, b) *x* ETPAOH: *y* TEOS: 7290 H_2O: 810 D_2O, and c) *x* TPAOH: *y* TEOS: 7290 H_2O: 810 D_2O. Open symbols correspond to the analysis where all particles are considered to have 200 nm in diameter; filled symbols correspond to the analysis where all particles are considered to have 5 nm in diameter.

where Γ is the amount of bound organocation, Γ_{max} is the maximum amount of bound organocation, K_{ad} is the adsorption constant and C is the equilibrium concentration of the organocation in the mixture. The Lineweaver-Burk fits of the isotherms are shown in Figure 3.10. These plots show the inverse of the amount of organocation absorbed to 5 nm particles as a function of the inverse of the equilibrium concentration.

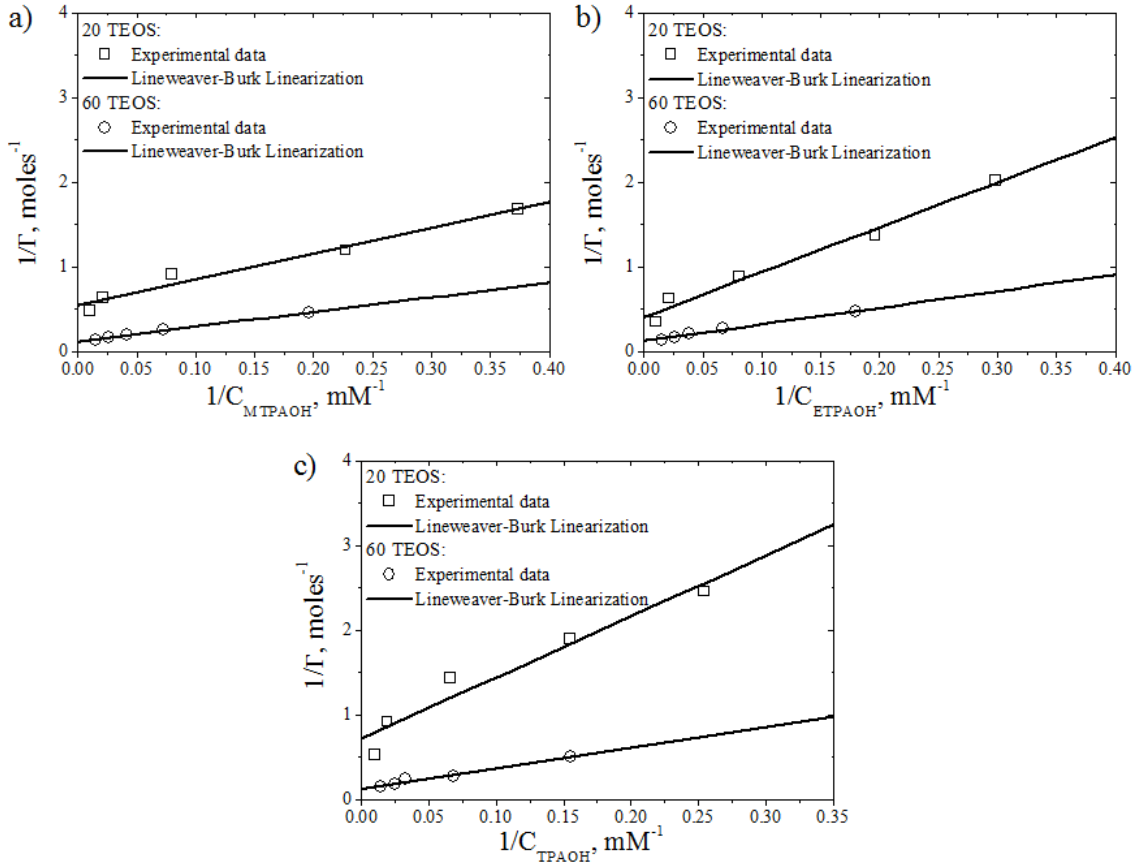

Figure 3.10 Lineweaver-Burk plots and fits for a) *x* MTPAOH: *y* TEOS: 7290 H_2O: 810 D_2O, b) *x* ETPAOH: *y* TEOS: 7290 H_2O: 810 D_2O, and c) *x* TPAOH: *y* TEOS: 7290 H_2O: 810 D_2O mixtures.

The adsorption constant (K_{ad}) and the maximum amount of bound organocation (Γ_{max}) are obtained from the Lineweaver-Burk fit. The change in the adsorption Gibbs energy (ΔG_{ad}) is calculated as

$$\Delta G_{ad} = RT\ln\left(K_{ad}\right) \tag{3.7}$$

where R is the gas constant. The adsorption constant, the maximum amount of bound organocation, and the adsorption Gibbs energy are summarized in Table 3.3.

Table 3.3 Langmuir constants and adsorption energy for mixtures with a molar composition of *x* $RN(C_3H_7)_3^+OH^-$: *y* TEOS: 7290 H_2O: 810 D_2O.

Organocation	K_{ad}, L/mol	Γ_{max}, moles	Γ^*_{max},[a] moles	R^2	σ[a]	ΔG_{ad}, kJ/mol
$MTPA^+$						
y = 20	182.9	1.81	0.155	0.972	0.091	-12.91
y = 60	70.5	8.15	0.158	0.994	0.011	-10.55
$ETPA^+$						
y = 20	78.1	2.42	0.206	0.980	0.105	-10.80
y = 60	65.9	7.77	0.150	0.990	0.015	-10.38
TPA^+						
y = 20	101.1	1.38	0.118	0.939	0.219	-11.44
y = 60	51.4	7.94	0.154	0.978	0.025	-9.77

[a] Maximum amount of adsorbed organocations (Γ_{max}) per amount of silica nanoparticles. The amount of silica nanoparticles has been calculated with the value of $[SiO_2]_{cac}$ = 0.052 mol/kg (or y_{cac} = 8.31 mol) reported by Fedeyko[61] for a sample with composition of 9 TPAOH: *y* TEOS: 9500 H_2O.

[b] Residual standard deviation defined as $\sigma = (Q/n_{obs} - p)^{1/2}$, where Q is the objective function, n_{obs} is the number of observations, and p is the number of parameters in the model.

In Table 3.3 it can be observed that the adsorption constant decreases as the amount of TEOS increases in the mixtures. In general, for a given TEOS concentration the adsorption constants of $MTPA^+$ are larger than the adsorption constants of $ETPA^+$ which are larger than those of TPA^+. The exception to this is the mixture with *x* TPA: 20 TEOS: 7290 H_2O: 810 D_2O which also has the lowest determination coefficient (R^2) and the highest residual standard deviation (σ). In general, the determination coefficient and

the residual standard deviation show that the experimental data fit well to the Langmuir isotherm. However, deviations of the model might occur because the Lineweaver-Burk linear regression, which is the double reciprocal of the Langmuir equation, might be susceptible to data errors at low concentrations. This is likely due to the fact that the Langmuir model assumes that all adsorption sites are uniform. Particularly at low organocation concentrations this might not be the case as it would be anticipated that organocations bind at the most favorable binding sites first. The MTPA organocation displays larger values of the adsorption constant and Gibbs energy compared with the values of ETPA and TPA organocations for analogous concentrations of TEOS. Therefore, the strongest organocation-silica binding strength is associated to the MTPA organocation. One simple explanation for this result is this molecule has the small C/N ratio, and thus is the most hydrophilic and also has the highest charge density.

The values presented in Table 3.4 are used to calculate the number of organocations adsorbed per silica particle, which has been assumed to have a core containing 356 silicon atoms as reported by Vlachos.[171] Most of the numbers trend to the same value range of approximately 55 organocations per particle. However, many assumptions have been made for this calculation (e.g., uniformity of surface coverage) and may not be precisely correct. The number of organocations per particle in the TPA mixture with the lower TEOS content appears much lower; as mentioned above, the fitting results appear to be the least statistically robust. The ETPA mixture with the low TEOS content appears to give a much higher value. The origin of this is unclear currently. One reasonable conclusion from Table 3.4 is that the organocation monolayer

coverage of silica nanoparticles seems to be fairly independent of organocation identity and silica content. The former makes sense as the size of the three organocations is very comparable. The latter is consistent with the existing model that above the cac addition of silica leads mainly to more particles instead of a dramatic change in the particle size. It is also important to mention that these numbers are different from those reported previously for TPA-silica mixtures,[172] where the nanoparticles were formed using NaOH followed by addition of TPABr into the mixture. This preparation method resulted in very low dilution of the TPA and the presence of an excess of sodium organocations. In this investigation the nanoparticle formation has been controlled by the addition of organocation and no sodium has been incorporated to the mixtures.

Table 3.4 Organocation monolayer coverage of silica nanoparticles in mixtures with a molar composition of *x* $RN(C_3H_7)_3^+OH^-$: *y* TEOS: 7290 H_2O: 810 D_2O.

Organocation	No. of organocations/particle
$MTPA^+$	
y = 20	55
y = 60	56
$ETPA^+$	
y = 20	74
y = 60	54
TPA^+	
y = 20	42
y = 60	55

3.4 Conclusions

Diffusion NMR results of mixtures containing TPA mimics (i.e., organocations that resemble the TPA cation structure) and silica are reported in this chapter. The diffusion NMR results indicate that the organocation adsorption free energies are quite comparable to TPA for the two TPA mimics investigated. This finding is quite interesting, as previous work has shown that these same TPA mimics lead to dramatically different (and slower) rates of silicalite-1 growth as compared to TPA.[44] In particular, MTPA cations were shown to lead to growth rates 50% slower than those of TPA. Thus, the current investigation shows that small changes in the binding energy to the silica nanoparticles will lead to large changes in the stability of these precursor particles and rate of zeolite formation. This investigation shows that PFG is uniquely suited to determine the silicate-organocation interactions in a non-invasive way. How these findings translate to in situ studies of zeolite formation will be reported in the next chapter.

CHAPTER IV

IN SITU PFG NMR INVESTIGATION OF SILICALITE-1 SYNTHESIS MIXTURES*

4.1 Introduction

It was shown in Chapter III that the strength of the organocation-silica interactions in precursor mixtures can be determined at room temperature from diffusion data obtained with PFG NMR spectroscopy. Although the results of this first investigation are important, information about the strength of the organocation-silica interactions under conditions approaching those of the actual synthesis mixtures (i.e., elevated temperatures) is necessary for a better understanding of zeolite nucleation and growth. Obtaining this information from diffusion experiments is not trivial because other effects such as convection can arise while increasing the temperature. Even though, NMR spectroscopy provides a suitable sequence for the determination of the diffusion coefficients if convection is present due to the relatively high temperatures. Thus, the next step of this research project has been the determination of the strength of organocation-silica interactions in TPAOH-TEOS-water mixtures at relatively high temperatures. Both in situ NMR and DLS have been used to investigate the TPA-silicalite-1 synthesis at 70°C. The term in situ refers to the NMR or DLS measurements performed at the synthesis conditions (i.e., temperature and concentration of the

---

synthesis). To the best knowledge of the author, there are no reports in the literature that use in situ PFG NMR for the investigation of zeolite synthesis mixtures.

In the investigation presented in this chapter, DOSY has been also used to determine the self-diffusion coefficients of the TPA cation. The diffusion NMR results have been analyzed using a two-site model, which was described in Chapter III. Fast exchange of the organocation between a free and bound state has been assumed in this investigation given that in Chapter III was shown that the TPAOH-TEOS-water systems at 25°C are in the fast exchange limit. Therefore, it is expected that increasing the temperature to 70°C leads to an increase in the exchange rate between sites. Therefore, the observed diffusion coefficient (D_{obs}) at 70°C can be also described with the Eq. 3.4 as a weighted average of the organocation exchanging between two states

$$D_{obs} = x_f D_f + x_b D_b \tag{3.4}$$

Thus, the investigation presented in this chapter shows that the organocation-silica interaction strength in TPA-synthesis mixtures at relatively higher temperatures can be determined in situ using PFG NMR. This information provides useful insights into the formation of silicalite-1.

4.2 Experimental

4.2.1 Materials

Tetrapropylammonium hydroxide (TPAOH, Alfa Aesar, 40% w/w aq. soln.), tetraethyl orthosilicate (TEOS, Aldrich, ≥ 99.0% and Fluka, > 99.0%), and deuterium oxide (D_2O, CIL, 99.9%) were used as received. Ethylene glycol (CIL, 80% in 20% DMSO–D6) was used for the temperature calibration of the NMR spectrometer.

Phosphate pH buffer (Beckman Coulter, pH 7.00 ± 0.01 at 25°C) and carbonate pH buffer (Beckman Coulter, pH 10.01 ± 0.01 at 25°C) were used for the calibration of the pH meter. Conductivity calibration solution (VWR, 718 micro–Mho ± 1 at 25°C, 0.005 N KCl) was used to calibrate the conductivity meter.

4.2.2 Silicalite-1 synthesis

Precursor mixtures with molar composition of *x* TPAOH: *y* TEOS: 7290 H_2O: 810 D_2O (where *x* was varied from 1 to 18 and *y* was varied from 0 to 60) were prepared following the procedure described in Chapter III. The precursor mixtures were heated at 70°C for varying periods of time.

4.2.3 In situ NMR spectroscopy

Single pulse ^1H and ^1H diffusion NMR measurements were performed on a Varian INOVA spectrometer operating at 500 MHz for ^1H, equipped with either a 5 mm indirect detection probe (with a z-axis PFG coil that provides a maximum gradient strength of 30 G/cm) or an H/F/C/P quadruple resonance probe (with a z-axis PFG coil that provides a maximum gradient strength of 65 G/cm). The temperature was regulated with a VT controller at a flow rate of 10-15 L/min. All the NMR experiments were carried out using 600 μL of sample with a vortex plug on the top of the column of liquid and without spinning to avoid convection. Samples within the probe were allowed to equilibrate at the desired temperature for at least 15 minutes. The gradient strength calibration was performed using a 10 mol% D_2O in H_2O mixture at 25°C with a self-diffusion coefficient of $(2.26 \pm 0.01) \times 10^{-9}$ m^2/s.[169] The temperature calibration was performed with a mixture of 80% ethylene glycol in 20% DMSO-D6. Single pulse ^1H

experiments were performed using 128 scans. The 90° pulse length was calibrated for each mixture; the values were between 6.9 and 7.0 μs at 25°C and 10.2 and 13.25 μs at 70°C when using the indirect probe, and between 23.5 and 29.0 μs at 70°C when using the quadruple resonance probe. In order to measure the diffusion coefficients at 70°C, convection compensated DOSY experiments were carried out using the DOSY bipolar pulse pair stimulated echo with convection compensation (Dbppste_cc) sequence shown in Figure 4.1. The Dbppste_cc sequence is a modification of the Dbppste sequence described in Chapter III and includes an additional block of pulses (dashed red box in Figure 4.1) exactly halfway through the diffusion delay.[168] A $\pi/2$ (90°) pulse is used in this block to move the magnetization back to the transverse plane. The magnetization gets refocused by the first gradient pulse δ_1 (green). The second gradient pulse, identical in sign, duration, and length to the first one, phase labels the spins in the opposite direction. Since the Dbppste sequence uses pairs of bipolar gradient pulses of duration δ_1 and strength g, a second pair of δ_1 pulses with an opposite direction to the first pair is applied. Then, the magnetization is moved back again to the axial plane for the second half of the diffusion delay. Because of the ordered nature of convection, the phase evolution due to this phenomenon is opposite during the two halves of the diffusion delay. Therefore, the convection contributions compensate each other, while diffusion being a random process is not affected. Homospoil gradient pulses (shown in red) are used in both halves of the diffusion delay in order to only detect desired coherences. The need for convection compensation was determined by moving the convection compensation block systematically along the diffusion delay (Δ) through an auxiliary

diffusion delay parameter (Δ_{aux}). In the presence of convection, signal attenuation and/or phase distortion were observed when the convection compensation block was shifted.[173] In the Dbppste_cc sequence, the first delay d_1 was 2 s, the gradient stabilization delay time τ was 500 μs, the diffusion delay Δ was 50 ms, the duration of the gradient pulse δ_1 was 2 ms (δ_2 and δ_3 were 3 ms), and the strength of the gradient pulse g was varied from 4 G/cm to 27 G/cm using 40 gradient levels that were acquired with 64 scans (or 128 scans when the quadruple resonance probe was used) per level and 4 steady–state transients at the start of each level.

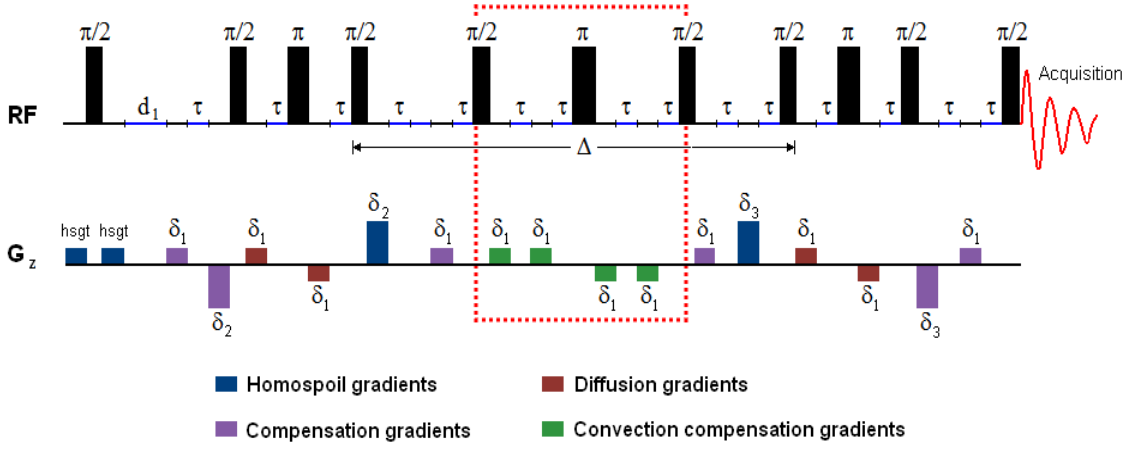

Figure 4.1 DOSY bipolar pulse pair stimulated echo with convection compensation (Dbppste_cc) sequence.[168]

The NMR data was processed using Varian's VNMRJ 2.2D software.[168] In order to extract the diffusion data from the DOSY experiments, the baseline of all the spectra was corrected and the threshold was adjusted such all signals of interest were above it; the line broadening was set to 1 Hz and the FIDs were zero-filled; then, the *dosy* macro was used. This macro determines the heights of all signals above the threshold and fits

the decay curve for each signal to a Gaussian. A 2D spectrum is constructed with this information displaying the chemical shift in the first dimension and the diffusion coefficients in the second.

4.2.4 Dynamic light scattering

DLS measurements were performed on the instrument described in Section 3.2.5. However, in this investigation all the measurements were conducted at 70°C. Therefore, properly cleaned semi–micro PMMA cuvettes (VWR 97000-590, volume range between 1.5 to 3 ml) were used at their minimum fill volume to reduce convection effects. When the mixtures were not clear they were diluted 1 to 10 (volume to volume) with filtered DI water to avoid multiple scattering. The measurements were also performed three times on each sample with an elapsed time of 10 min and the light scattering data was analyzed with the NNLS algorithm of the BI–DLSW control.

4.2.5 Conductivity and pH

Conductivity and pH measurements were performed with the instruments described in Section 3.2.4. Both, conductivity and pH measurements were conducted at (70 ± 0.5)°C; the temperature was controlled using a water bath with a digital thermometer (WVR Model 15551-000).

4.3 Results and discussion

4.3.1 Precursor mixtures of silicalite-1

Figure 4.2 shows the single-pulse ^{1}H NMR spectra of mixtures with composition *x* TPAOH: *y* TEOS: 7290 H_2O: 810 D_2O at 25°C (Figure 1a-c) and 70°C (Figure 1d-f). The chemical shift values of the signals show temperature dependence (notice the

different x-axis scales between the spectra at 25°C and 70°C). The ^{1}H NMR signals corresponding to the TPA organocation (A-C) experience a downfield shift between 210 and 235 Hz after increasing the temperature from 25°C to 70°C. The signals corresponding to the ethanol (D and E), which is a product of the hydrolysis of TEOS, also experience a downfield shift between 220 and 235 Hz after increasing the temperature. Although the water signal is not shown in the spectra of Figure 4.2, the chemical shift of the water protons remains practically constant at both temperatures (δ_{H2O} (25°C) = 4.68 ppm and δ_{H2O} (70°C) = 4.69 ppm, which is equivalent to a downfield shift of 5 Hz). For the organocations in water alone (Figure 4.2a,d), the intensities of the TPA cation signals (A-C) at 25°C are in general slightly larger than those at 70°C.[173] This phenomenon can be explained with the Boltzmann equation, which describes that as the thermal energy of the system increases a smaller difference in the populations between the lower and higher energy level is observed. Since the intensity of the NMR signal is proportional to the population difference, smaller signal intensities are expected at higher temperatures. In the presence of silica (Figure 1b,c,e,f), the intensities of the TPA organocation signals (A-C) at 25°C are in general slightly smaller than those at 70°C. One possible explanation in agreement with the investigation presented in Chapter III is that more organocation is bound to the silica at 25°C than at 70°C. This will be assessed in more detail below via PFG NMR.

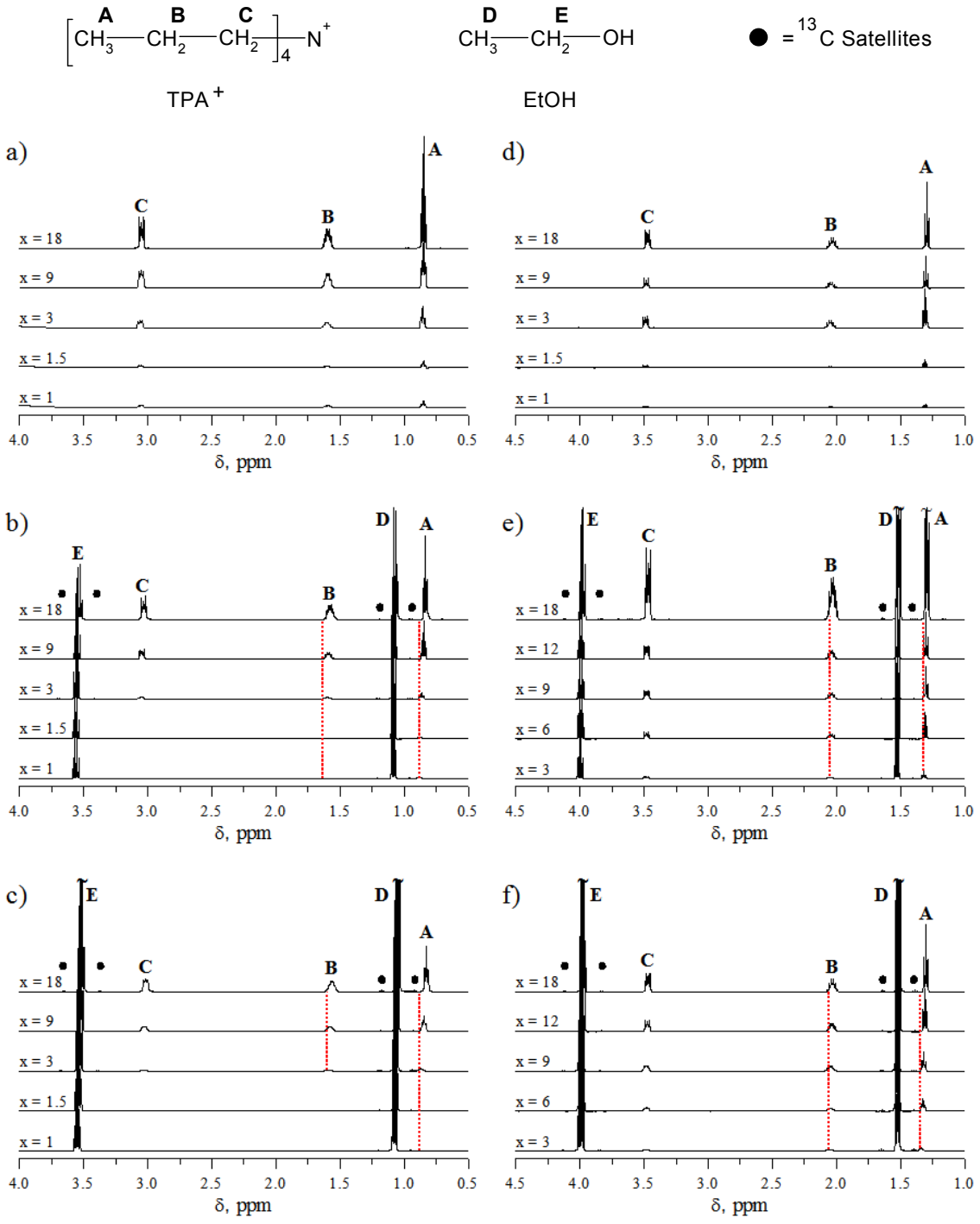

Figure 4.2 Single-pulse ^{1}H NMR spectra at 25°C (a-c) and 70°C (d-f) for mixtures with a molar composition of *x* TPAOH: *y* TEOS: 7290 H_2O: 810 D_2O where a,d) *y* = 0, b,e) *y* = 20, and c,f) *y* = 60.

Some TPA organocation resonances experience an upfield shift as a function of the organocation concentration. These changes in the chemical shift are summarized in Table 4.1. The organocation concentration in the organocation-water mixtures at 25°C does not affect the chemical shift values of the TPA organocation resonance. However, the organocation resonances experience a relatively small upfield shift of 10 Hz in the same mixtures at 70°C. This upfield shift is associated with an increase of the organocation shielding. The enhancement of the electron charge density of the organocation might be related with organocation-organocation interactions promoted by the temperature increase. In the presence of silica, the organocation resonances experience an upfield shift as the organocation concentration increases. In this case, the organocation experiences upfield shifts between 10 to 35 Hz at 25°C and between 10 to 20 Hz at 70°C. It is important to be aware that the upfield changes are calculated from $x = 1$ to $x = 18$ for most of the cation signals at 25°C, and from $x = 3$ to $x = 18$ for all the organocation signals at 70°C. Moreover, and consistently with the investigation on precursor mixtures, the upfield shift of the signals increased for the outer moieties ($\Delta\delta_A > \Delta\delta_B > \Delta\delta_C$). The ethanol signals experience a smaller upfield shift (5-10 Hz) than the organocation signals. Also, the chemical shift changes correlate with silica content, i.e., increasing silica content leads to larger shifts.

Table 4.1 Chemical shift changes of the organocation methyl resonances of Figure 4.2.

Composition	Shifted peaks	$\delta(x = 1)$, ppm	$\delta(x = 18)$, ppm	$\Delta\delta$, ppm ($\Delta\nu$, Hz)
T = 25°C				
x TPAOH: 7290 H_2O: 810 D_2O	None			
x TPAOH: 20TEOS: 7290 H_2O: 810 D_2O	A	0.88	0.83	0.05 (*25*)
	B	1.61	1.58	0.03 (*15*)
	C	3.05	3.03	0.03 (*10*)
x TPAOH: 60 TEOS: 7290 H_2O: 810 D_2O	A	0.90	0.83	0.07 (*35*)
	B	1.61[a]	1.57	0.04 (*20*)
	C	3.04[a]	3.02	0.02 (*10*)
T = 70°C				
x TPAOH: 7290 H_2O: 810 D_2O	A	1.31	1.29	0.02 (*10*)
	B	2.05	2.03	0.02 (*10*)
	C	3.49	3.47	0.02 (*10*)
x TPAOH: 20 TEOS: 7290 H_2O: 810 D_2O	A	1.32[a]	1.29	0.03 (*15*)
	B	2.05[a]	2.03	0.02 (*10*)
	C	3.49[a]	3.47	0.02 (*10*)
x TPAOH: 60 TEOS: 7290 H_2O: 810 D_2O	A	1.34[a]	1.30	0.04 (*20*)
	B	2.06[a]	2.03	0.03 (*15*)
	C	3.49[a]	3.47	0.02 (*10*)

[a] Chemical shift value at $x = 3$.

In Figure 4.3 the observed diffusion coefficients of TPA cation at 70°C for mixtures with a composition of *x* TPAOH: *y* TEOS: 7290 H_2O: 810 D_2O are showed. The TPA cation diffusion coefficients remain almost constant when the organocation is free in water and no silica is present. However, the diffusion coefficients slightly (~ 8%) decrease for the highest TPAOH concentrations which is likely due to a reduction in the organocation mobility caused by attractive organocation-organocation interactions. In the presence of silica (TEOS), the TPA cation diffusion coefficients increase with the organocation concentration but decrease with the addition of TEOS.

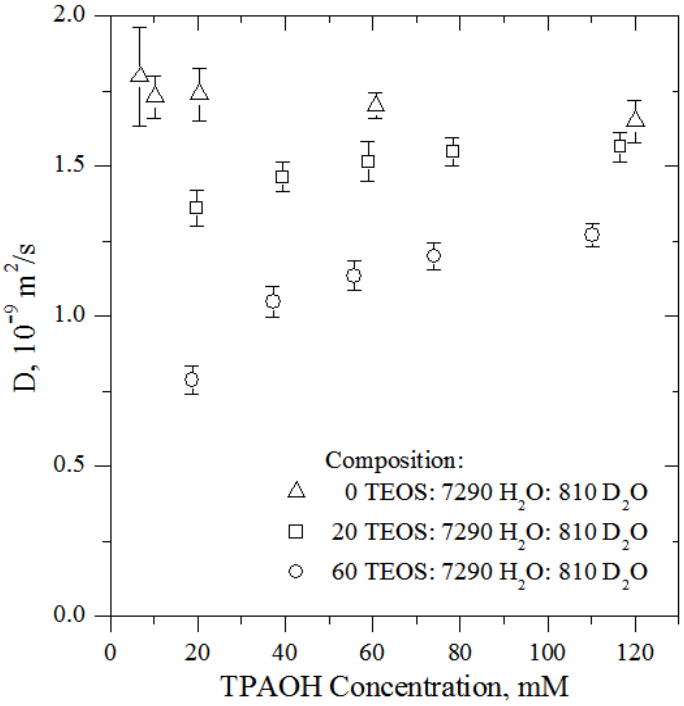

Figure 4.3 Diffusion coefficients of the TPA cation as a function of the total concentration of TPAOH for mixtures with a molar composition of *x* TPAOH: *y* TEOS: 7290 H_2O: 810 D_2O at 70°C. The error bars represent the line width of the signal in the diffusion dimension; the line width is determined with the estimated error of the diffusion coefficient as obtained from the fitting process.[168]

The observations of the TPA cation diffusion coefficients allow inferring that less organocation mobility is associated with lower organocation and higher silica (TEOS) contents. In other words, the organocation-silica interactions are stronger in the presence of more particles of silica and less molecules of organocation in the mixture. We observed larger diffusion coefficients at 70°C than at 25°C for the same TAPOH-TEOS-water mixtures reported in Chapter III, which is expected due to the increase in temperature. Even so, the trends in the diffusion coefficients are similar to those observed at 25°C.

The fraction of organocation that is bound to the silica (x_b) in the TPAOH-TEOS-water mixtures at 70°C can be calculated from the organocation diffusion coefficients using Eq. 3.4. The observed diffusion coefficients (D_{obs}) of the TPA cation are experimentally determined by PFG NMR spectroscopy from TPAOH-TEOS-water mixtures at 70°C (Figure 4.3). The free diffusion coefficient of TPA in water at 70°C is determined to be $(1.725 \pm 0.054) \times 10^{-9}$ m^2/s. The diffusion coefficient of the bound TPA cation (D_b) is assumed to be the diffusion coefficient of a silica particle. DLS measurements on a mixture with a molar composition of 12 TPAOH: 60 TEOS: 7290 H_2O: 810 D_2O at 70°C show that the particle size distribution is not unimodal. The distribution shows small (5 nm in diameter) and large (200 nm in diameter) particles that the analysis below considers in the calculation of the bound fraction. The diffusion coefficients of the small and large particles are determined to be 2.49×10^{-10} m^2/s and 6.22×10^{-12} m^2/s, respectively. Figure 4.4 shows the fraction and amount of cation bound

to 5 nm (filled symbols) and 200 nm (open symbols) silica particles for TPAOH-TEOS-water systems at 70°C.

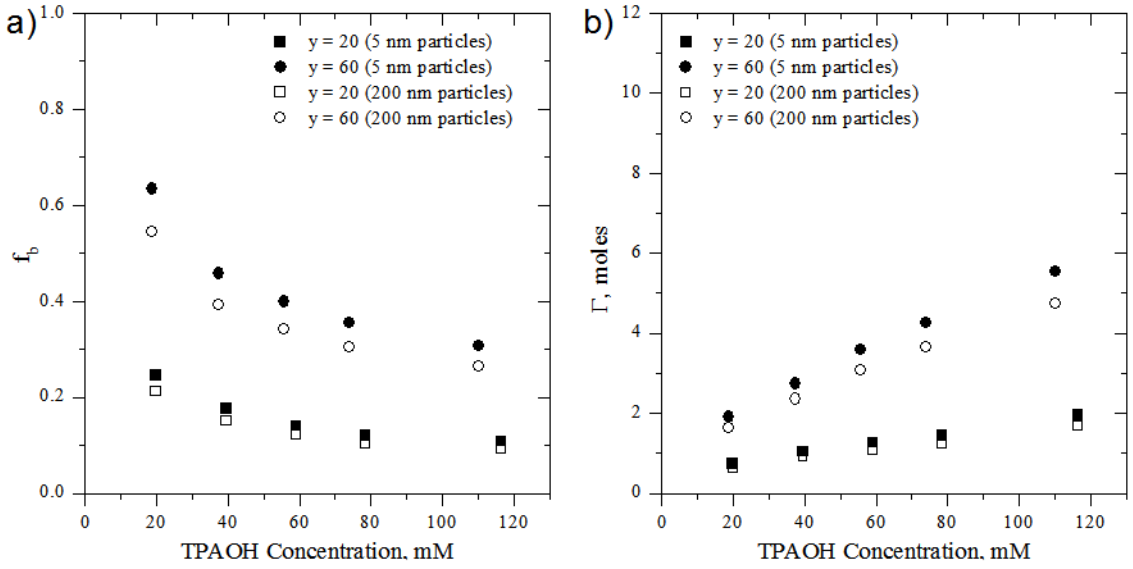

Figure 4.4 a) Fraction of bound organocation (f_b) and b) amount of bound cation (Γ) as a function of the total concentration of TPAOH for mixtures with a molar composition of x TPAOH: y TEOS: 7290 H_2O: 810 D_2O at 70°C.

Neither the fraction nor the amount of bound organocation depends strongly on the size of silica particles because Eq. 3.4 is not very sensitive to the error of D_b. Though the amount of bound organocation as a function of the total concentration of TPAOH at 70°C also shows an increasing trend, the plots in Figure 4.4 are more linear than those of analogous mixtures at 25°C. Moreover, the convergence towards a plateau at 70°C is not as clear as at 25°C. This suggests that no saturation of the silica particles occurs in these precursor mixtures at 70°C. One explanation of this behavior is that since the organocation mobility is higher at 70°C than at 25°C, a much higher concentration of TPAOH in the mixture is needed to observe saturation.

In order to calculate the binding energy of the TPA cation the data in Figure 4.4b is analyzed using the Langmuir and Freundlich isotherms. The linear form of the Langmuir isotherm is the Lineweaver-Burk equation

$$\frac{1}{\Gamma} = \frac{1}{\Gamma_{\max}} + \frac{1}{\Gamma_{\max} K_{ad} C} \tag{3.6}$$

where Γ is the amount of bound organocation, Γ_{max} is the maximum amount of bound organocation, K_{ads} is the adsorption constant, and C is the equilibrium concentration of the organocation in the mixture. In this chapter, the adsorption constant calculated with the Langmuir model is referred as K_L to distinguish it from that calculated with the Freundlich model. The Langmuir model makes several assumptions. These assumptions consider that adsorption occurs on flat surfaces with equivalent sites allowing only monolayer coverage, the energy of adsorption is the same for all the sites and independent of surface coverage, and no interactions between the adsorbate molecules are present. The linear form of the Freundlich isotherm is given by the equation

$$\log(\Gamma) = \log(K_F) + \frac{1}{n}\log(C) \tag{4.1}$$

where Γ is the amount of bound organocation, K_F is the adsorption constant calculated with the Freundlich model, C is the equilibrium concentration of organocation in the mixture, and 1/n is a correction factor called heterogeneity factor. This model isotherm considers heterogeneous adsorptive energies on the absorbent surface,[174] but it does not predict the maximum amount of bound adsorbate molecules.[175] The Lineweaver-Burk and the Freundlich linearization of the amount of bound organocation are shown in

Figure 4.5 and 4.6, respectively. The parameters calculated from these fittings, the statistics, and the binding energies are summarized in Table 4.2.

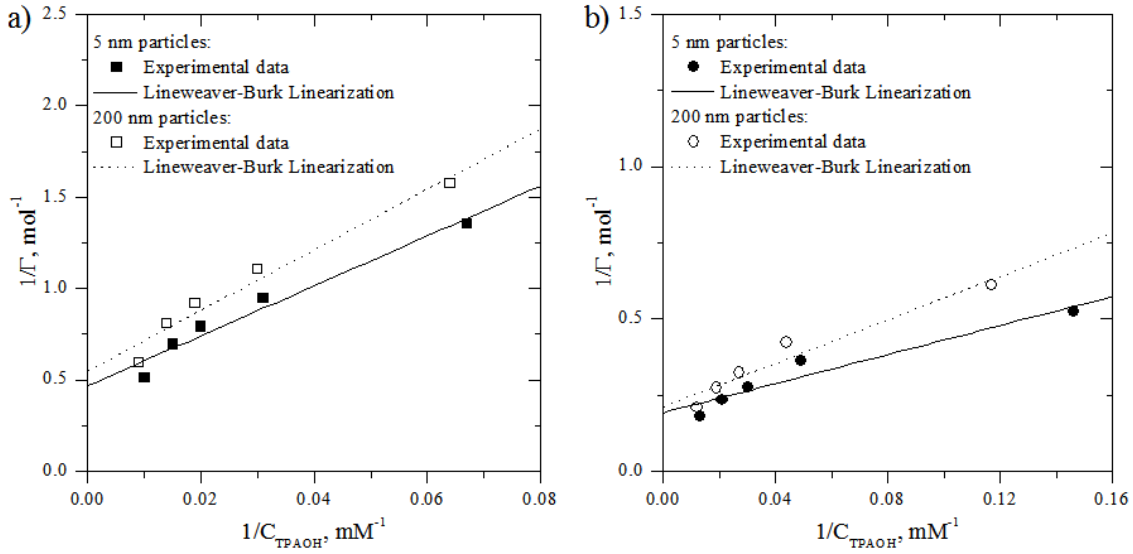

Figure 4.5 Lineweaver–Burk plots for mixtures with a molar composition of *x* TPAOH: *y* TEOS: 7290 H_2O: 810 D_2O at 70°C where a) *y* = 20 and b) *y* = 60.

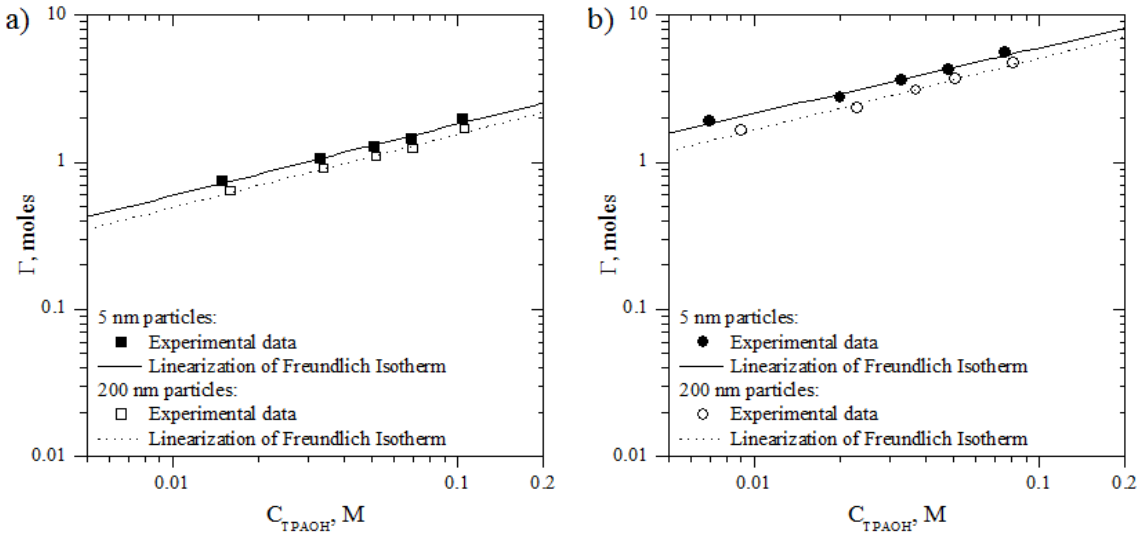

Figure 4.6 Linear Freundlich plots for mixtures with a molar composition of *x* TPAOH: *y* TEOS: 7290 H_2O: 810 D_2O at 70°C where a) *y* = 20 and b) *y* = 60.

Table 4.2 Fitting parameters, statistics, and adsorption energy for mixtures with a molar composition of *x* TPAOH: *y* TEOS: 7290 H_2O: 810 D_2O.

Langmuir model	K_L, L/mol	Γ_{max}, moles	R^2	σ [a]	$K_{ads} = K_L$, mol/L	ΔG_{ad}, kJ/mol
5 nm particles						
$y = 20$	35.0	2.11	0.960	0.073	35.0	-10.14
$y = 60$	81.3	5.18	0.927	0.042	81.3	-12.55
200 nm particles						
$y = 20$	32.7	1.84	0.962	0.082	32.7	-9.95
$y = 60$	59.4	4.73	0.941	0.044	59.4	-11.65
Freundlich model	K_F, $L^{1/n}mol^{(n-1)/n}$	Γ_{max}, moles	R^2	σ [a]	K_U range, mol/L	ΔG_{ad}, kJ/mol
5 nm particles						
$y = 20$	5.1	2.07	0.986	0.022	9.4 – 61.3	(-6.39) – (-11.74)
$y = 60$	16.4	2.27	0.986	0.024	16.1 – 149.0	(-7.93) – (-14.28)
200 nm particles						
$y = 20$	4.8	2.04	0.986	0.021	9.0 – 57.6	(-6.27) – (-11.56)
$y = 60$	15.0	2.12	0.990	0.021	67.3 – 189.8	(-12.01) – (-14.97)

[a] Residual standard deviation defined as $\sigma = (Q/n_{obs} - p)^{1/2}$, where Q is the objective function, n_{obs} is the number of observations, and p is the number of parameters in the model.

Comparison of Figure 4.5 and 4.6, the determination coefficients (R^2), and the residual standard deviation (σ) indicate that the Freundlich model describes the isotherms better than the Langmuir model. Although the fittings with the Langmuir

isotherm might be considered acceptable ($R^2 > 0.92$ and $\sigma < 0.09$), deviations of the model can be observed at low TPAOH equilibrium concentrations (i.e., high values of $1/C_{TPAOH}$). This causes an over-prediction of the adsorption constant. Deviations of the Langmuir model at low TPAOH equilibrium concentrations are also observed in organocation-TEOS-water mixtures at 25°C (Chapter III). For those mixtures, the data is well described with the Langmuir isotherm and the deviations of the isotherm are ascribed to the assumptions of the Langmuir model and to its Lineweaver–Burk linearization, which is more susceptible to data errors at low concentrations. In the investigation presented in this chapter, deviations from the Langmuir isotherm might be due to the fact that this model isotherm does not consider heterogeneous adsorption sites and organocation-organocation interactions. These interactions are more likely to occur at 70°C even in diluted mixtures (i.e., mixtures with 8100 moles of water).

On the other hand, fittings to the Freundlich isotherm show larger determination coefficients and smaller residual standard deviations than fittings to the Langmuir isotherm. This is likely to occur since the Freundlich isotherm considers to some extent the roughness of the particle and particle heterogeneity; these features of the particle are not considered by the Langmuir model but might affect the adsorption process since the organocation likely binds the most favorable sites first. The Freundlich adsorption constants (K_F) can be compared between themselves because the heterogeneity factor is very similar for all the Freundlich fittings (n ~ 2). However, they cannot be directly compared with the Langmuir adsorption constants (K_L), because their values and units vary nonlinearly depending on the heterogeneity factor n. Then, in order to compare the

adsorption constants estimated with the Langmuir and Freundlich isotherms, a new variable that unifies the Freundlich adsorption constant (K_F) and the heterogeneity factor (n) is used.[176] This mathematical transformation of the Freundlich adsorption constant does not take into account the conceptual differences between K_F and K_L. The unified constant K_U has the same units as K_L and is given by the equation

$$K_U = \left(\frac{K_F}{\Gamma} \right)^n \tag{4.2}$$

In Table 4.2 we can observe that, for a given particle size and concentration of TEOS, the Langmuir adsorption constants (K_L) are within the range of K_U. The adsorption constants have similar values for the adsorption over 5 nm and 200 nm silica particles, but they increase as the concentration of TEOS increases. Moreover, larger adsorption Gibbs energies are determined at higher concentrations of TEOS. The adsorption Gibbs energies are very similar to those determined at 25°C.[170]

The cation monolayer coverage is calculated with the Langmuir parameter of the maximum amount of bound cation (Γ_{max}) assuming that the silica particles have a core of 356 silicon atoms[68] (i.e., 5 nm particles). The organocation monolayer coverage is presented in Table 4.3. A larger amount of organocation seems to be adsorbed by the silica particles for the mixtures with the lowest content of TEOS. Since this behavior can be due to lower availability of silica particles per organocation at low TEOS concentrations, it is important to point out that many assumptions are made in this calculation and that the Langmuir isotherm does not fit the data as well as the Freundlich isotherm.

Table 4.3 Organocation monolayer coverage of silica nanoparticles in mixtures with a molar composition of *x* TPAOH: *y* TEOS: 7290 H_2O: 810 D_2O.

TEOS	No. of organocations/particle
y = 20	64
y = 60	36

4.3.2 Time evolution of a silicalite-1 synthesis mixture heated at 70°C

The time evolution of a mixture with molar composition of 12 TPAOH: 60 TEOS: 7290 H_2O: 810 D_2O has been monitored at 70°C. The pH has been measured at 70°C during the silicalite-1 crystallization of this mixture (Figure 4.7). The increasing trend of pH with time is consistent with the observations of Rimer et. al.[177] for the synthesis at 95°C of a more concentrated mixture with a molar composition of 9 TPAOH: 25 TEOS: 480 H_2O, although pH values higher than the ones of the mixture investigated here were observed. In accordance with the observations of Rimer et. al.,[177] the pH increases when the concentration of the silica species in the mixture decreases. During this process, the amount of silica in the bulk mixture will decrease as the zeolite particles increase in size and number. This change in the silica concentration, and therefore the increase in the pH of the mixture, is associated with an exothermic-endothermic transition that occurs during the silicalite-1 crystallization near the end of the synthesis.[177] In the mixture studied here, this transition appears to be occurring between t = 5 days and t = 8 days. Conductivity measurements at 70°C are in agreement with the pH results and show an increase in the conductivity from 2.97 mS/cm (at t = 0 days) to 45.8 mS/cm (at t = 8 days).

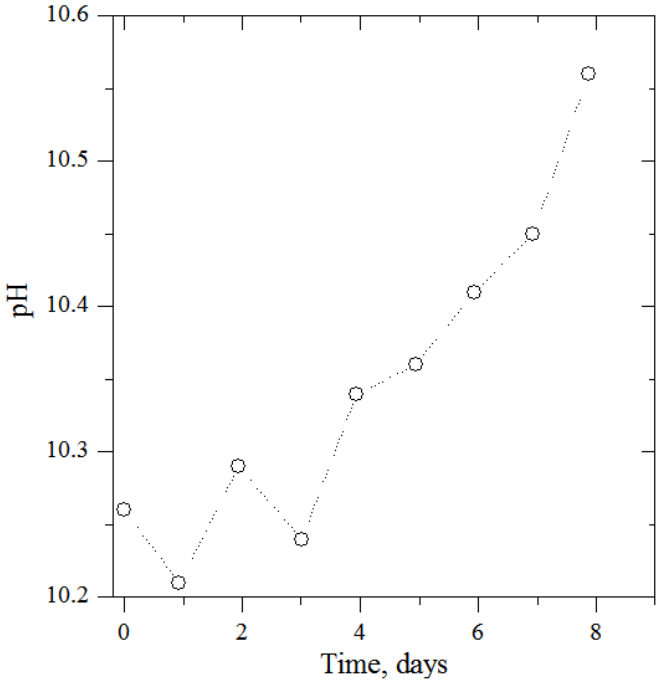

Figure 4.7 pH as a function of time for a mixture with a molar composition of 12 TPAOH: 60 TEOS: 7290 H_2O: 810 D_2O at 70°C. (t = 0 days corresponds to the precursor mixture measured at 70°C right after a 24 h period of aging and mixing).

DLS measurements were conducted to monitor the size of the silica particles in the same mixture at 70°C (Figure 4.7). In order to avoid multiple scattering the mixtures were diluted 1:10 in volume with deionized water when they became turbid ($t \geq 3$ days). Figure 4.8a displays the intensity-weighted size distributions and Figure 4.8b displays the number-weighted size distributions. Because DLS does not detect the particles individually but the intensity of the scattered light, the intensity-weighted distributions are considered as more reliable since they are closer to the raw data. On the other hand, number-weighted distributions give more useful information regarding to the number of particles present in the mixture. However, number-weighted distributions are only a mathematical transformation that allows estimating the number of particles and might be

affected by the polydispersity of the sample. The intensity-weighted plots show trimodal (~ 2 nm, 25 nm and 300 nm in diameter) and polydisperse distributions for the clear mixtures ($t \leq 2$ days). These distributions become bimodal when the samples become turbid ($t = 3$ days). As the time increases ($t \geq 4$ days) the distributions become unimodal and monodisperse. At the end of the synthesis ($t = 8$ days) the silica particles are about 230 nm in diameter. On the other hand, the number-weighted plots only show particles of less than 20 nm in diameter for the clear mixtures ($t \leq 2$ days). More monodisperse distributions with bigger particle sizes are observed as the time increases ($t \geq 3$ days). Comparison of Figure 4.8a and 4.8b indicates that some aggregates (~300 nm in diameter) might be present in the clear mixtures. Nevertheless, the amount of aggregates might be overestimated with the intensity-weighted plots because the scattered intensity scales nonlinearly with the particle size. The results suggest that silica particles of relatively small size (< 20 nm) and few aggregates (~ 300 nm) are present at the beginning of the silicalite-1 synthesis. Restructuration of the silica species seems to occur after heating the mixture at 70°C for several days leading to the formation of particles of approximately 230 nm in diameter at the end of the synthesis.

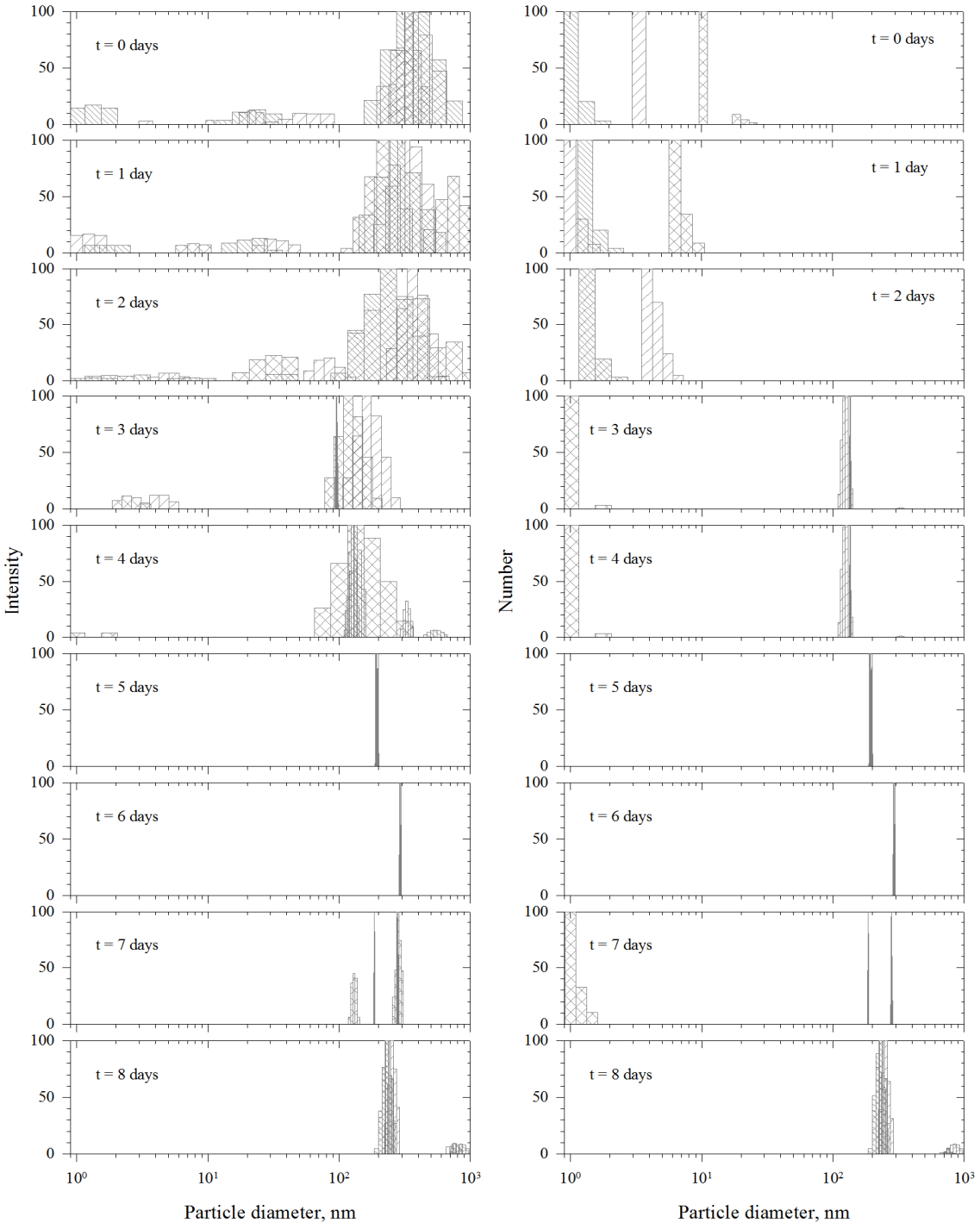

Figure 4.8 NNLS particle size distributions weighted by a) intensity and b) number of particles at 70°C as a function of time for a mixture with a molar composition of 12 TPAOH: 60 TEOS: 7290 H_2O: 810 D_2O. Up diagonal hatched bar, 1st run; down diagonal hatched bar, 2nd run; and double hatched bar 3rd run.

Silicalite-1 crystallization was also monitored by single-pulse ^{1}H NMR experiments conducted at 70°C. The single-pulse ^{1}H NMR spectra at 70°C as a function of time are shown in Figure 4.9. Neither a considerable shift nor signal broadening is observed for the organocation resonances as the time increases. Only a decrease in the signal intensity is observed at t = 6 days.

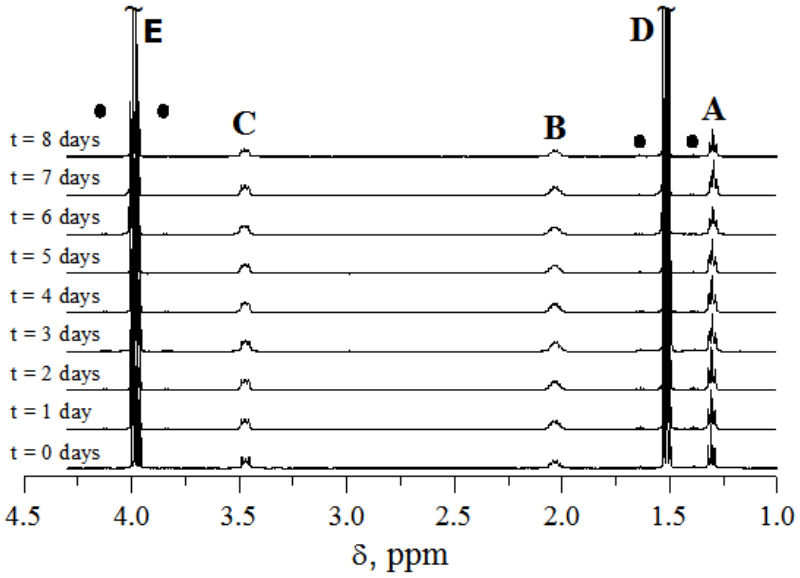

Figure 4.9 Single-pulse ^{1}H NMR spectra at 70°C as a function of time for a mixture with a molar composition of 12 TPAOH: 60 TEOS: 7290 H_2O: 810 D_2O.

In order to get more information about the mobility of the TPA cation during the silicalite-1 crystallization, PFG NMR experiments at the same temperature (70°C) and on the same mixture (12 TPAOH: 60 TEOS: 7290 H_2O: 810 D_2O) have been also conducted. The diffusion coefficients of the TPA cation at 70°C (referred to the water diffusion coefficient) as a function of time are shown in Figure 4.10. The organocation diffusion coefficient remains almost constant at the beginning of the synthesis when the mixture is clear ($t \leq 2$ days), but it starts to increase when the mixture starts to become

turbid (t = 3 days). The organocation diffusion coefficient reaches a maximum at $t \sim 6$ days, slightly drops at $t \sim 7$ days, and finally trends towards a plateau at $t \sim 8$ days. It is important to mention that some solids were observed in the mixture from day 6 onwards, but they were allowed to sediment before acquiring the NMR data. One interpretation of the results in Figure 4.10 is that upon heating there is less TPA cation bound to the external surface of the particles. Moreover, the TPA cation in the bulk diffuses faster promoting that the silica species restructure while acting as a template. These findings are consistent with the idea that upon heating and particle growth, there is less external surface area on which the TPA can be adsorbed. However, it is expected that some TPA cations will be trapped inside the growing crystals. Assuming that all the silica present in the mixture were in the form of silicalite-1 and that the crystals have an ideal unit-cell with a TPA/SiO_2 ratio of 1/24,[34] approximately one fifth of the total TPA present in the mixture would be occluded in the growing particles. It is important to point out that it is very likely that TPA occluded in the growing particles does not contribute to the diffusion measurements. Two reasons can be given to justify this hypothesis. First, it should be expected that TPA encapsulated in silica had a dramatically reduced spin-spin relaxation time (T_2) due to restricted mobility. These spin-spin relaxation times are typically on the order of a few milliseconds for molecules adsorbed on zeolites.[178] For this reason, very broad signals are observed for the occluded TPA in silicalite–1 (even in the presence of magic angle spinning) as compared to the signals of the TPA in the bulk mixture.[109] Therefore, it is very likely that occluded TPA does not contribute to the intensity of the NMR signals observed in this investigation. Second, if the occluded TPA

contributed to the intensity of the observed signals, the PFG NMR experiments would not attenuate its signal with the strongest gradient because the mean diameter of the growing particles (which is in the order of 10^2 nm), is much smaller than the root mean square displacement of the TPA molecules (which is in the order of 10^3–10^4 nm).[145,178] Therefore, the TPA occluded in the growing particles should not contribute to the diffusion coefficient determined from the PFG NMR experiments.

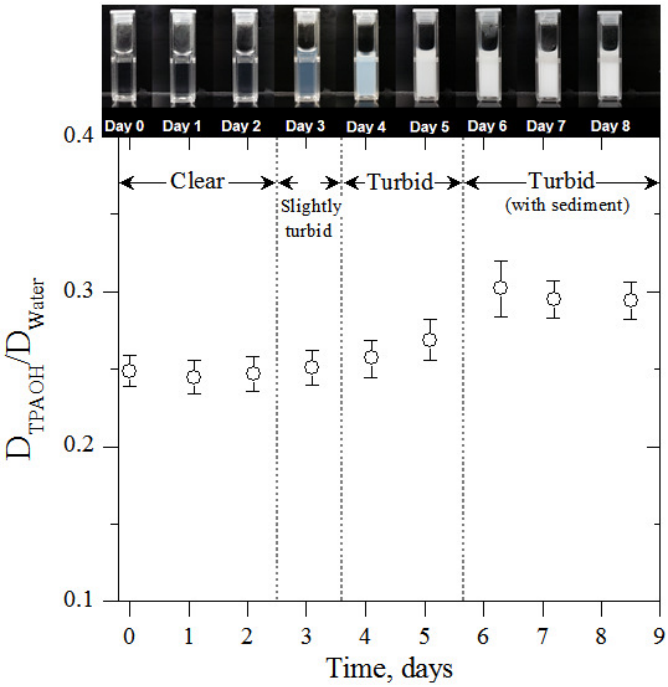

Figure 4.10 Observed diffusion coefficients of the TPA cation at 70°C (referred to the water diffusion coefficient) as a function of time for a mixture with a molar composition of 12 TPAOH: 60 TEOS: 7290 H_2O: 810 D_2O. The water diffusion coefficient determined from a sample with a molar composition of 90% H_2O in D_2O at 70°C was 5.572 ± 0.092 x 10^{-9} m^2/s.[173] This value is in agreement with the water diffusion coefficients reported by Holtz et. al.[179]

The maximum diffusion coefficient observed at t ~ 6 days might be associated with the exothermic-endothermic shift reported by Vlachos et. al.[177] Self-assembly of the

primary silica particles is supposed to occur during the exothermic process, while the completion of crystallization is supposed to occur at the end of the endothermic process.

4.4 Conclusions

In situ PFG NMR experiments are shown to be feasible to monitor organocation-silica interactions at zeolite synthesis conditions. The results on TPAOH-TEOS-water mixtures at 70°C reported in this chapter show comparable adsorption Gibbs energies for precursor mixtures at 25°C. However, the adsorption data at 70°C does not fit the Langmuir isotherm well as compared to the data at 25°C. Larger deviations at 70°C are ascribed to assumptions in the Langmuir isotherm that might not apply as well at higher temperatures. Therefore, the Freundlich isotherm that considers heterogeneous sites to some extent was used showing a better fit of the adsorption data at 70°C. The time evolution of the silicalite-1 synthesis has been also monitored via diffusion NMR. PFG NMR shows that the diffusion coefficients increase at the beginning of the synthesis, reach a maximum during the exothermic-endothermic transition, and trend to a plateau at the end of the synthesis. Thus, the current work shows that in situ PFG NMR techniques allow determining the strength of the organocation-silica interactions and their time evolution during the silicalite-1 crystallization. This fundamental knowledge should contribute to a more detailed molecular description of zeolite nucleation and growth that ultimately leads to routes for the rational design and control of zeolite syntheses.

CHAPTER V

SYSTEMATIC INVESTIGATION OF SILICALITE-1 PRECURSOR MIXTURES WITH VARYING DEGREES OF DILUTION

5.1 Introduction

As discussed in previous chapters, optically transparent mixtures of silicalite-1 have been widely investigated using spectroscopy, microscopy, calorimetry, and scattering.[38,43-46,50,55,58-70,79,80,170,173,180-182] However, the scattering studies have at times been inconsistent with one another, and there is still significant controversy in the literature regarding to the detailed processes being observed in these mixtures. One challenge in reviewing these studies is that very few of the literature reports from different research groups investigate mixtures with the same composition. The wide range of compositions for TPAOH-TEOS-H_2O mixtures studied in some of the previous works is illustrated in Figure 5.1. Varying the composition affects the properties of these mixtures by changing important parameters such as the pH. Given that these mixtures are highly sensitive to pH,[183] comparison between results of mixtures with different composition and (sometimes unreported) pH is not trivial. Moreover, generating conclusions from the comparison of results between 'concentrated' and 'dilute' mixtures can be particularly difficult.

The goal of the investigation presented in this chapter is to elucidate the effects of the composition in the distribution of species in precursor mixtures and the implications of these effects in the final zeolite phase. In order to achieve this goal,

several mixtures have been synthesized and characterized prior to heating over a wide expanse of the composition space (see Figure 1) and the effect of the composition on the conductivity, pH, and particle size distribution (PSD) in precursor mixtures of silicalite-1 has been investigated. The outcome of this investigation should provide a better understanding about precursor mixtures of silicalite-1 and help to unify the findings on nucleation and growth of silicalite-1.

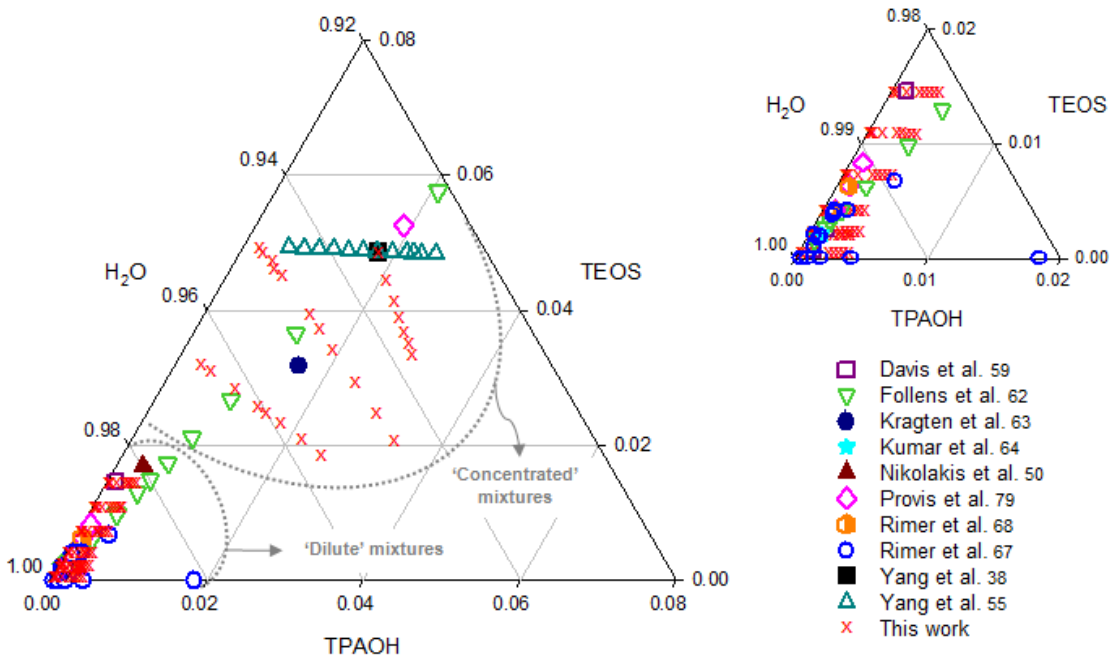

Figure 5.1 Ternary diagram showing the molar fractions of TPAOH, TEOS and H_2O in silicalite-1 mixtures studied in the previous and the present investigation. The mixtures with a relatively low content of water are referred as 'concentrated' mixtures, while the mixtures with a relatively high content of water are referred as 'dilute' mixtures. The inset amplifies the compositions for 'dilute' mixtures.

5.2 Experimental

5.2.1 Materials

Tetrapropylammonium hydroxide (TPAOH, Alfa Aesar, 40% w/w aq. soln.) and tetraethyl orthosilicate (TEOS, Aldrich, ≥ 99.0% and Fluka, > 99.0%) were used as received. Phosphate pH buffer (Beckman Coulter, pH 7.00 ± 0.01 at 25°C) and carbonate pH buffer (Beckman Coulter, pH 10.01 ± 0.01 at 25°C) were used for the calibration of the pH meter. Conductivity calibration solution (VWR, 718 micro-Mho ± 1 at 25°C, 0.005 N KCl) was used to calibrate the conductivity meter. Dilute aqueous suspensions of micro particle size standard based on monodisperse polystyrene (Fluka, size: 0.2 μm and 0.5 μm) were used for performance verification of the Brookhaven ZetaPALS instrument.

5.2.2 Precursor mixtures of silicalite-1 synthesis

Mixtures with a molar composition of x TPAOH: y TEOS: z H_2O were prepared in several sets. The sets are summarized in Table 1. Sets S1 to S7 correspond to the 'dilute' mixtures, since sets S8 to S10 correspond to the 'concentrated' mixtures. Since TEOS speciation is not totally understood, the compositions of the mixtures given in Table 1 are based on the TEOS content added to the mixture rather than on the expected SiO_2 content.

Each set of mixtures was prepared as follows. First, the mixture containing the lowest concentration of TPAOH in the set (e.g., mixtures with x = 1 for 'dilute' systems) was prepared as described in Chapter III, Section 3.2.2. Previous DLS investigations on silicalite-1 have reported that the synthesis mixtures were filtered after their preparation

but prior to DLS analysis.[46,63,66,70,159,180-182] However, removal of silicate species formed during the aging and mixing period might occur by following this procedure. Therefore, for the mixtures investigated here, the solvent (DI water) used in the mixture preparation was filtered through a 0.2 μm cellulose acetate filter in order to remove any foreign particulate matter (dust) that could interfere later with the DLS analysis. The initial TPAOH-TEOS-H_2O mixture was placed in a screw-cap Teflon container and was aged for 24 hours while mixing at room temperature to ensure full hydrolysis of TEOS. The resulting precursor mixture, which contained the lowest concentration of TPAOH, was measured. Subsequent mixtures belonging to the same set were prepared by addition of TPAOH solution to this precursor mixture until the set of mixtures was completed. Changes in the water composition due to addition of TPAOH solution were neglected in the preparation of 'dilute' mixtures (sets S1 to S7) since the largest error introduced in the molar composition due to these changes is less than 10%. However, these changes in water content were considered in the preparation of 'concentrated' mixtures (sets S8 to S10) and therefore, the TPAOH addition was represented as an increase in the TPAOH/TEOS (x/y) molar ratio. All mixtures were transparent and only few of them belonging to the 'concentrated' sets (mixtures from set S8 with x/y = 0.10-0.34 and from set S10 with x/y = 0.04-0.12) had a viscous, gel-like appearance.

5.2.3 Dynamic light scattering

DLS measurements were conducted at 25°C in the instrument described in Section 3.2.5. Precursor mixtures were loaded in PMMA cuvettes (VWR 58017-875, 4.5 ml volume) that were properly cleaned to avoid dust. The measurements were also

conducted three times on each sample over a period of 10 min in order to ensure repeatability. The light scattering data was analyzed with the NNLS algorithm provided with the BI–DLSW control software. The viscosity of the medium was 0.890 cP (at 25°C) and the refractive index (RI) was 1.331 for the medium and 1.475 for the particles. The latter value was used in the mathematical transformation from intensity-weighted to volume- or number-weighted PSDs.

Table 5.1 Composition of the mixtures investigated in this research.

Set	Molar ratio
S1[a]	x TPAOH: 5 TEOS: 8100 H_2O
S2[a]	x TPAOH: 20 TEOS: 8100 H_2O
S3[a]	x TPAOH: 60 TEOS: 8100 H_2O
S4[a]	x TPAOH: 90 TEOS: 8100 H_2O
S5[a]	x TPAOH: 120 TEOS: 8100 H_2O
S6[a]	x TPAOH: 20 TEOS: 9500 H_2O
S7[a]	x TPAOH: 40 TEOS: 9500 H_2O
S8[b]	x TPAOH: y TEOS: 200 H_2O
S9[c]	x TPAOH: y TEOS: 300 H_2O
S10[d]	x TPAOH: y TEOS: 480 H_2O

[a] x = 1, 1.5, 3, 9, 18, 21, 24, 27, and 30 for S1 to S7.
[b] x/y = 0.10, 0.15, 0.34, 0.42, 0.56, 0.83, 1.17, and 1.61 for S8.
[c] x/y = 0.10, 0.15, 0.33, 0.53, 0.60, 0.76, 1.03, and 1.35 for S9.
[d] x/y = 0.04, 0.06, 0.12, 0.36, 0.46, 0.56, 0.65, 0.73, 0.81, and 0.88 for S10.

5.2.4 Conductivity and pH

Conductivity and pH measurements were conducted using the instruments described in Section 3.2.4. All conductivity and pH measurements were conducted at room temperature.

5.3 Results and discussion

5.3.1 'Dilute' mixtures

In this section, results for 'dilute' mixtures (sets S1 to S7) are discussed. Figure 5.2 shows a contour plot of the conductivity for precursor mixtures with a molar composition of *x* TPAOH: *y* TEOS: 8100 H_2O (sets S1-S5). The conductivity increases with the TPAOH content (*x*) and decreases with the TEOS content (*y*) which is consistent with results previously published.[61] The inset compares the conductivity between mixtures with a molar composition of *x* TPAOH: *y* TEOS: 8100 H_2O (with *y* = 20 for set S2) and *x* TPAOH: *y* TEOS: 9500 H_2O (with y = 20 for set S6 and y = 40 for set S7). For a given TPAOH and TEOS content, the conductivity does not change significantly when the water content was increased in the mixtures from 8100 to 9500 moles of water. Also, it can be confirmed from the inset that the conductivity decreases in these 'dilute' mixtures when the TEOS content increases.

Previous investigations have reported that the conductivity and pH behavior can be explained on the basis of the silica chemistry of these mixtures.[61] Typically, polymerization of silica to colloidal TPA-silica particles occurs in TPAOH-TEOS-H_2O precursor mixtures. Colloidal TPA-silica particles seem to show a phase behavior and display a critical aggregation concentration (cac) below which the silica species are

present as monomers and small oligomers, and above which the silica forms uniform nanoparticles in the mixture.[61] This cac is usually observed as a breakpoint in the conductivity and pH curves. In the region below the cac, conductivity and pH drop quickly as the silica concentration increases. In the region above the cac, conductivity and pH decrease slowly with the silica concentration. The cac is expected to occur at TEOS/TPAOH ~ 1,[80] and it has been drawn in Figure 5.2 at TEOS/TPAOH = 1 as a dotted line.

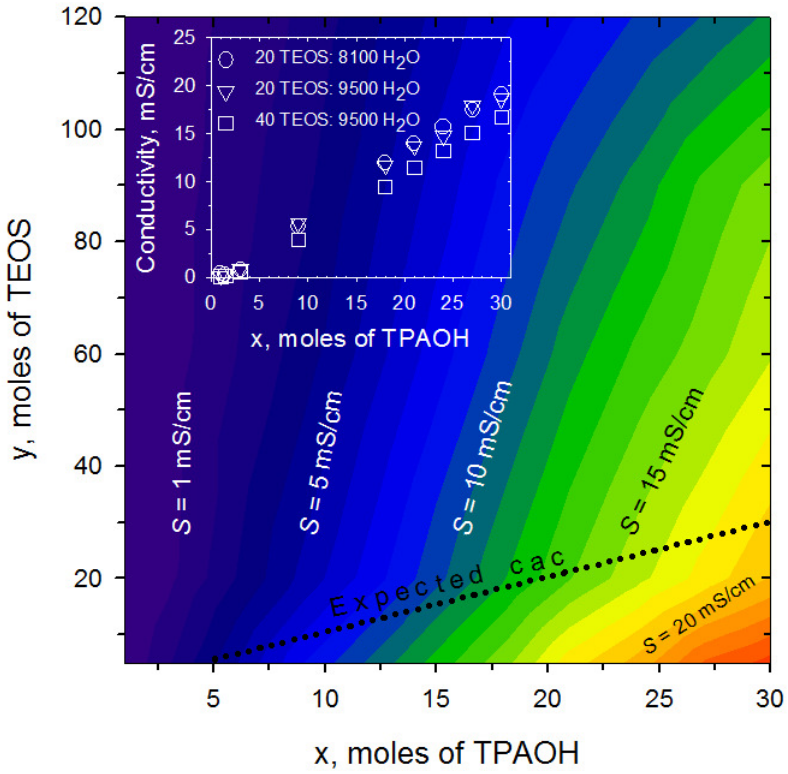

Figure 5.2 Contour plot displaying the conductivity for precursor mixtures with a molar composition of *x* TPAOH: *y* TEOS: 8100 H_2O. The inset shows a comparison of the effect of the composition on the conductivity between mixtures with a molar composition of *x* TPAOH: *y* TEOS: 8100 H_2O (where *y* = 20) and *x* TPAOH: *y* TEOS: 9500 H_2O (where *y* = 20 and 40).

Figure 5.3 shows a contour plot of the pH for precursor mixtures with a molar composition of *x* TPAOH: *y* TEOS: 8100 H_2O (sets S1-S5). The inset compares the pH between mixtures with a molar composition of *x* TPAOH: *y* TEOS: 8100 H_2O (with *y* = 20 for S2) and *x* TPAOH: *y* TEOS: 9500 H_2O (with *y* = 20 for S6 and *y* = 40 for S7). The cac locus (dotted line), expected to occur at TEOS/TPAOH ~ 1,[80] was also drawn in this plot. The pH increases with the TPAOH content and decreases with the TEOS content, which is consistent with the conductivity data. No significant changes in pH between mixtures with 8100 and 9500 moles of water can be observed in the inset.

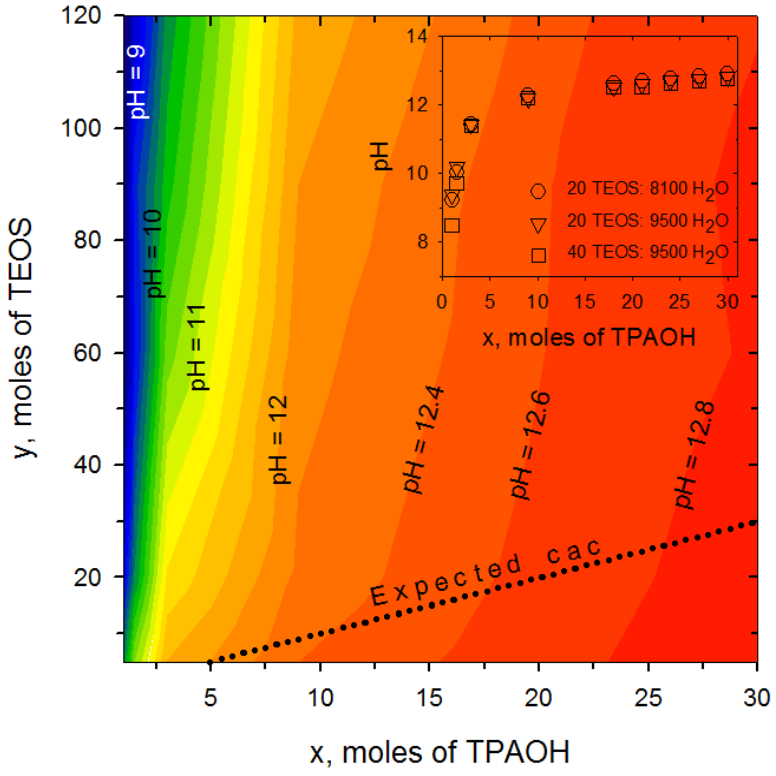

Figure 5.3 Contour plot displaying the pH for precursor mixtures with a molar composition of *x* TPAOH: *y* TEOS: 8100 H_2O. The inset shows a comparison of the effect of the composition on the conductivity between mixtures with a molar composition of *x* TPAOH: *y* TEOS: 8100 H_2O (where *y* = 20) and *x* TPAOH: *y* TEOS: 9500 H_2O (where *y* = 20 and 40).

Figures 5.2 and 5.3 show conductivity and pH data on 63 mixtures, and thus represent a broad range of the composition space for the 'dilute' precursor mixtures of silicalite-1 that have been broadly studied in the zeolite community.

DLS measurements were performed on dilute mixtures from sets S1 to S5 in order to determine their particle size distribution (PSD). PSDs presented here were intensity-weighted unless otherwise stated. As mentioned in Section 4.3.2, the intensity-weighted distributions are considered more reliable than other weighted distributions such as the number-weighted or volume-weighted ones because DLS measures fluctuations in the scattered light intensity rather than number or volume of particles. However, intensity-weighted PSDs can over predict the number of aggregates in the mixture because the intensity of the scattered light is proportional to the sixth power of the particle diameter. Therefore, larger particles scatter more strongly than smaller particles. This point will be discussed with more detail below. In Figure 5.4 the distribution mode of the particles in mixtures with a molar composition of x TPAOH: y TEOS: 8100 H_2O is showed. Bimodal and trimodal distributions of particles are observed in these mixtures. Most of the mixtures have trimodal distributions but three small bimodal distributions regions can be observed: the first at low TPAOH and TEOS content, the second and the largest at high TPAOH and low TEOS content, and the third at medium TPAOH and high TEOS content. It is noteworthy to point out that the first and the second regions were near to the expected cac locus and that the second and largest bimodal distribution region is mostly below the cac.

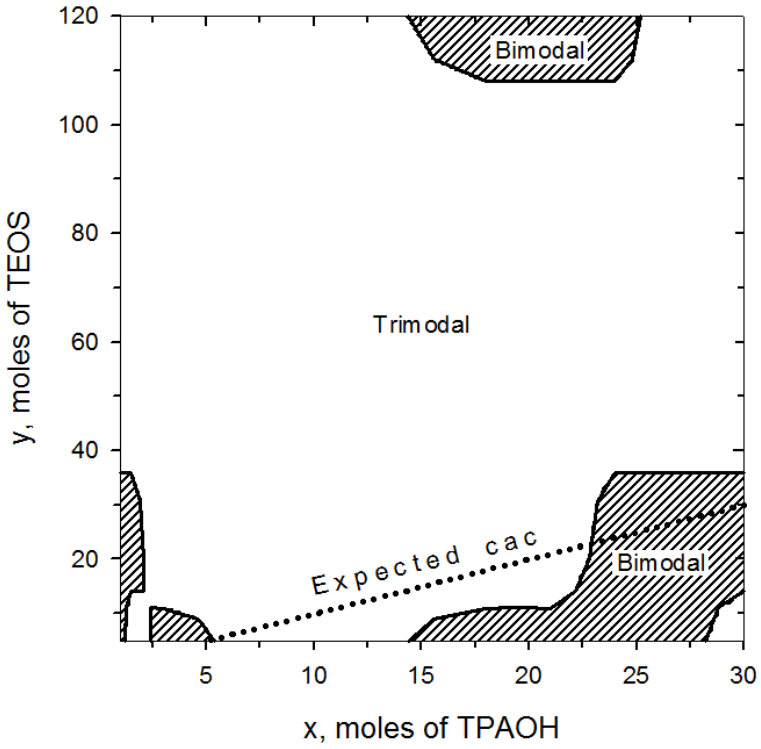

Figure 5.4 Particle size distribution (PSD) mode (i.e., bimodal or trimodal) for precursor mixtures with a molar composition of *x* TPAOH: *y* TEOS: 8100 H_2O.

A diagram of the PSD behavior of mixtures with a molar composition of *x* TPAOH: *y* TEOS: 8100 H_2O (sets S1 to S5) is showed in Figure 5.5. This diagram shows the fraction (based on the intensity of the scattered light) of nanoparticles (x_{NP}), small aggregates (x_{SA}), and big aggregates (x_{BA}) present in a given mixture, being $x_{NP} + x_{SA} + x_{BA} = 1$ the entire population of particles in that mixture. Particle size range and average for each population observed in the PSDs are showed in Table 5.2. The size range of nanoparticles was 1 nm to 100 nm in diameter with an average size of 11 ± 5 nm. The size range of the small aggregates was 100 nm to 1 μm in diameter with an average size of 340 ± 100 nm. Objects larger than 1 μm were considered big aggregates.

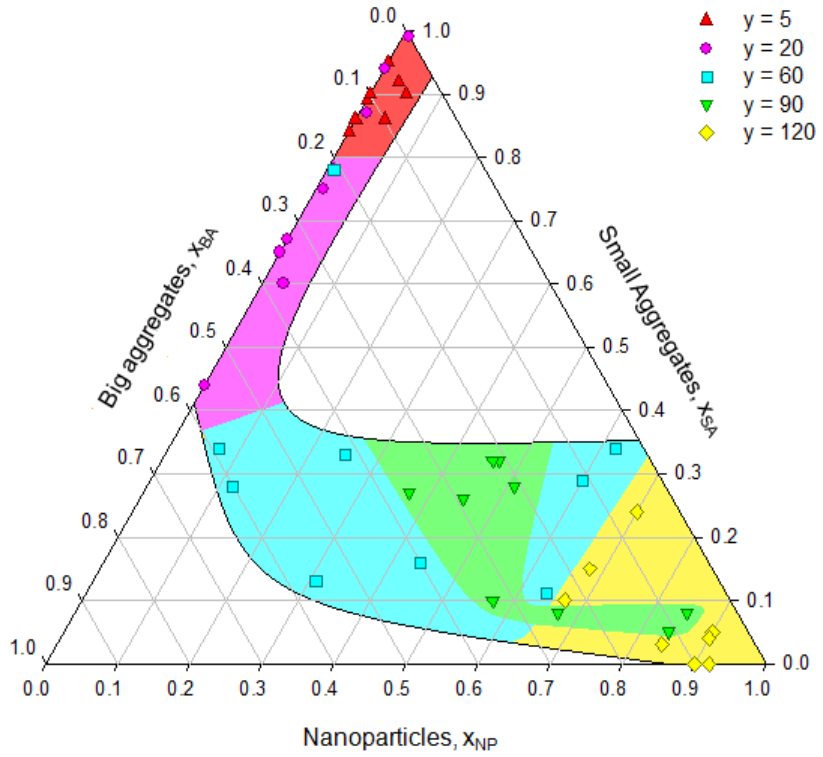

Figure 5.5 Particle size distribution (PSD) for precursor mixtures with a molar composition of *x* TPAOH: *y* TEOS: 8100 H_2O, where *x* was varied from 1 to 30.

Table 5.2 Range and average of particle size for populations observed in PSDs of mixtures from sets S1-S5.

Population	Range, nm	Average, nm
1st population: nanoparticles	1-100	11 ± 5
2nd population: small aggregates	100-1000	340 ± 100
3rd population: big aggregates	>1000	

In Figure 5.5 a clear trend of PSD as a function of the composition of the mixtures can be observed. Thus, mainly small aggregates, some big aggregates, and very few nanoparticles were observed in mixtures with low TEOS contents (y = 5 and y = 20;

red and pink regions, respectively). Larger amounts of nanoparticles with some small aggregates and few big aggregates were observed in the mixtures with high TEOS content (y = 60, y = 90, and y = 120; cyan, green, and yellow regions, respectively). It is important to mark that all the mixtures with compositions below the expected cac were observed in the red and pink regions where small aggregates are predominant. PSDs were not only a function of TEOS concentration but they were also a function of TPAOH concentration.

The size of nanoparticles as a function of TPAOH concentration for precursor mixtures of sets S1 to S5 is shown in Figure 5.6. From this figure two observations can be made. First, increasing TEOS concentration (y) increases, in general, the size of the nanoparticles; however, this increase is not dramatic, and nanoparticles with sizes between 1 and 17 nm in diameter are observed regardless considerable addition of TEOS (from y = 5 to y = 120). Second, for $y \geq 60$, the particle size seems to increase at low TPAOH concentrations, reach a maximum (or stabilize) at medium TPAOH concentrations, and drop at higher TPAOH concentrations. These observations are consistent with previous works, which reported that particles change little in size upon TEOS addition but synthesis mixtures with high pH and/or high TPAOH/TEOS ratios lead to smaller precursor particles.[61] Reduction of particle size with TPAOH addition (and therefore, with increasing pH) can be explained as a charge balance occurring in a nanoparticle with a core-shell structure. Charged silica units increase in the nanoparticle core as pH increases, while TPA cations remain constant in the nanoparticle shell; then, the particle volume should decrease to balance the charge.[61]

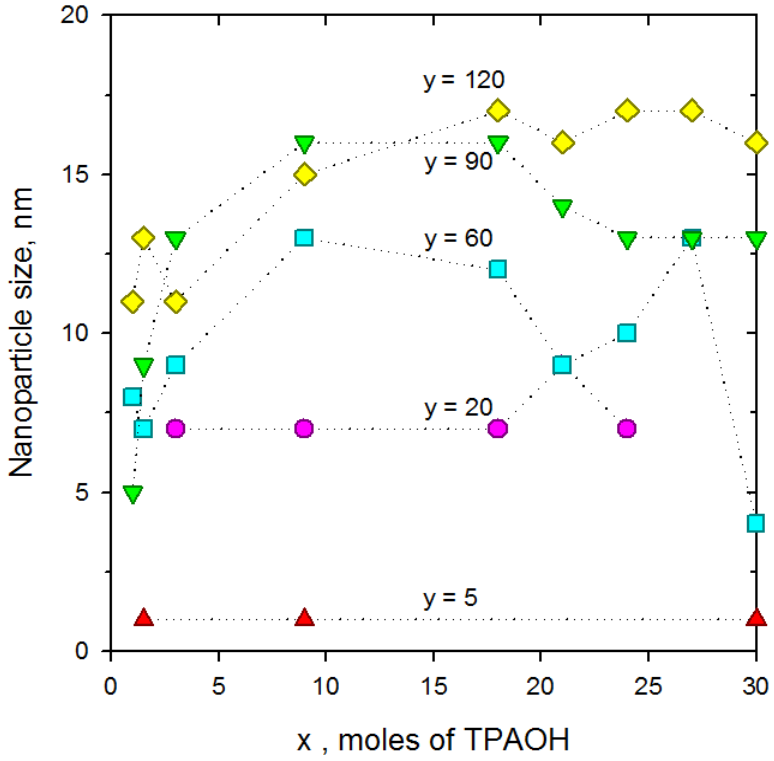

Figure 5.6 Average size of nanoparticles as a function of the TPAOH concentration for precursor mixtures with a molar composition of *x* TPAOH: *y* TEOS: 8100 H_2O.

Figure 5.7 shows a schematic representation of the species that might be coexisting in a precursor mixture of silicalite-1 that has a molar composition above the cac and high water content. The initial mixture (mixture at t = 0 h) contents TPAOH, TEOS and water molecules, but several reactions occur once these molecules start to interact. First, it is expected that TEOS dissolves in the aqueous TPAOH through a hydrolysis reaction, which is relatively fast in systems with high water content and can be described as a single-step irreversible process for systems like the ones studied here with no significant excess of ethanol[80]

$$Si(OEt)_4 + 4H_2O \rightarrow Si(OH)_4 + 4EtOH \qquad (5.1)$$

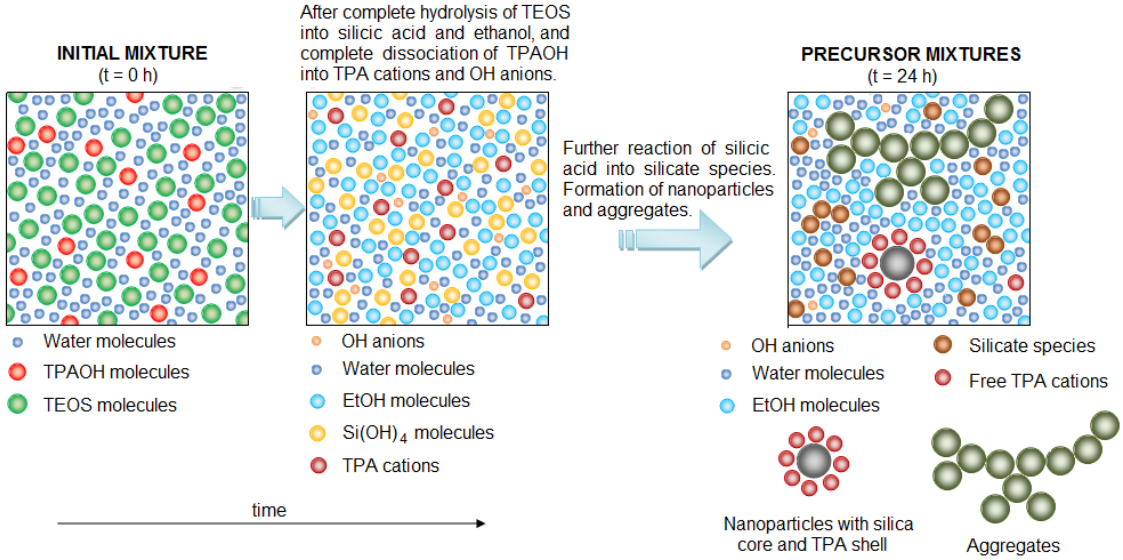

Figure 5.7 Scheme of the species that might be coexisting in a hypothetical precursor mixture of silicalite-1 with a molar composition above the cac.

It is also expected that TPAOH in aqueous mixtures dissociates into TPA cations and OH anions. Thus, it is expected that after a short period of time the mixture contains silicic acid ($Si(OH)_4$), ethanol (EtOH), water, TPA cations, and OH anions. Then, further acid-base reactions take place. Below the cac, monomers are formed by deprotonation of silicic acid, and hydroxide anions (OH^-) are consumed and combined with the silicic-acid-lost-proton to form water[61]

$$Si(OH)_4 + OH^- \rightarrow Si(OH)_3O^- + H_2O \qquad (5.2)$$

This consumption of hydroxide ions can be observed as a significant change in the conductivity and pH values as it was showed in Figures 5.2 and 5.3. Monomers might further combine (condensation reaction) to form oligomers, which also deprotonate to form Q^3 species[61]

$$Si_nO_{(3/2)n}(OH)_n + mOH^- \rightarrow \left(Si_nO_{(3/2)n}(OH)_{n-m}O_m\right)^{m-} + mH_2O \quad (5.3)$$

Additional content of TEOS in the mixture above the cac promotes formation of nanoparticles by the apparent sequester of dissolved silica from the aqueous phase to build blocks of nanoparticles that have a silica core and a TPA shell[61]

$$\begin{aligned} &nSi(OH)_4 + m\left(TPA^+Si(OH)_3O^-\right) \rightarrow \\ &\left(Si_{n+m}O_{3/2(n+m)}(OH)_nO_m\right)^{m-}\left(TPA^+\right)_m + 3/2(n+m)H_2O \end{aligned} \quad (5.4)$$

The removal of dissolved silica from the aqueous phase during the formation of nanoparticles can be observed as a slow decrease in the conductivity and pH values when increasing the TEOS content above the cac.

The formation of nanoparticles with a core-shell structure is depicted on the right side of Figure 5.7. Also, and based on the observations of this investigation, aggregates of silicate species are formed in the precursor mixtures (also depicted in Figure 5.7). However, two important observations about these aggregates have to be pointed out and are described in the next two paragraphs.

First, it is likely that the mixtures contain a small number of aggregates as compared with the number of nanoparticles. Although intensity-weighted PSDs showed a significant amount of aggregates in the mixtures, the intensity-weighted analysis is prone to over predict the number of large objects because they scatter more strongly. Therefore, it is helpful to analyze the data with volume-weighted or number-weighted distributions, which can provide a useful insight about the relatively amount of particles from each population in a given mixture. A comparison between intensity-, volume-, and

number-weighted PSDs is shown in Figure 5.8. Intensity-weighted analysis (solid line) for a mixture with a molar composition of 1 TPAOH: 5 TEOS: 8100 H_2O (Figure 5.8a) shows a very small population of nanoparticles, a large population of small aggregates, and a considerable population of large aggregates. However, a larger population of nanoparticles can be seen in the volume- (dashed line) and number-weighted (dotted line) distributions, although significant populations of aggregates can still be seen in the volume-weighted distribution. Therefore, it can be inferred that the amount of aggregates in this mixture might be smaller than the amount of nanoparticles, but still significant. On the other hand, intensity-, volume-, and number-weighted PSDs for a mixture with a molar composition of 30 TPAOH: 120 TEOS: 8100 H_2O (Figure 5.8b) show a large population of nanoparticles. Thus, it can be inferred that the amount of aggregates in this mixture is not significant since they can only be observed in the intensity-weighted distribution. To conclude this remark, it is important to emphasize that the basic distribution obtained by DLS is intensity weighted and that this distribution is considered more reliable than other weighted distributions because DLS measures fluctuations in the intensity of scattered light rather than volume or number of particles. Other distributions are mathematical transformations of the intensity-weighted distribution and might be affected by the polydispersity of the mixtures.

Second, it is possible that silicate species forming the aggregates are weakly bonded together. If this is the case, these aggregates might not be as stable as the nanoparticles and can easily restructure in such a way that they contribute, together with other dissolved silica species, as building blocks for precursor nanoparticles or as a

source of silica for nanoparticle growth. Thus, it can be expected that after a period of 24 h a precursor mixture contains nanoparticles, few aggregates, silicate species (neutral or charged in the form of monomers, oligomers, etc.) and solvent molecules (i.e., water and ethanol).

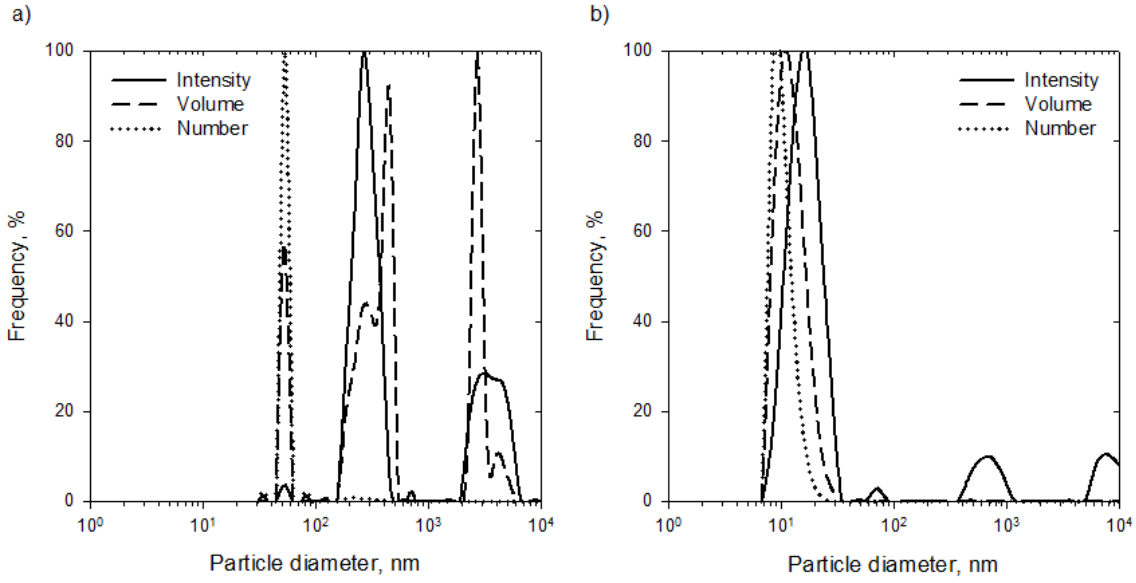

Figure 5.8 Comparison of intensity-, volume-, and number-weighted PSDs for mixtures with a molar composition of a) 1 TPAOH: 5 TEOS: 8100 H_2O and b) 30 TPAOH: 120 TEOS: 8100 H_2O.

5.3.2 'Concentrated' mixtures

In this section results for mixtures of sets S8 to S10 are discussed. The conductivity of precursor mixtures with a molar composition of *x* TPAOH: *y* TEOS: *z* H_2O (sets S8 and S9) as a function of the TPAOH/TEOS (*x*/*y*) ratio is shown in Figure 5.9. A fairly linear increase in the conductivity is observed at low *x*/*y* ratios, while the convergence towards a plateau is observed at high *x*/*y* ratios. This trend is consistent with previous works.[61] Moreover, it can be observed that the conductivity is very similar

for mixtures with z = 200 (set S8) and those with z = 300 (set S9). However, the conductivity is slightly but consistently higher (up ~ 20 % for x/y ~ 0.3 - 0.6) in mixtures with high water content (z = 300). The origin of higher conductivities for more dilute mixtures with z = 300 is unclear at this point. It is important to point out that the mixture of set S8 with x/y = 0.10 was transparent, but very viscous and with a gel-like appearance. Addition of TPAOH to the subsequent mixtures of set S8 promoted the dissolution of the gel phase, in such a way that the mixtures with $x/y \geq 0.34$ had a liquid-like appearance.

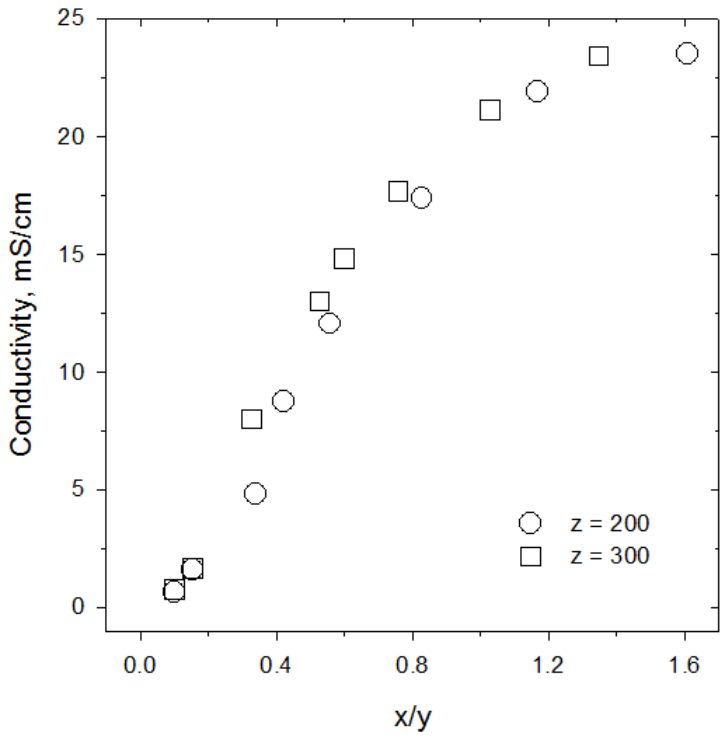

Figure 5.9 Conductivity as a function of the TPAOH/TEOS molar ratio for precursor mixtures with a molar composition of x TPAOH: y TEOS: z H_2O.

The pH of precursor mixtures with a molar composition of x TPAOH: y TEOS: z H_2O (sets S8 and S9) as a function of the TPAOH/TEOS (x/y) ratio is shown in Figure

5.10. In general, larger pH values are observed for samples with lower water contents (z = 200, set S8). This behavior is expected since the concentration of hydroxide ions (which is proportional to the pH) is larger in samples with lower contents of water.

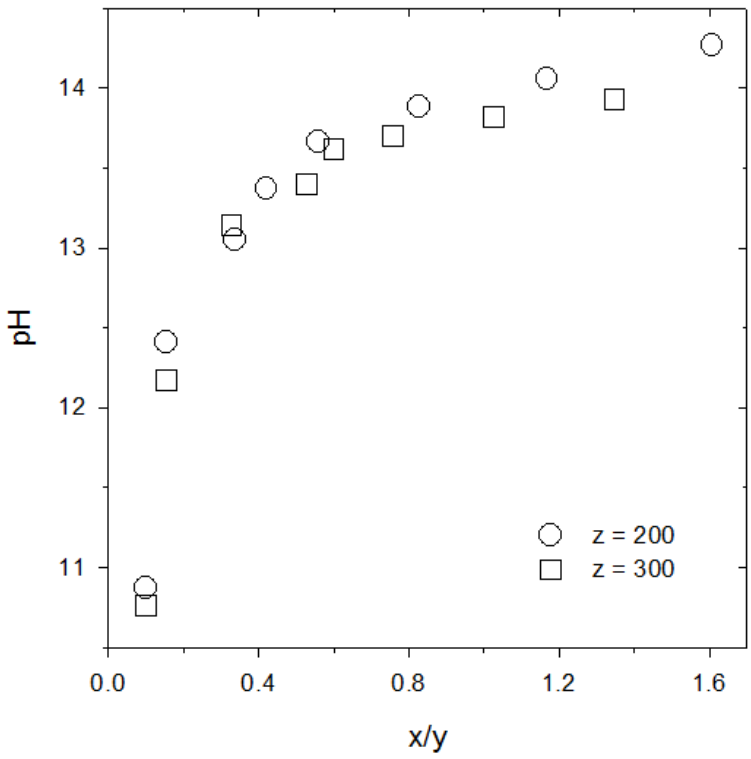

Figure 5.10 pH as a function of the TPAOH/TEOS molar ratio for precursor mixtures with a molar composition of x TPAOH: y TEOS: z H_2O

Figure 5.11 displays the particle size distribution mode of precursor mixtures with a molar composition of x TPAOH: y TEOS: z H_2O (sets S8-S10) as a function of the TPAOH/TEOS (x/y) ratio. No clear trends in the PSD mode are observed as a function of x/y, but most of the mixtures showed trimodal and/or tetramodal distributions. The exception to this behavior are mixtures of set S10 with x/y = 0.04, 0.06, and 0.12, which showed unimodal or bimodal distributions with populations of

small and/or big aggregates. However, it is important to point out that a gel-like solid was formed on top of these mixtures, and that only the liquid on the bottom was tested using DLS. Interestingly, and in contrast with the single population of nanoparticles observed in 'dilute' mixtures, the rest of the mixtures of sets S8 to S10 show two populations of particles with relatively small diameters (referred in Table 5.3 as small and big nanoparticles). This observation is consistent with results reported in previous studies of precursor mixtures.[65,159] The range and average of particle size are showed in Table 5.3 for each population observed in the PSDs. Small nanoparticles have a size range of 1 to 10 nm in diameter with an average size of 2 ± 1 nm, big nanoparticles have a size range of 10 to 100 nm in diameter with an average size of 30 ± 20 nm, and small aggregates have a size range of 100 nm to 1 μm in diameter with an average size of 350 ± 180 nm. Objects larger than 1 μm are considered big aggregates.

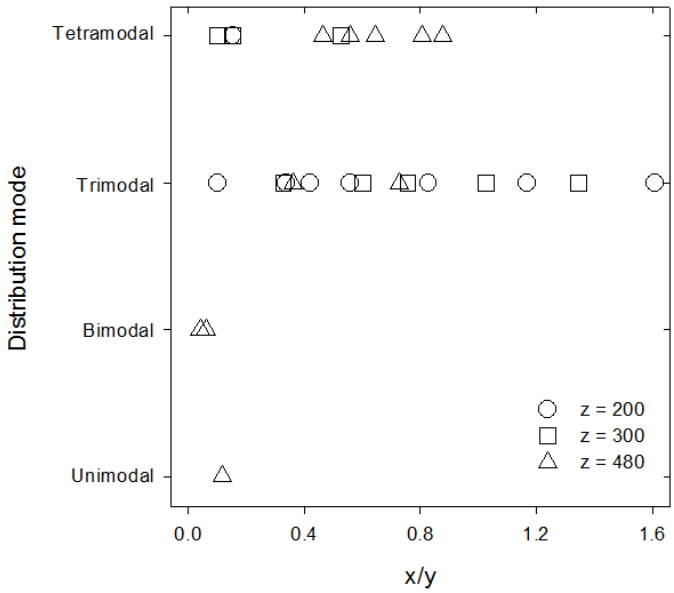

Figure 5.11 Particle size distribution mode as a function of the TPAOH/TEOS molar ratio for precursor mixtures with a molar composition of *x* TPAOH: *y* TEOS: *z* H_2O.

Table 5.3 Range and average of particle size for populations observed in PSDs of mixtures from sets S8-S10.

Population	Range, nm	Average, nm
1st population: small nanoparticles	1-10	2 ± 1
2nd population: big nanoparticles	10-100	30 ± 20
3rd population: small aggregates	100-1000	350 ± 180
4th population: big aggregates	>1000	

A diagram of the PSD behavior of mixtures with a molar composition of *x* TPAOH: *y* TEOS: *z* H_2O (sets S8-S10) is showed in Figure 5.12. This diagram shows the fraction of small nanoparticles (x_{SNP}), big nanoparticles (x_{BNP}), and aggregates (x_A). The fraction of aggregates includes both, small and big aggregates. The trends in PSD of 'concentrated' mixtures are not as clear as the trends observed for 'dilute' mixtures. However, larger fraction of aggregates can be observed in the 'concentrated' mixtures with the highest content of water (z = 480); but again, it is worthy to point out that the intensity-weighted PSDs used to generate the diagram of Figure 5.12 are prone to over predict the amount of large particles in the mixtures. Even so, the observation of larger fractions of aggregates at higher water contents is consistent with the results for 'dilute' mixtures. Therefore, it is possible that increasing water in these mixtures promotes the formation of aggregates, which can be the result of a surface tension effect.

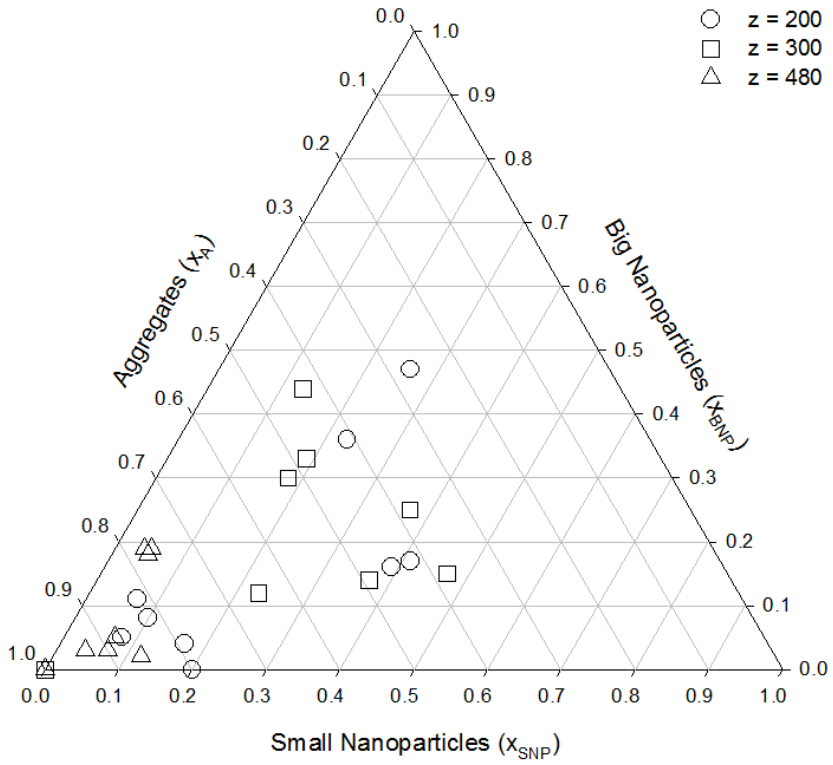

Figure 5.12 Particle size distribution (PSD) behavior for precursor mixtures with a molar composition of *x* TPAOH: *y* TEOS: *z* H_2O (sets S8-S10).

The size of small and big nanoparticles as a function of the TPAOH/ TEOS (*x*/*y*) ratio for precursor mixtures with a molar composition of *x* TPAOH: *y* TEOS: *z* H_2O (sets S8-S10) is shown in Figure 5.13. In contrast with 'dilute' mixtures, the size of the nanoparticles does not show any dependency on the *x*/*y* ratio. All the mixtures of sets S8-S10 show sizes between 1-3 nm in diameter for the population of small nanoparticles regardless their content of TPAOH and TEOS (Figure 5.13a). Most of the mixtures of sets S8-S10, especially those with *z* = 480, show sizes of approximately 20 nm in diameter for the second population of big nanoparticles (Figure 5.13b).

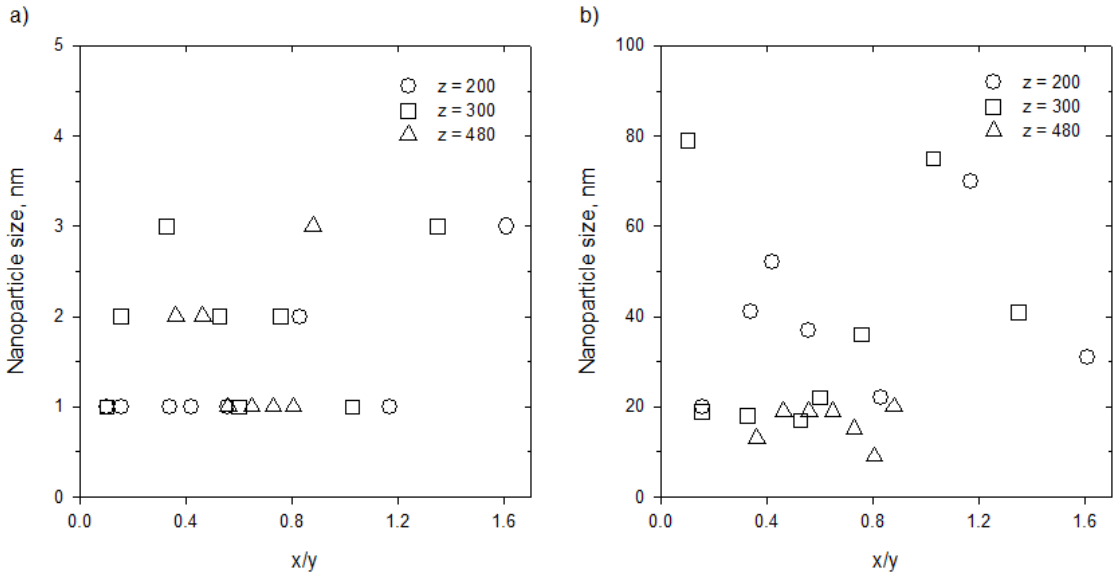

Figure 5.13 Average size of a) small and b) big nanoparticles as a function of the TPAOH/TEOS molar ratio for precursor mixtures with a molar composition of *x* TPAOH: *y* TEOS: *z* H_2O (sets S8-S10).

5.4 Conclusions

Important results on the nucleation and growth of silicalite-1 precursor mixtures have been reported in previous investigations. However, these investigations have been conducted on mixtures with different compositions, which complicate the comparison among results. Therefore, the main goal of this investigation is to provide a way to unify these findings by means of the investigation of the composition effect on the phase behavior of these silicalite-1 precursor mixtures. Thus, a broad range of compositions for 'dilute' and 'concentrated' mixtures has been studied in this investigation. Specifically, the effect of the composition on the conductivity, pH, and particle size distribution (PSD) of the mixtures was studied. Both 'dilute' and 'concentrated' mixtures, show a rapid decrease on the conductivity and pH at low concentration of TEOS and a slow

decrease at high concentration of TEOS. This observation is consistent with the regions above and below the critical aggregation concentration (cac) reported in previous works. Trimodal PSDs with nanoparticles (~ 10 nm in diameter), small aggregates (~ 340 nm in diameter), and big aggregates (> 1 μm in diameter), are observed in most of the 'dilute' mixtures. Moreover, PSDs present a dependence on the mixture composition, showing more nanoparticles at higher TEOS concentration and smaller nanoparticle sizes at higher TPAOH concentration. On the other hand, 'concentrated' mixtures did not show a clear dependence of PSD on mixture composition. However, and in contrast with 'dilute' mixtures, most of the 'concentrated' mixtures show trimodal or tetramodal distributions with populations consisting of small nanoparticles (~ 2 nm in diameter), big nanoparticles (~ 30 nm in diameter), small aggregates (~ 350 nm in diameter), and big aggregates (> 1 μm in diameter). Thus, 'concentrated' mixtures seem to be more complex than 'dilute' ones, and more interactions among species must be expected to occur in these mixtures due to their relatively high concentration. In conclusion, the investigation presented in this chapter shows that composition affects the phase behavior of silicalite-1 precursor mixtures. This fact should be considered when comparing previous findings reported in the literature since the behavior of PSD in precursor mixtures might affect the rate of crystallization of the final zeolite phase. It is expected that the information presented in this chapter helps to unify previous findings on silicalite-1 nucleation and growth by providing a better understanding of the composition effect in precursor mixtures.

CHAPTER VI

SUMMARY AND CONCLUSIONS

The investigation presented in this dissertation was conducted in order to determine the strength of organic-inorganic interactions in transparent synthesis mixtures using PFG NMR spectroscopy. The synthesis of silicalite-1 was chosen for this investigation as a model system because of its robustness, chemical simplicity, versatility to form MFI under a wide range of conditions, and suitability to be studied using different experimental techniques. The approach presented in this dissertation used experimental data of the organocation self-diffusion coefficients obtained with PFG NMR in order to determine the strength of the organocation-silica interactions in silicalite-1 synthesis mixtures. In this chapter, the findings of this investigation are summarized and the conclusion of this research is presented.

6.1 Summary of findings

Three main tasks were conducted in order to achieve the objective of this investigation and were presented in Chapters III, IV, and V. The findings of these tasks are summarized as follows.

6.1.1 Findings of the investigation of the organocation role in precursor mixtures of silicalite-1

An investigation of organocation-TEOS-water mixtures containing organocations that resemble the TPA cation structure (i.e., TPA mimics) was presented in Chapter III. The particular objective of this first investigation was to determine how the identity of

the organocation affects the strength of the organocation-silica interactions. The outcome of this investigation was expected to give some insights of the role of the organocation in the silicalite-1 nucleation and growth.

The findings showed that PFG NMR is uniquely suited to determine in a non-invasive way the adsorption strength of the organocation to the silica nanoparticles. The diffusion NMR results indicated that the adsorption Gibbs energies of MTPA and ETPA cations (i.e., the two organocations with TPA mimics) are quite similar to the adsorption Gibbs energy of TPA cation. This finding is quite interesting, as previous work showed that the TPA mimics studied here lead to dramatically different rates of silicalite-1 growth as compared to the TPA cation.[44] In particular, the previous work showed that MTPA cations lead to growth rates ~50% slower than those of TPA cation. Thus, it can be concluded from this investigation that small changes in the Gibbs energy of the organanocation adsorption over the silica nanoparticles lead to large changes in both the stability of these precursor particles and the rate of silicalite-1 formation.

6.1.2 Findings of the in situ PFG NMR investigation of silicalite-1 synthesis mixtures

An in situ PFG NMR investigation of the silicalite-1 synthesis from TPAOH-TEOS-water mixtures was presented in Chapter IV. The particular objective of this second investigation was to determine whether or not the organocation self-diffusion coefficients can be measured at temperatures near to the actual synthesis temperature using in situ PFG NMR measurements. The findings of this investigation were expected to provide information about the strength of the organocation-silica interactions at the

synthesis temperature and how these values compare with those acquired at 25°C. Also, the diffusion results were expected to give some insight of the time evolution of the silicalite-1 formation at the synthesis conditions.

The findings presented in Chapter IV showed that in situ PFG NMR is a feasible technique to determine the organocation self-diffusion coefficients at synthesis temperatures. The results showed similar adsorption Gibbs energies for the TPAOH-TEOS-water mixtures at 70°C and 25°C. However, the adsorption data at 70°C did not fit the Langmuir isotherm as well as the data at 25°C did. The larger deviations at 70°C were ascribed to assumptions in the Langmuir isotherm that might not apply at higher temperatures. Therefore, the Freundlich isotherm that considers heterogeneous sites to some extent was used and showed a better fit of the adsorption data at 70°C.

The time evolution of the silicalite-1 synthesis was also monitored via PFG NMR. Single-pulse ^{1}H standard NMR experiments did not show dramatic differences in the spectra during the heating period. However, the diffusion coefficients obtained with PFG NMR remained almost constant at the beginning of the synthesis, increased when the samples became turbid, reached a maximum during the exothermic-endothermic transition, and trended towards a plateau at the end of the synthesis. Thus, it can be concluded from this investigation that in situ PFG NMR allows determining the strength of the organocation-silica interactions at the synthesis conditions and monitoring the time evolution of the mixtures during the silicalite-1 crystallization.

6.1.3 Findings of the systematic investigation of silicalite-1 precursor mixtures with varying degrees of dilution

A systematic investigation of TPAOH-TEOS-water precursor mixtures with a broad range of compositions was presented in Chapter V. Given that previous investigations of silicalite-1 nucleation and growth were conducted on mixtures with basically randomly selected compositions, the particular objective of this third investigation was to determine whether or not the composition affects the phase behavior of the precursor mixtures. The findings of this investigation were expected to unify previous findings by showing similarities or differences in the phase behavior of these precursor mixtures as a function of the composition.

Findings for 'dilute' and 'concentrated' mixtures showed a rapid decrease on the conductivity and pH at low concentration of TEOS and a slow decrease at high concentration of TEOS. This observation was consistent with the regions above and below the critical aggregation concentration (cac) reported in previous works.[61] Most of the 'dilute' mixtures showed trimodal PSDs with populations consisting of nanoparticles (~ 10 nm in diameter), small aggregates (~ 340 nm in diameter), and big aggregates (> 1 μm in diameter). Also, the PSDs showed a dependence on the mixture composition, with more nanoparticles at higher TEOS concentration and smaller nanoparticle sizes at higher TPAOH concentration. The 'concentrated' mixtures did not show a clear dependence of the PSD on the mixture composition. However, most of the 'concentrated' mixtures showed trimodal or tetramodal distributions with populations consisting of small nanoparticles (~ 2 nm in diameter), big nanoparticles (~ 30 nm in

diameter), small aggregates (~ 350 nm in diameter), and big aggregates (> 1 μm in diameter). Thus, 'concentrated' mixtures seemed to be more complex than 'dilute' ones, and more interactions among species must be expected to occur in these mixtures due to their relatively high concentration.

In conclusion, this investigation showed that the composition affects the phase behavior of silicalite-1 precursor mixtures. This fact should be considered when comparing previous findings reported in the literature since the behavior of PSD in precursor mixtures might affect the rate of crystallization of the final zeolite phase.

6.2 Conclusions

The main conclusion of this research is that the strength of the organic-inorganic interactions in transparent synthesis mixtures can be determined from experimental data of the organocation self-diffusion coefficients obtained with PFG NMR spectroscopy.

The following specific conclusions can be made from the results described in this dissertation:

- Small changes in the Gibbs energy of the organocation adsorption over the silica nanoparticles lead to large changes in both the stability of the precursor particles and the rate of silicalite-1 formation.
- The strength of the organocation-silica interactions at the synthesis conditions can be determined using in situ PFG NMR. Therefore, the time evolution of the silicalite-1 crystallization can be monitored.

- The adsorption Gibbs energies are similar at 25°C and 70°C. The exothermic-endothermic transition occurring during the silicalite-1 synthesis is associated with a maximum in the organocation diffusion coefficients.
- The composition of the silicalite-1 precursor mixtures affects their PSD. Therefore, the composition should be considered when comparing previous findings reported in the literature for mixtures with different compositions.

CHAPTER VII

RECOMMENDATIONS FOR FUTURE INVESTIGATIONS

7.1 Implication of the current research for the zeolite synthesis

Prior to the research presented in this dissertation only *structural* information about the morphology of the species involved in the zeolite synthesis was available. The research presented here provided *chemical* information about the strength of the organic-inorganic interactions occurring during the zeolite formation. Determining this *chemical* information has one important implication for zeolite synthesis, which is helping to understand better the nucleation and growth process of zeolites. This better understanding of zeolite crystallization is required for the development of a detailed molecular-level description of this process. Such a description is needed in order to generate predictive models of zeolite formation that allow the control of zeolite properties and the rational design of new zeolite synthesis. In a broader scope, this predictive model would represent a pinnacle achievement in zeolite science that would allow the emergence of a new generation of materials by design.

7.2 Recommendations for future research

Although the main objective of this research of determining the strength of organic-inorganic interactions with PFG NMR was satisfied, more research has to be conducted in order to achieve the ultimate objective of the investigations of zeolite nucleation and growth that is the generation of a predictive model for the rational synthesis of zeolites. Therefore, several recommendations for future research are

proposed based on the findings of this investigation and are presented in the next sections of this chapter.

7.2.1 Study of zeolite A synthesis

In order to generalize the results presented in this dissertation, it is recommended to investigate the nucleation and growth of other zeolites using the same approach presented in this work. Although silicalite-1 synthesis has been chosen as a model synthesis due to its favorable attributes, previous studies have shown that the silicalite-1 crystallization mechanism is not representative of the entire group of zeolites.[45] Moreover, the following limitations of the silicalite-1 synthesis reported in previous works[184] have to be considered:

- Pure-silica zeolites as silicalite-1 represent only a small fraction of all the possible zeolite structures.
- With exception of MFI and MEL framework types, the growth of pure-silica zeolites is difficult because their syntheses usually require large complex SDAs and/or fluoride media, long crystallization times (e.g., up to several weeks at 150-175°C), multiple silica sources (e.g., fumed silica, silica gel, or colloidal silica) as in MTW synthesis, and sometimes high temperatures (i.e., temperatures higher than 150-175°C).
- The use of pure-silica zeolites in a large-scale is impractical due to the cost of SDAs.

- The effect of heteroatom substitution involved in most of the zeolite frameworks cannot be studied from the synthesis of silicalite-1 because this zeolite does not contain heteroatoms.

Thus, it is recommended to investigate zeolite A syntheses with PFG NMR in order to determine the strength of organic-inorganic interactions. As mentioned in Chapter I, the nucleation and growth of zeolite A (LTA) has been previously studied by Mintova et al. with HRTEM and DLS.[40] In that study, the morphology and evolution of the zeolite A formation is reported. Therefore, it is suggested to follow the same synthesis procedure in order to investigate the organic-inorganic interactions during the zeolite A synthesis.

Three main steps are proposed for the study of the zeolite A synthesis: 1) determine the effect of the aging and heating periods on the final zeolite A structure using PXRD; 2) monitor the PSD of the mixtures during the synthesis by DLS; and 3) determine the strength of organic-inorganic interactions and monitor the time evolution of zeolite A using NMR spectroscopy.

The first step is proposed because the synthesis of zeolite A seems to be sensitive to the duration of the aging and heating periods. A preliminary investigation of the effect of these experimental parameters on the final structure of zeolite A was conducted. Seven zeolite A synthesis mixtures were investigated. The information of the aging time, heating time, and composition of these mixtures is summarized in Table 7.1. The aging was performed at room temperature, while a constant temperature of 70°C was used during the heating.

Table 7.1 Aging time, heating time, and composition for zeolite A synthesis mixtures.

Mixture ID	Aging time, days	Heating time, days	Composition
ZA1	7	0	0.3 Na_2O: 11.25 SiO_2: 1.8 Al_2O3: 13.4 $(TMA)_2O$: 700 H_2O
ZA2	7	2	**0.35** Na_2O: 11.25 SiO_2: 1.8 Al_2O3: 13.4 $(TMA)_2O$: 700 H_2O
ZA3	7	2	0.3 Na_2O: 11.25 SiO_2: 1.8 Al_2O3: 13.4 $(TMA)_2O$: 700 H_2O
ZA4	7	2	0.3 Na_2O: 11.25 SiO_2: 1.8 Al_2O3: 13.4 $(TMA)_2O$: **710 H_2O**
ZA5	7	5	0.3 Na_2O: 11.25 SiO_2: 1.8 Al_2O3: 13.4 $(TMA)_2O$: 700 H_2O
ZA6	10	2	0.3 Na_2O: 11.25 SiO_2: 1.8 Al_2O3: 13.4 $(TMA)_2O$: 700 H_2O
ZA7	10	18	0.3 Na_2O: 11.25 SiO_2: 1.8 Al_2O3: 13.4 $(TMA)_2O$: 700 H_2O

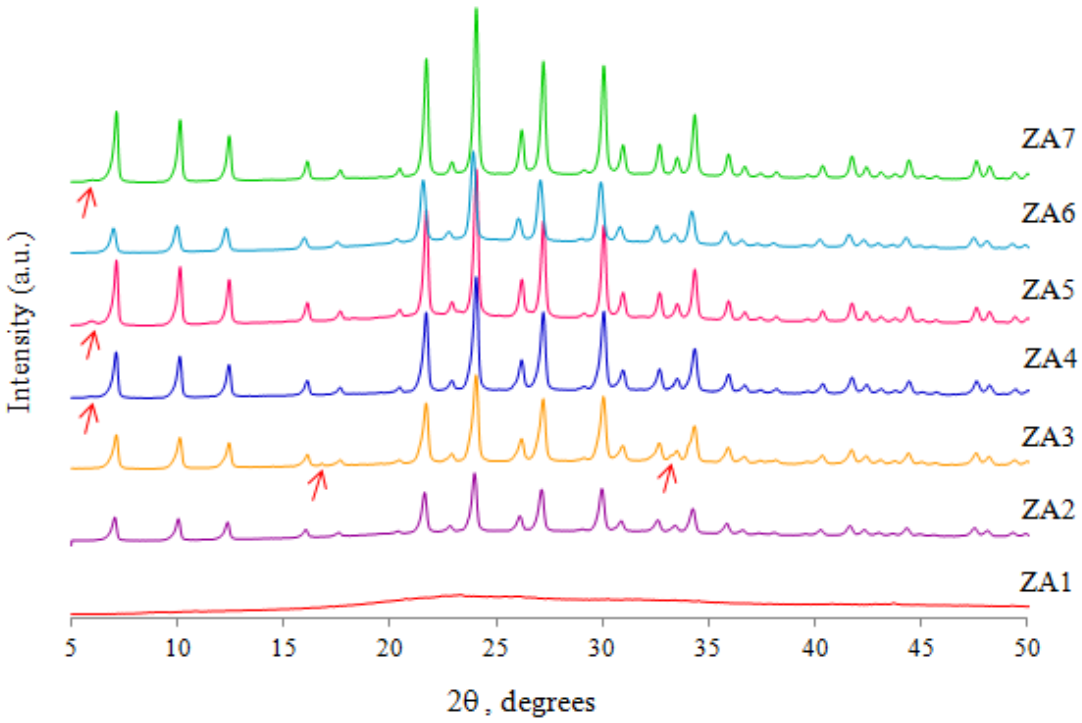

Figure 7.1 PXRD patterns of the zeolite A synthesis mixtures described in Table 7.1 as a function of the aging time, heating time, and composition.

The PXRD patterns of the mixtures described in Table 7.1 are shown in Figure 7.1. The PXRD patterns show that zeolite A was formed from all the synthesis mixtures that were heated for at least 2 days (i.e., mixtures ZA2 to ZA7). Also, the intensity of the peak patterns seems to increase with the aging and heating time, which has been associated with larger thicknesses of the tested samples. It is important to point out that very small amounts of powder were obtained from each synthesis and that all the powder obtained was tested by PXRD. The red arrows in Figure 7.1 point to small peaks that do not belong to the LTA standard pattern. Although other zeolite phases can be formed by varying the conditions of zeolite A synthesis, the peaks identified with the red arrows have not been associated with other zeolite phases. These peaks, however, have been attributed to subtle distortions in the zeolite framework caused by the changes in the synthesis conditions or in the post-synthesis treatment (i.e., collection of the solids).[18] These changes can reduce the symmetry of the material and produce more peaks in the pattern.

The second step proposed for the investigation of the zeolite A synthesis is monitoring the PSD of the mixtures. In Figure 7.2 some preliminary results of PSD are shown for mixture ZA4. As described in Table 7.1, mixture ZA4 was aged at room temperature during 7 days and heated at 70°C during 5 days after the aging period. The PSD results show that two populations of particles are present at the beginning of the synthesis: one of approximately 40 nm in diameter and the other bigger than 1 μm in diameter. The first population is consistent with the work of Mintova et al. that reported the presence of aggregates in the size range of 40 to 80 nm at the beginning of the

synthesis.[40] The PSDs of Figure 7.2 also show that after 3 days of aging at room temperature another two very small populations can be observed: one in the range of 1 to 2 nm, and the other of approximately 200 nm. Moreover, some distortion of the population with the biggest particle size is observed. These changes in the PSD coincide in time with the observations of Mintova et al.[40] They reported the "birth" of small zeolite A crystallites (10-30 nm in diameter) embedded in amorphous gel aggregates (~30-60 nm) after 3 days of aging at room temperature.

During the remaining aging period, the PSDs showed in Figure 7.2 stay fairly constant displaying at all the times the population with particle size of approximately 40 nm (blue dotted line). Only some changes in the population with the bigger particle size (> 1 μm) are observed. For this remaining aging period Mintova et al. reported that zeolite A crystallites grow at the expense of the surrounding amorphous agglomerates and that crystalline particles of ~40 to 80 nm are formed after 7 days at room temperature.[40] Of course, DLS is not capable to distinguish between amorphous and crystalline phases, and their conclusions were based on their HRTEM and XRD studies.

In Figure 7.1 it can be observed that heating the mixture at 70°C for 1 day perturbs the PSD and that further heating promotes the PSD stabilization displaying a population with particle size of approximately 200 nm. This value is also in agreement with the values observed by Mintova et al. after 10 days of aging at room temperature and 2 days of heating at 80°C.[40] However, a better comparison between the PSD results with the results of the investigation of Mintova et al can be made by analyzing mixture ZA6 that uses the same aging and heating periods than that work.

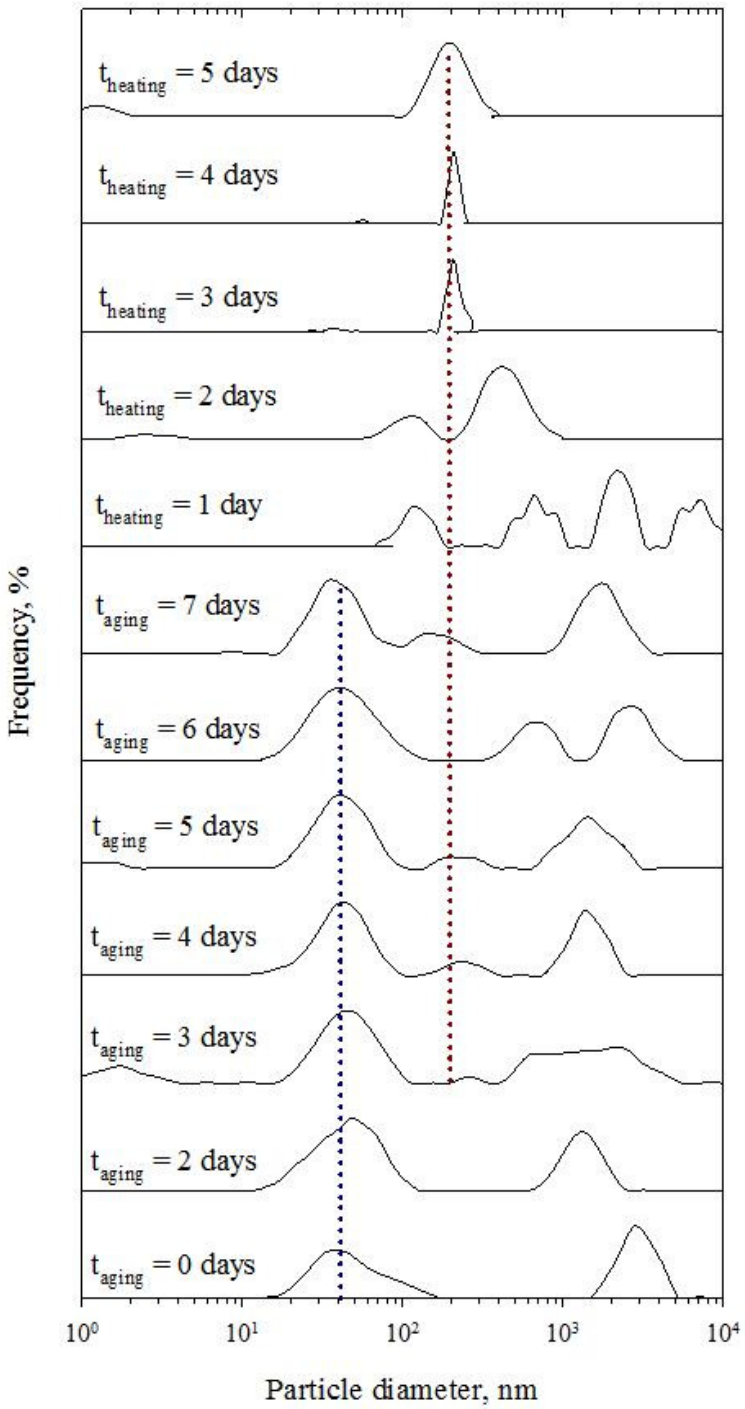

Figure 7.2 NNLS particle size distributions for the synthesis mixture ZA4. The PSDs are weighted by intensity and the maximum frequency of each distribution is 100%.

Finally, for the third step of the zeolite A investigation two recommendations are made. First, it is suggested to monitor with single-pulse ^{1}H NMR and PFG NMR measurements the time evolution of the self-diffusion coefficients of the organocation (TMA cation) in the mixture ZA6 at the synthesis conditions (i.e. at 25°C during 10 days of aging and at 70°C during 2 days of heating). The time evolution of the signal intensity and self-diffusion coefficients of the organocation can be analyzed and compared with the formation mechanism proposed by Mintova et al.[40] Second, it is recommended to vary the organocation content in order to determine the strength of the organic-inorganic interactions at different stages of the zeolite A synthesis. However, it has to be considered that varying the organocation content might change the final phase obtained from the synthesis.

7.2.2 Study of the organocation role of non-TPA mimics

The investigation presented in Chapter III was conducted in order to understand the role of the organocation in the silicalite-1 synthesis. In that investigation organocations with a similar molecular structure to that of the TPA cation were studied. Thus, it was possible to ascribe differences in the strength of the organocation-silica interactions to the organocation identity. However, it is recommended to study the role of other organocations in transparent synthesis mixtures in order to extend the findings of that investigation to more complex systems. Therefore, it is proposed the study of the role of 4,4'-trimethylenebis (1,1'-dimethylpiperidinium) (TMBDMP) and N,N,N-trimethyl-1-adamantylammonium (TMAA). The former is a selective cation that can lead to the formation of ZMS-12, but not from optically transparent mixtures.[46] The

latter is a highly non-selective cation whose zeolite phases depend on the synthesis conditions. Also, the molecular structure of these organocations is quite different to the one of the TPA cation. Preliminary results show that the free diffusion coefficients of the TMAA and TMBDMP cations are significantly different to the diffusion coefficients of the TPA and TPA-mimics cations (Figure 7.3). Therefore, a different behavior of their diffusion coefficients is expected in the presence of silica. The diffusion coefficients of the TMBDMP cation as a function of the organocation concentration are shown in Figure 7.4 for a mixture containing a silica source (TEOS). The trend observed in this figure is quite different to the trends observed for the TPA cations, but further study of this cation is needed in order to understand these systems.

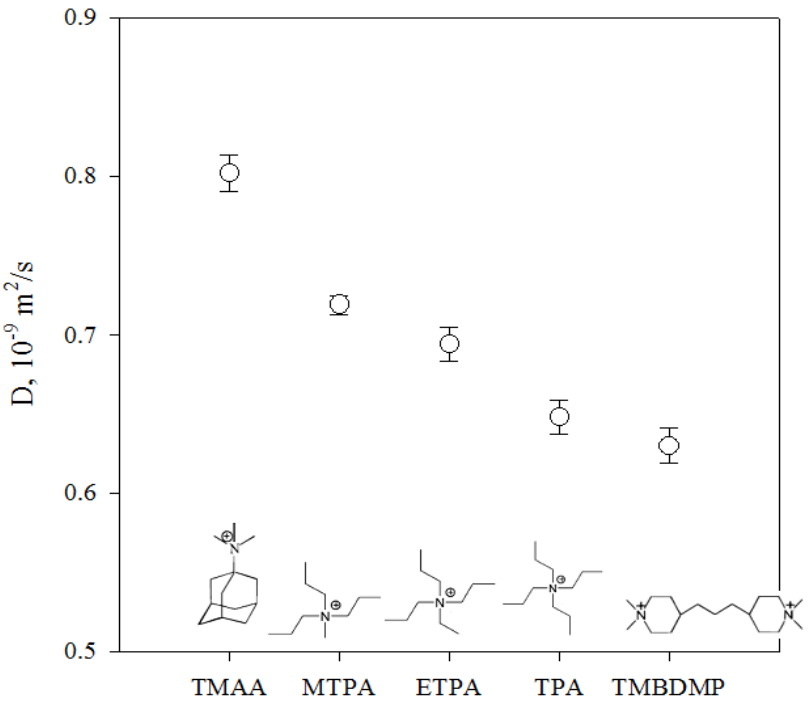

Figure 7.3 Diffusion coefficients of different organocation at 25°C in mixtures with a molar composition of *x* cation: 7290 H_2O: 810 D_2O.

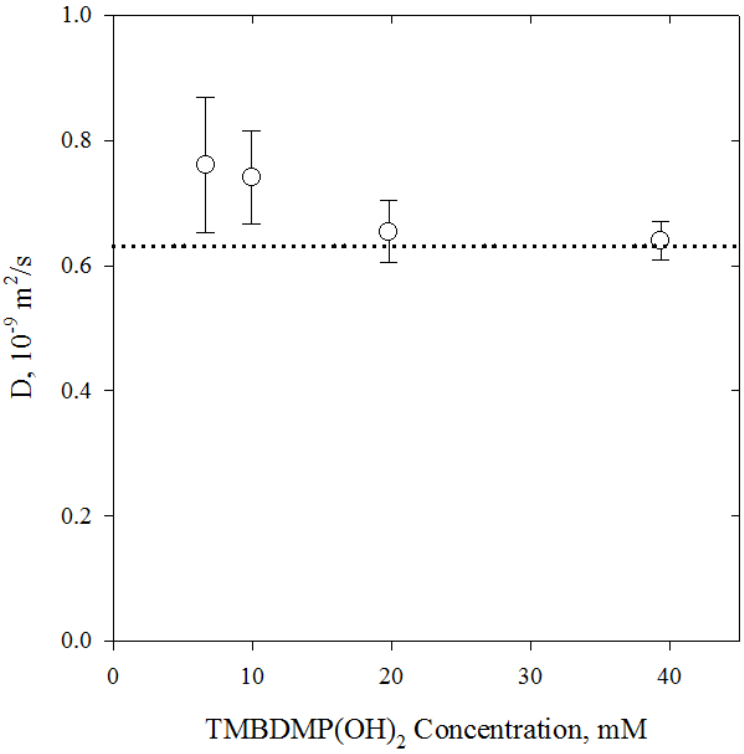

Figure 7.4 Diffusion coefficients of TMBDMP cation as a function of the total $TMBDMP(OH)_2$ concentration for mixtures with a molar composition of *x* $TMBDMP(OH)_2$: 20 TEOS: 7290 H_2O: 810 D_2O at 25°C. The free diffusion coefficient of the TMBDMP cation is indicated with the dotted line.

7.2.3 Other recommendations

In Chapter I many important parameters involved in the zeolite synthesis were described. These parameters include composition, Si and Al sources, Si/Al ratio, pH, water content, SDAs, solvents, aging, stirring, temperature, and time. It is suggested the use of design of experiments (DOE) for future research because this systematic approach will allow planning structured experiments where specific changes in the input variables are made in order to analyze the effects in the output variables. DOE offers a more effective approach than the "one change at a time" testing.[185] It allows planning for all

possible dependencies among variables at the first place, and then prescribes what data are needed to assess them. Therefore, it maximizes the information gained with the experiments since the effect of more than one parameter and the interactions among parameters can be tested at the same time. The use of this statistical tool is strongly recommended for the design of future experiments, given the large number of parameters involved in this complex problem of zeolite nucleation and growth.

REFERENCES

1. Kozo, I.; Sridhar, K.; Makoto, N., *Porous Materials. Process Technology and Applications*. Kluwer Academic Publishers: Dordrecht, **1998**.

2. Cundy, C. S.; Cox, P. A., *Chemical Reviews* **2003,** *103* (3), 663-702.

3. van Bekkum, H.; Flanigen, E. M.; Jacobs, P. A.; Jansen, J. C., *Introduction to Zeolite Science and Practice*. Elsevier: Amsterdam, **2001**.

4. Wong, T. W., *Handbook of Zeolites: Structure, Properties and Applications*. Nova Science Publishers: New York, **2009**.

5. Salazar, K.; McNutt, M. K., *Mineral Commodity Summaries 2011*. U.S. Geological Survey: Washington, **2011**.

6. Dyer, A., *An Introduction to Zeolite Molecular Sieves*. John Wiley & Sons: Chichester, **1998**.

7. Cejka, J.; van Bekkum, H.; Corma, A.; Schuth, F., *Introduction to Zeolite Science and Practice*. Elsevier: Amsterdam; Boston; Heidelberg, **2007**.

8. Baerlocher, C.; McCusker, L. B., *Database of Zeolite Structures*. http://www.iza-structure.org/databases (accessed August **2011**).

9. Kanellopoulos, N. K., *Nanoporous Materials: Advanced Techniques for Characterization, Modeling, and Processing*. CRC Press: London, **2011**.

10. Corma, A.; Rey, F.; Rius, J.; Sabater, M. J.; Valencia, S., *Nature* **2004,** *431* (7006), 287-290.

11. Breck, D. W., *Zeolite Molecular Sieves. Structure, Chemistry, and Use*. John Wiley & Sons: New York, **1974**.

12. Kühl, G., *Microporous and Mesoporous Materials* **1998,** *22* (4-6), 515-516.

13. Mintova, S.; Valtchev, V., *Microporous and Mesoporous Materials* **2002,** *55* (2), 171-179.

14. Meise, W.; Schwochow F, E., Kinetic Studies on the Formation of Zeolite A. In *Molecular Sieves*, Meier, W. M.; Uytterhoeven, J. B., Eds. American Chemical Society: Bayer AG, **1973**, Vol. 121, 169-178.

15. Lu, B.; Tsuda, T.; Sasaki, H.; Oumi, Y.; Itabashi, K.; Teranishi, T.; Sano, T., *Chemistry of Materials* **2003,** *16* (2), 286-291.

16. Fegan, S. G.; Lowe, B. M., *Journal of the Chemical Society, Faraday Transactions 1: Physical Chemistry in Condensed Phases* **1986,** *82* (3), 785-799.

17. Camblor, M. A.; Villaescusa, L. A.; Díaz-Cabañas, M. J., *Topics in Catalysis* **1999,** *9* (1), 59-76.

18. Robson, H.; Lillerud, K. P., *Verified Syntheses of Zeolitic Materials*. Elsevier: Amsterdam, **2001**.

19. Flanigen, E. M., A Review and New Perspectives in Zeolite Crystallization. In *Molecular Sieves*, Meier, W. M.; Uytterhoeven, J. B., Eds. American Chemical Society: Washington, **1973**; Vol. 121, 119-139.

20. Feijen, E. J. P.; Martens, J. A.; Jacobs, P. A., Zeolites and their Mechanism of Synthesis. In *Studies in Surface Science and Catalysis*, J. Weitkamp, H. G. K. H. P.; Hölderich, W., Eds. Elsevier: Louvain-la-Neuve, **1994**, Vol. 84, 3-21.

21. Barrer, R. M.; Denny, P. J., *Journal of the Chemical Society (Resumed)* **1961**, 971-982.

22. Lok, B. M.; Cannan, T. R.; Messina, C. A., *Zeolites* **1983,** *3* (4), 282-291.

23. Davis, M. E.; Lobo, R. F., *Chemistry of Materials* **1992,** *4* (4), 756-768.

24. Delprato, F.; Delmotte, L.; Guth, J. L.; Huve, L., *Zeolites* **1990,** *10* (6), 546-552.

25. Goretsky, A. V.; Beck, L. W.; Zones, S. I.; Davis, M. E., *Microporous and Mesoporous Materials* **1999,** *28* (3), 387-393.

26. Burkett, S. L.; Davis, M. E., Towards the Rational Design and Synthesis of Zeolites. In *Advances in Porous Materials*, Komarneni, S.; Smith, D. M.; Beck, J. S., Eds. Materials Research Society: Pittsburgh, **1995**, Vol. 371, 3-14.

27. Davis, M. E., Strategies for Zeolite Synthesis by Design. In *Studies in Surface Science and Catalysis.* Laurent, B.; Serge, K., Eds. Elsevier: Quebec, **1995**, Vol. 97, 35-44.

28. Morris, R. E.; Weigel, S. J., *Chemical Society Reviews* **1997,** *26* (4), 309-317.

29. Twomey, T. A. M.; Mackay, M.; Kuipers, H. P. C. E.; Thompson, R. W., *Zeolites* **1994,** *14* (3), 162-168.

30. Ogura, M.; Kawazu, Y.; Takahashi, H.; Okubo, T., *Chemistry of Materials* **2003,** *15* (13), 2661-2667.

31. Di Renzo, F.; Remoué, F.; Massiani, P.; Fajula, F.; Figueras, F.; Thierry Des, C., *Zeolites* **1991,** *11* (6), 539-548.

32. Hanif, N.; Anderson, M. W.; Alfredsson, V.; Terasaki, O., *Physical Chemistry Chemical Physics* **2000,** *2* (14), 3349-3357.

33. Feoktistova, N. N.; Zhdanov, S. P.; Lutz, W.; Büllow, M., *Zeolites* **1989,** *9* (2), 136-139.

34. Cundy, C. S.; Lowe, B. M.; Sinclair, D. M., *Faraday Discussions* **1993,** *95 (0)*, 235-252.

35. Ciric, J., *Journal of Colloid and Interface Science* **1968,** *28* (2), 315-324.

36. Van Santen, R. A., *The Journal of Physical Chemistry* **1984,** *88* (24), 5768-5769.

37. Barrer, R. M., Zeolites: Their Nucleation and Growth. In *Zeolite Synthesis*, Occelli, M. L.; Robson, H. E., Eds. American Chemical Society: Washington, **1989**; Vol. 398, 11-27.

38. Yang, S.; Navrotsky, A., *Chemistry of Materials* **2004,** *16* (19), 3682-3687.

39. Cubillas, P.; Anderson, M. W., Synthesis Mechanism: Crystal Growth and Nucleation. In *Zeolites and Catalysis*, Čejka, J.; Corma, A.; Zones, S. I., Eds. Wiley-VCH: Weinheim, **2010**, Vol. 1, 1-55.

40. Mintova, S.; Olson, N. H.; Valtchev, V.; Bein, T., *Science* **1999,** *283* (5404), 958-960.

41. Brian J, S., *Zeolites* **1997,** *18* (2-3), 97-105.

42. Watson, J. N.; Iton, L. E.; Keir, R. I.; Thomas, J. C.; Dowling, T. L.; White, J. W., *The Journal of Physical Chemistry B* **1997,** *101* (48), 10094-10104.

43. Cheng, C.-H.; Shantz, D. F., *Current Opinion in Colloid & Interface Science* **2005,** *10* (5-6), 188-194.

44. Cheng, C.-H.; Shantz, D. F., *The Journal of Physical Chemistry B* **2005,** *109* (29), 13912-13920.

45. Cheng, C.-H.; Shantz, D. F., *The Journal of Physical Chemistry B* **2005,** *109* (41), 19116-19125.

46. Cheng, C.-H.; Shantz, D. F., *The Journal of Physical Chemistry B* **2005,** *109* (15), 7266-7274.

47. Li, Q.; Mihailova, B.; Creaser, D.; Sterte, J., *Microporous and Mesoporous Materials* **2000,** *40* (1-3), 53-62.

48. Li, Q.; Mihailova, B.; Creaser, D.; Sterte, J., *Microporous and Mesoporous Materials* **2001,** *43* (1), 51-59.

49. Navrotsky, A., *Current Opinion in Colloid & Interface Science* **2005,** *10* (5-6), 195-202.

50. Nikolakis, V.; Tsapatsis, M.; Vlachos, D. G., *Langmuir* **2003,** *19* (11), 4619-4626.

51. Persson, A. E.; Schoeman, B. J.; Sterte, J.; Otterstedt, J. E., *Zeolites* **1994,** *14* (7), 557-567.

52. Schoeman, B. J., *Zeolites* **1997,** *18* (2-3), 97-105.

53. Schoeman, B. J., *Microporous and Mesoporous Materials* **1998,** *22* (1-3), 9-22.

54. Yang, S.; Navrotsky, A., *Chemistry of Materials* **2002,** *14* (6), 2803-2811.

55. Yang, S.; Navrotsky, A.; Wesolowski, D. J.; Pople, J. A., *Chemistry of Materials* **2004,** *16* (2), 210-219.

56. Yang, S.; Navrotsky, A., *Microporous and Mesoporous Materials* **2002,** *52* (2), 93-103.

57. Lobo, R. F.; Zones, S. I.; Davis, M. E., *Journal of Inclusion Phenomena and Molecular Recognition in Chemistry* **1995,** *21* (1-4), 47-78.

58. Cheng, C.-H.; Shantz, D. F., *The Journal of Physical Chemistry B* **2005,** *110* (1), 313-318.

59. Davis, T. M.; Drews, T. O.; Ramanan, H.; He, C.; Dong, J.; Schnablegger, H.; Katsoulakis, M. A.; Kokkoli, E.; McCormick, A. V.; Penn, R. L.; Tsapatsis, M., *Nature Materials* **2006,** *5* (5), 400-408.

60. Fedeyko, J.; Vlachos, D. G.; Lobo, R. F., *Langmuir* **2005,** *21* (11), 5197-5206.

61. Fedeyko, J. M.; Rimer, J. D.; Lobo, R. F.; Vlachos, D. G., *The Journal of Physical Chemistry B* **2004,** *108* (33), 12271-12275.

62. Follens, L. R. A.; Aerts, A.; Haouas, M.; Caremans, T. P.; Loppinet, B.; Goderis, B.; Vermant, J.; Taulelle, F.; Martens, J. A.; Kirschhock, C. E. A., *Physical Chemistry Chemical Physics* **2008,** *10* (36), 5574-5583.

63. Kragten, D. D.; Fedeyko, J. M.; Sawant, K. R.; Rimer, J. D.; Vlachos, D. G.; Lobo, R. F.; Tsapatsis, M., *The Journal of Physical Chemistry B* **2003,** *107* (37), 10006-10016.

64. Kumar, S.; Wang, Z.; Penn, R. L.; Tsapatsis, M., *Journal of the American Chemical Society* **2008,** *130* (51), 17284-17286.

65. Mintova, S.; Olson, N. H.; Senker, J.; Bein, T., *Angewandte Chemie International Edition* **2002,** *41* (14), 2558-2561.

66. Mintova, S.; Valtchev, V.; Bein, T., *Colloids and Surfaces A: Physicochemical and Engineering Aspects* **2003,** *217* (1-3), 153-157.

67. Rimer, J. D.; Fedeyko, J.; Vlachos, D. G.; Lobo, R. F., *Chemistry A European Journal* **2006,** *12* (11), 2926-2934.

68. Rimer, J. D.; Lobo, R. F.; Vlachos, D. G., *Langmuir* **2005,** *21* (19), 8960-8971.

69. Rimer, J. D.; Vlachos, D. G.; Lobo, R. F., *The Journal of Physical Chemistry B* **2005,** *109* (26), 12762-12771.

70. Rimer, J. D.; Vlachos, D. G.; Lobo, R. F., Kinetics of Silicalite-1 Crystallization. In *Studies in Surface Science and Catalysis*, Ruren Xu, Z. G. J. C.; Wenfu, Y., Eds. Elsevier: **2007**, Vol. 170, 133-144.

71. Hould, N. D.; Lobo, R. F., *Chemistry of Materials* **2008,** *20* (18), 5807-5815.

72. de Moor, P. P. E. A.; Beelen, T. P. M.; Komanschek, B. U.; van Santen, R. A., *Microporous and Mesoporous Materials* **1998,** *21* (4-6), 263-269.

73. de Moor, P. P. E. A.; Beelen, T. P. M.; van Santen, R. A., *The Journal of Physical Chemistry B* **1999,** *103* (10), 1639-1650.

74. de Moor, P.-P. E. A.; Beelen, T. P. M.; Komanschek, B. U.; Beck, L. W.; Wagner, P.; Davis, M. E.; van Santen, R. A., *Chemistry – A European Journal* **1999,** *5* (7), 2083-2088.

75. de Moor, P.-P. E. A.; Beelen, T. P. M.; Komanschek, B. U.; Diat, O.; van Santen, R. A., *The Journal of Physical Chemistry B* **1997,** *101* (51), 11077-11086.

76. de Moor, P.-P. E. A.; Beelen, T. P. M.; van Santen, R. A.; Beck, L. W.; Davis, M. E., *The Journal of Physical Chemistry B* **2000,** *104* (32), 7600-7611.

77. de Moor, P.-P. E. A.; Beelen, T. P. M.; van Santen, R. A.; Tsuji, K.; Davis, M. E., *Chemistry of Materials* **1999,** *11* (1), 36-43.

78. Iton, L. E.; Trouw, F.; Brun, T. O.; Epperson, J. E.; White, J. W.; Henderson, S. J., *Langmuir* **1992,** *8* (4), 1045-1048.

79. Provis, J. L.; Gehman, J. D.; White, C. E.; Vlachos, D. G., *The Journal of Physical Chemistry C* **2008,** *112* (38), 14769-14775.

80. Provis, J. L.; Vlachos, D. G., *The Journal of Physical Chemistry B* **2006,** *110* (7), 3098-3108.

81. Rimer, J. D.; Trofymluk, O.; Navrotsky, A.; Lobo, R. F.; Vlachos, D. G., *Chemistry of Materials* **2007,** *19* (17), 4189-4197.

82. Schoeman, B. J., *Microporous Materials* **1997,** *9* (5-6), 267-271.

83. Schoeman, B. J.; Babouchkina, E.; Mintova, S.; Valtchev, V. P.; Sterte, J., *Journal of Porous Materials* **2001,** *8* (1), 13-22.

84. Schoeman, B. J.; Regev, O., *Zeolites* **1996,** *17* (5-6), 447-456.

85. Aerts, A.; Follens, L. R. A.; Haouas, M.; Caremans, T. P.; Delsuc, M.-A.; Loppinet, B.; Vermant, J.; Goderis, B.; Taulelle, F.; Martens, J. A.; Kirschhock, C. E. A., *Chemistry of Materials* **2007,** *19* (14), 3448-3454.

86. Fyfe, C. A.; Darton, R. J.; Schneider, C.; Scheffler, F., *The Journal of Physical Chemistry C* **2007,** *112* (1), 80-88.

87. Haouas, M.; Taulelle, F., *The Journal of Physical Chemistry B* **2006,** *110* (7), 3007-3014.

88. Houssin, C. J. Y.; Kirschhock, C. E. A.; Magusin, P. C. M. M.; Mojet, B. L.; Grobet, P. J.; Jacobs, P. A.; Martens, J. A.; van Santen, R. A., *Physical Chemistry Chemical Physics* **2003,** *5* (16), 3518-3524.

89. Kinrade, S. D.; Donovan, J. C. H.; Schach, A. S.; Knight, C. T. G., *Journal of the Chemical Society, Dalton Transactions* **2002,** (7), 1250-1252.

90. Kinrade, S. D.; Knight, C. T. G.; Pole, D. L.; Syvitski, R. T., *Inorganic Chemistry* **1998,** *37* (17), 4272-4277.

91. Knight, C. T. G., *Zeolites* **1990,** *10* (2), 140-144.

92. Knight, C. T. G.; Syvitski, R. T.; Kinrade, S. D.; Laurent, B.; Serge, K., Aqueous Silicate Chemistry in Zeolite Synthesis. In *Studies in Surface Science and Catalysis.* Elsevier: Quebec, Vol. 97, **1995**, 483-488.

93. Knight, C. T. G.; Wang, J.; Kinrade, S. D., *Physical Chemistry Chemical Physics* **2006,** *8* (26), 3099-3103.

94. Petry, D. P.; Haouas, M.; Wong, S. C. C.; Aerts, A.; Kirschhock, C. E. A.; Martens, J. A.; Gaskell, S. J.; Anderson, M. W.; Taulelle, F., *The Journal of Physical Chemistry C* **2009,** *113* (49), 20827-20836.

95. Navrotsky, A.; Trofymluk, O.; Levchenko, A. A., *Chemical Reviews* **2009,** *109* (9), 3885-3902.

96. Piccione, P. M.; Yang, S.; Navrotsky, A.; Davis, M. E., *The Journal of Physical Chemistry B* **2002,** *106* (14), 3629-3638.

97. Kumar, S.; Davis, T. M.; Ramanan, H.; Penn, R. L.; Tsapatsis, M., *The Journal of Physical Chemistry B* **2007,** *111* (13), 3398-3403.

98. Ramanan, H.; Kokkoli, E.; Tsapatsis, M., *Angewandte Chemie International Edition* **2004,** *43* (35), 4558-4561.

99. Schoeman, B. J.; Sterte, J.; Otterstedt, J. E., *Zeolites* **1994,** *14* (7), 568-575.

100. Watson, J. N.; Brown, A. S.; Iton, L. E.; White, J. W., *Journal of the Chemical Society, Faraday Transactions* **1998,** *94* (15), 2181-2186.

101. Gies, H.; Marler, B.; Werthmann, U., Synthesis of Porosils: Crystalline Nanoporous Silicas with Cage- and Channel-Like Void Structures Synthesis. Springer: Berlin, **1998**.

102. Kubota, Y.; Helmkamp, M. M.; Zones, S. I.; Davis, M. E., *Microporous Materials* **1996,** *6* (4), 213-229.

103. Lawton, S. L.; Rohrbaugh, W. J., *Science* **1990,** *247* (4948), 1319-1322.

104. Nakagawa, Y.; Lee, G. S.; Harris, T. V.; Yuen, L. T.; Zones, S. I., *Microporous and Mesoporous Materials* **1998,** *22* (1-3), 69-85.

105. Petrovic, I.; Navrotsky, A.; Davis, M. E.; Zones, S. I., *Chemistry of Materials* **1993,** *5* (12), 1805-1813.

106. Rollmann, L. D.; Schlenker, J. L.; Lawton, S. L.; Kennedy, C. L.; Kennedy, G. J.; Doren, D. J., *The Journal of Physical Chemistry B* **1999,** *103* (34), 7175-7183.

107. Zones, S. I.; Nakagawa, Y.; Lee, G. S.; Chen, C. Y.; Yuen, L. T., *Microporous and Mesoporous Materials* **1998,** *21* (4-6), 199-211.

108. Zones, S. I.; Nakagawa, Y.; Yuen, L. T.; Harris, T. V., *Journal of the American Chemical Society* **1996,** *118* (32), 7558-7567.

109. Burkett, S. L.; Davis, M. E., *Chemistry of Materials* **1995,** *7* (8), 1453-1463.

110. Harris, R. K.; Jones, J.; Knight, C. T. G.; Pawson, D., *Journal of Molecular Structure* **1980,** *69*, 95-103.

111. Harris, R. K.; Knight, C. T. G., *Journal of Molecular Structure* **1982,** *78* (3-4), 273-278.

112. Harris, R. K.; Knight, C. T. G., *Journal of the Chemical Society, Faraday Transactions 2: Molecular and Chemical Physics* **1983,** *79* (10), 1525-1538.

113. Harris, R. K.; Knight, C. T. G., *Journal of the Chemical Society, Faraday Transactions 2: Molecular and Chemical Physics* **1983,** *79* (10), 1539-1561.

114. Harris, R. K.; Knight, C. T. G.; Hull, W. E., *Journal of the American Chemical Society* **1981,** *103* (6), 1577-1578.

115. Kinrade, S. D.; Knight, C. T. G.; Pole, D. L.; Syvitski, R. T., *Inorganic Chemistry* **1998,** *37* (17), 4278-4283.

116. Kinrade, S. D.; Marat, K.; Knight, C. T. G., *The Journal of Physical Chemistry* **1996,** *100* (47), 18351-18356.

117. Kinrade, S. D.; Pole, D. L., *Inorganic Chemistry* **1992,** *31* (22), 4558-4563.

118. Kinrade, S. D.; Swaddle, T. W., *Inorganic Chemistry* **1988,** *27* (23), 4253-4259.

119. Kinrade, S. D.; Swaddle, T. W., *Inorganic Chemistry* **1988,** *27* (23), 4259-4264.

120. Knight, C. T. G., *Journal of the Chemical Society, Dalton Transactions* **1988,** (6), 1457-1460.

121. Knight, C. T. G., *Zeolites* **1989,** *9* (5), 448-450.

122. Knight, C. T. G.; Kirkpatrick, R. J.; Oldfield, E., *Journal of the Chemical Society, Chemical Communications* **1986,** (1), 66-67.

123. Kirschhock, C. E. A.; Buschmann, V.; Kremer, S.; Ravishankar, R.; Houssin, C. J. Y.; Mojet, B. L.; van Santen, R. A.; Grobet, P. J.; Jacobs, P. A.; Martens, J. A., *Angewandte Chemie International Edition* **2001,** *40* (14), 2637-2640.

124. Kirschhock, C. E. A.; Kremer, S. P. B.; Grobet, P. J.; Jacobs, P. A.; Martens, J. A., *The Journal of Physical Chemistry B* **2002,** *106* (19), 4897-4900.

125. Kirschhock, C. E. A.; Ravishankar, R.; Jacobs, P. A.; Martens, J. A., *The Journal of Physical Chemistry B* **1999,** *103* (50), 11021-11027.

126. Kirschhock, C. E. A.; Ravishankar, R.; Looveren, L. V.; Jacobs, P. A.; Martens, J. A., *The Journal of Physical Chemistry B* **1999,** *103* (24), 4972-4978.

127. Kirschhock, C. E. A.; Ravishankar, R.; Verspeurt, F.; Grobet, P. J.; Jacobs, P. A.; Martens, J. A., *The Journal of Physical Chemistry B* **1999,** *103* (24), 4965-4971.

128. Kirschhock, C. E. A.; Ravishankar, R.; Verspeurt, F.; Grobet, P. J.; Jacobs, P. A.; Martens, J. A., *The Journal of Physical Chemistry B* **2002,** *106* (12), 3333-3334.

129. Ravishankar, R.; Kirschhock, C.; Schoeman, B. J.; Vanoppen, P.; Grobet, P. J.; Storck, S.; Maier, W. F.; Martens, J. A.; De Schryver, F. C.; Jacobs, P. A., *The Journal of Physical Chemistry B* **1998,** *102* (15), 2633-2639.

130. Ravishankar, R.; Kirschhock, C. E. A.; Knops-Gerrits, P.-P.; Feijen, E. J. P.; Grobet, P. J.; Vanoppen, P.; De Schryver, F. C.; Miehe, G.; Fuess, H.; Schoeman, B. J.; Jacobs, P. A.; Martens, J. A., *The Journal of Physical Chemistry B* **1999,** *103* (24), 4960-4964.

131. Knight, C. T. G.; Kinrade, S. D., *The Journal of Physical Chemistry B* **2002,** *106* (12), 3329-3332.

132. Shi, J.; Anderson, M. W.; Carr, S. W., *Chemistry of Materials* **1996,** *8* (2), 369-375.

133. Choudhury, R. P.; Schonhoff, M., *The Journal of Chemical Physics* **2007,** *127* (23), 234702.

134. Friebolin, H., *Basic One- and Two-Dimensional NMR Spectroscopy*. Wiley-VCH: Weinheim, **1998**.

135. Homans, S. W., *A Dictionary of Concepts in NMR*. Oxford University Press: New York, **1989**.

136. Weber, U.; Thiele, H., *NMR Spectroscopy: Modern Spectral Analysis*. Wiley-VCH: Weinheim, **1998**.

137. Ruthven, D. M., *Principles of Adsorption and Adsorption Process*. Wiley: New York, **1984**.

138. Hrabe, J.; Kaur, G.; Guilfoyle, D., *Journal of Medical Physics* **2007,** *32* (1), 34-42.

139. Price, W. S., *Concepts in Magnetic Resonance* **1997,** *9* (5), 299-336.

140. Peschier, L. J. C.; Bouwstra, J. A.; de Bleyser, J.; Junginger, H. E.; Leyte, J. C., *Journal of Magnetic Resonance, Series B* **1996,** *110* (2), 150-157.

141. Tanner, J. E., *The Journal of Chemical Physics* **1970,** *52* (5), 2523-2526.

142. Berger, S.; Braun, S., *200 and More NMR Experiments*. Wiley-VCH: Weinheim, **2004**.

143. Johnson, C. S., *Progress in Nuclear Magnetic Resonance Spectroscopy* **1999,** *34* (3-4), 203-256.

144. Morris, K. F.; Johnson, C. S., *Journal of the American Chemical Society* **1992,** *114* (8), 3139-3141.

145. Morris, K. F.; Stilbs, P.; Johnson, C. S., *Analytical Chemistry* **1994,** *66* (2), 211-215.

146. Wu, D.; Chen, A.; Johnson, J. C. S., *Journal of Magnetic Resonance, Series A* **1996,** *123* (2), 215-218.

147. Wu, D. H.; Chen, A. D.; Johnson, C. S., *Journal of Magnetic Resonance, Series A* **1995,** *115* (2), 260-264.

148. Antalek, B., *Concepts in Magnetic Resonance* **2002,** *14* (4), 225-258.

149. Chen, A.; Wu, D.; Johnson, C. S., *Journal of the American Chemical Society* **1995,** *117* (30), 7965-7970.

150. Cohen, Y.; Avram, L.; Frish, L., *Angewandte Chemie International Edition* **2005,** *44* (4), 520-554.

151. Huo, R.; Wehrens, R.; Duynhoven, J. v.; Buydens, L. M. C., *Analytica Chimica Acta* **2003,** *490* (1-2), 231-251.

152. Ovenden, S. P. B.; Bourne, D. J. *The Diffusion Ordered Spectroscopy (DOSY) Pulse Sequence and Defence Applications*; Human Protection and Performance Division: Australia, **2008**.

153. Price, K. E.; Lucas, L. H.; Larive, C. K., *Analytical and Bioanalytical Chemistry* **2004,** *378* (6), 1405-1407.

154. Gounarides, J. S.; Chen, A.; Shapiro, M. J., *Journal of Chromatography B: Biomedical Sciences and Applications* **1999,** *725* (1), 79-90.

155. Hallberg, F.; Weise, C. F.; Yushmanov, P. V.; Pettersson, E. T.; Stilbs, P.; Furo, I., *Journal of the American Chemical Society* **2008,** *130* (24), 7550-7551.

156. Pecora, R., *Dynamic Light Scattering: Applications of Photon Correlation Spectroscopy*. Plenum Press: New York, **1985**.

157. Schmitz, K. S., *An Introduction to Dynamic Light Scattering by Macromolecules*. Academic Press: Boston, **1990**.

158. Tscharnuter, W., Photon Correlation Spectroscopy in Particle Sizing. In *Encyclopedia of Analytical Chemistry*, Meyers, R. A., Ed. John Wiley & Sons: Chichester, **2000**, 5469-5485.

159. Bodnar, M.; Hartmann, J. F.; Borbely, J., *Biomacromolecules* **2006,** *7* (11), 3030-3036.

160. Roig, A. R.; Alessandrini, J. L., *Particle & Particle Systems Characterization* **2006,** *23* (6), 431-437.

161. Yu, L.-S.; Yang, G.-l.; He, Z.-j.; Li, Y., *Acta Laser Biology Sinica* **2007,** *16* (1), 74-78.

162. Azaroff, L. V.; Buerger, M. J., *The Powder Method in X-ray Crystallography*. McGraw-Hill: New York, **1958**.

163. Nuffield, E. W., *X-ray Diffraction Methods*. Wiley: New York, **1966**.

164. Hans, L., The pH-value and its Importance for the Crystallization of Zeolites. In *Verified Synthesis of Zeolitic Materials*, Robson, H., Ed. Elsevier: Amsterdam, **2001**, 33-38.

165. Kärger, J., *Annalen der Physik* **1971,** *482* (1), 107-109.

166. Kärger, J., *Adv. Colloid Interface Sci.* **1985,** *23*, 129-148.

167. Woessner, D. E., *Concepts in Magnetic Resonance* **1996,** *8* (6), 397-421.

168. NMR Spectroscopy User Guide. Varian, Inc. Inova and MercuryPlus NMR Systems with VnmrJ 2.2D Software Pub. No. 01-999378-00, Rev. A 0808.

169. Holz, M.; Weingartner, H., *Journal of Magnetic Resonance* **1969,** *92* (1), 115-125.

170. Rivas-Cardona, A.; Shantz, D. F., *The Journal of Physical Chemistry C* **2010,** *114* (47), 20178-20188.

171. Lucas, L. H.; Yan, J.; Larive, C. K.; Zartler, E. R.; Shapiro, M. J., *Analytical Chemistry* **2003,** *75* (3), 627-634.

172. Nikolakis, V.; Kokkoli, E.; Tirrell, M.; Tsapatsis, M.; Vlachos, D. G., *Chemistry of Materials* **2000,** *12* (3), 845-853.

173. Rivas-Cardona, A.; Shantz, D. F., *The Journal of Physical Chemistry C* **2011,** *115* (26), 13016-13026.

174. Subramanyam, B.; Das, A., *International Journal of Environmental Science and Technology* **2009,** *6* (4), 633-640.

175. Sparks, D. L., *Environmental Soil Chemistry*. Academic Press: San Diego, **2003**.

176. Chen, Z.; Xing, B.; McGill, W. B., *Journal of Environmental Quality* **1999,** *28* (5), 1422-1428.

177. Rimer, J. D.; Trofymluk, O.; Lobo, R. F.; Navrotsky, A.; Vlachos, D. G., *The Journal of Physical Chemistry C* **2008,** *112* (38), 14754-14761.

178. Kärger, J.; Pfeifer, H., *Zeolites* **1987,** *7* (2), 90-107.

179. Holz, M.; Heil, S. R.; Sacco, A., *Physical Chemistry Chemical Physics* **2000,** *2* (20), 4740-4742.

180. Li, X.; Shantz, D. F., *The Journal of Physical Chemistry C* **2010,** *114* (34), 14561-14570.

181. Li, X.; Shantz, D. F., *The Journal of Physical Chemistry C* **2010,** *114* (18), 8449-8458.

182. Li, X.; Shantz, D. F., *Langmuir* **2010,** *26* (23), 18459-18467.

183. Tokay, B.; Somer, M.; Erdem-Senatalar, A.; Schüth, F.; Thompson, R. W., *Microporous and Mesoporous Materials* **2009,** *118* (1-3), 143-151.

184. Rimer, J. D. Dissertation: Self-Assembly of Silica Nanoparticles and their Role in the Mechanism of Silicalite-1 Crystallization. University of Delaware: Delaware, **2006**.

185. Bordelon, L. L., Design of Experiments Applied to Flight Testing. In *Mission Systems Engineering*, Educational Notes RTO-EN-SCI-176: Neuilly-sur-Sein, **2006**.

VITA

Name: Alejandra del Rocio Rivas Cardona

Address: Johnson Matthey, 436 Devon Park Drive, Wayne, PA 19087-1816

Email Address: ale.rivas25@gmail.com

Education: B.S., Chemical Engineering, Instituto Tecnologico de Celaya, 2004
M.S., Chemical Engineering, Instituto Tecnologico de Celaya, 2007
Ph.D., Chemical Engineering, Texas A&M University, 2011

AWARDS

B.S. degree awarded with honors.

National scholarship for undergraduate studies from Mexican Secretariat of Public Education (SEP for its acronym in Spanish: Secretaria de Educacion Publica), 2005.

National scholarship for graduate studies from the Mexican National Council of Science and Technology (CONACYT for its acronym in Spanish: Consejo Nacional de Ciencia y Tecnologia), 2007-2010.

Member of the Omega Chi Epsilon Chemical Engineering Honor Society, Texas A&M University, 2010.

PUBLICATIONS

Rivas-Cardona, A. and Shantz, D. F., Pulsed-Field Gradient NMR Investigations of Alkyltripropylammonium-Silica Mixtures, *Journal of Physical Chemistry C* **2010**, 114, 20178-20188.

Rivas-Cardona, A. and Shantz, D. F., In Situ PFG-NMR of Silicalite-1 Synthesis Mixtures, *Journal of Physical Chemistry C* **2011**, 115, 13016-13026.